UNIVERSITY OF CALIFORNIA SANTA CRUZ

SANTA CRUZ

Design of Efficient Photocatalytic Nanocomposites Composed of Manganese Oxides and Graphene Oxide Quantum Dots for Bactericidal Activity: Exploring the Structural and Chemical Roles of Photoactivity

A dissertation submitted in partial satisfaction
of the requirements for the degree of

DOCTOR OF PHILOSOPHY

In

CHEMISTRY

by

Gustavo Chata

June 2021

The Dissertation of Gustavo Chata is approved:

_____
Professor Shaowei Chen, Chair

_____
Professor Scott R. J. Oliver

_____
Professor Alexander Ayzner

_____
Quentin Williams

Interim Vice Provost and Dean of Graduate Studies

Table of Contents

LIST OF FIGURES AND TABLES

CHAPTER 2

Abstract

Design of Efficient Photocatalytic Nanocomposites Composed of Manganese Oxides and Graphene Oxide Quantum Dots for Bactericidal Activity: Exploring the Structural and Chemical Roles of Photoactivity

Gustavo Chata

The bactericidal utility of inorganic chemicals predates back to 1500 BP where Egyptians recorded the use of copper as an antibacterial agent. Recently, inorganic nanomaterials like silver and copper are utilized for sutures to prevent bacterial infections. The biomedical application of nanomaterials is imperative due to the threatening increase in antibiotic resistance bacteria which is projected to become a leading cause of death in 2050 [1]. The diminished antibacterial activity of antibiotics is attributed to their cellular target specificity which lead to rapid bacterial resistance. In contrast to antibiotics nanomaterials (ex. CuNP) produce bactericidal activity by providing broad-spectrum activity. Therein the indiscriminatory activity of inorganic nanoparticles provide multiple cellular targets leading to efficient bactericidal

activity. Aggregation and ionization of metal-based nanoparticles may lead to cytotoxicity in a host's cells; a lower concentration of chemically stable metal-based nanoparticle can enhance biocompatibility. The application of photoactive metal-oxide based nanocomposites exerts bactericidal activity at a markedly lower concentration in contrast to metal-based nanoparticles. In the present thesis we focus on exploring the photoactivity of a Mn_xO_y/GOQD nanocomposite and its source of antibacterial activity.

Chapter 2 describes the design of GOQD/MnO_2 via oxidation of graphene oxide with $KMnO_4$ as an oxidizer to produce an effective photocatalyst for bactericidal activity. A series of $KMnO_4$ feed ratios was utilized to deposited varying concentrations of MnO_2 onto GOQD. The deposition of MnO_2 was analyzed via high resolution transmission electron microscopy (HRTEM) by the (211) lattice present in α-MnO_2 nanowires. The chemical composition of the composite nanostructures was analyzed by X-ray photoelectron spectroscopy (XPS) to analyze the chemical composition and concentration of deposited MnO_2. An optimal concentration of 7.85% Mn/C contained the most efficient photoactivity against *E. coli* at a concentration of 0.1 mg/mL, which is lower

than the accounted MIC of the catalyst occurring at 5 mg/mL. The enhanced photoactivity was measured via electron paramagnetic resonance (EPR) which attributed the enhanced photoactivity to hydride and hydroxide radical production.

In chapter 3 a series of first row transition metals with attributed bactericidal activity were deposited via a facile sonication method. The doping of graphene oxide was accounted by HRTEM and XPS which both demonstrated the presence of metal ions without the presence of lattice oxygen, commonly measured from metal oxide structures. The enhanced photodynamic activity against *E.coli* is documented for GOQD-Co^{2+} at an excitation of 365 nm. Analysis of time resolved fluorescence lifetime (TRFL) demonstrates an extended lifetime at the excited state for Co^{2+}-GOQD. The diminished methylene blue degradation (MBD) demonstrates bactericidal activity mechanism independent of ROS formation.

In chapter 4 polyaniline (PANI) was utilized to anchor Mn_xO_y onto the GOQD structure. The deposition of various Mn_xO_y nanoparticles was assessed via HRTEM while the oxidation state of the Mn was measured via XPS. The

bactericidal activity was measured in the dark and under light irradiation for a gram-negative *E.coli* and gram-positive *S.Epidermidis*. The enhanced photodegradation determined from an Ellman's reagent assay and EPR found a higher valency Mn_xO_y deposited on GOQD with PANI to produce a higher concentration of ROS, specifically hydroxyl radical species ($HO^{\cdot}$). Although the enhanced bactericidal activity was evident from GPM-1 and GPM-2 samples which produced a lower concentration of $HO^{\cdot}$. The scanning electron microscopy (SEM) data details the intimate nanocomposite to cellular interface in both GPM-1 and GPM-2 samples therein shedding light on its photoinduced bactericidal mechanism

ACKNOWLEDGEMENTS

On a simmering vibrant summer day I found myself expeditiously pacing to the chambers of the man of whom would undoubtedly develop my life's journey. A joyous and towering man with an infectious laugh and energy greeted me in the chambers of his office. His passion and desire for developing science was undeniable and I could evidently find a glimmer of hope for the unexplored and unknown. A glimmer which I had readily found stirring within the cauldrons of my intellectual stew. I realized on that fateful day I was staring at my future advisor Dr. Shaowei Chen, a man who understood the rigorous training required to develop a scientist. I knew I was fortunate to have met such a remarkable person and as my graduate career ends I still find myself in gratitude for his efforts.

My graduate committee have been pillars of academic excellence providing the necessary balance of support and criticism I have often required. I am deeply indebted to both Dr. Scott Oliver and Dr. Alexander Ayzner for finding interest in my work and providing the necessary analysis and commentary in critical points of my academic career. I found all of the opinions shared by both of you as

part of my own critical observations of my own work. Thank you for your inquisitive interest and timely support for my development.

The nature of my graduate work required an extensive amount of collaboration. I would be remiss to highlight the importance of Dr. Chad Saltikov as a commendatory figure in my development as a scientist. I deeply appreciate your continuous effort to equalize my humble graduate position to your elite professorship status. Often, I found myself discussing ideas to a person I felt was a colleague who was greatly attributed to your charisma. I appreciate access to the well of vast knowledge and experience you possess, and while I only nourished my growth with a glass-full it was enough to sprout an honorable degree.

DEDICATION

I dedicate my degree to all people who find themselves questioning their full potential. As a Venezuelan immigrant to a low middle class family, I rarely found myself with the notion fulfilling a degree with this level of prestige. Although I was absorbed by science experiments which I would readily conduct in my spare time with a chemistry model set gifted to me by my aunt. Undeniably the support provided by my family has been my greatest blessing because they recognized that glimmer of light slowly developing with time and enhanced its strength with love and compassion. I thank God for providing such a special gift and I hope whoever reads this work knows that love is within us all. The desire to give it and receive it is up to us and while life challenges us we are always observed with compassion even if it remains unknown to us. So don't stop, keep growing, keep loving.

Chapter 1: Introduction

1.1 Risk of Antibiotic Resistance in both Gram-Positive and Gram-Negative Bacteria

Antibiotic resistance is reported to occur when a drug loses its ability to inhibit cell growth effectively. The rate of antibiotic resistance is amplified by the rate of cellular machinery of bacteria which has continuously inhibited the development of alternative therapeutics [2]. The intrinsic resistance of bacteria can occur from loss of a cellular target or an enzyme rendering the antibiotic inactive [3]. The resistant mechanisms are readily transferred to various bacterial organisms via genomic modification, therefore once resistance is developed it can expeditiously be transferred via transduction and conjugation. The structural difference between gram-positive and gram-negative bacteria defines the mechanism of antibiotic resistance exhibited by the cell. An example of diverging bacterial mechanisms based upon structural difference is portrayed by the application of β-lactam antibiotics [4]. The membrane protected peptidoglycan layer of gram-negative bacteria allows it to utilize a β-lactam antibiotic degrading enzyme known as β-lactamase to inactivate the antibiotic [5]. In contrast to the peptidoglycan exposed gram-positive

bacteria which instead utilize penicillin binding protein (PBP)[6]. The structural variation, rate of genomic mutation, and transference of resistant genomic regions leads to the application of various antibiotics to inhibit bacterial growth[3]. The continuous application of antibiotics can eventually lead to the resistance of the applied molecules therein requiring alternative therapeutics to combat antibiotic resistant bacteria.

To modulate the established antibiotic resistance mechanisms which both gram-negative and gram-positive bacteria have exploited, alternative therapeutics have been adapted with varying bactericidal mechanisms[7, 8]. An example include antimicrobial oligonucleotides which serve to silence the regions of bacterial genome related to antibiotic resistance and phage therapy which utilize viral proteins to infect bacteria [8]. The unique bactericidal activity of such alternative therapeutics may be specific to certain strains of bacteria or require a specific drug-delivery material to allow for its efficacy. Therefore, streamlining a manufacturing procedure for various strains of bacteria and medical conditions can be challenging. Nanomaterials have

been readily applied as alternative therapeutics for treatment of antibiotic resistant bacteria [9, 10].

Nanoparticles allow for enhanced therapeutic to cell membrane interaction which regulate cell membrane regulation and interfere with molecular pathways. The mechanism of bactericidal activity includes a) disruption of membrane integrity, b) triggering of host immune response, c) inhibition of biofilm formation, d) generation of reactive oxygen species (ROS), and e) inhibition of RNA and protein synthesis through the induction of intracellular effects. The bactericidal activity of nanoparticles may be exhibited by various of the described mechanisms thereby proving to be more efficacious target-specific antibiotics[11]. While the chemical stability of metal-based nanoparticles, ex. AgNPs and AuNPs, have been proven to be effective at selectively targeting bacterial organisms via surface modifications their aggregation and ionization may lead to cytotoxicity of the host's cells[12]. Therefore, a target-specific therapeutic water-soluble and dispersible bactericidal nanoparticle is desirable to prevent damage to eukaryotic cells.

Chapter 1.2 Efficacy of Carbon and Metal Oxide Based Nanocomposites

The high extent of oxygen moieties exhibited by graphene oxide quantum dots (GOQD) allows for water solubility which enhance their antimicrobial activity [13-15]. The chemical inertness of carbon enhances the biocompatibility of graphene-based nanoparticles. Furthermore, chemical modulation carbon frame can lower cytotoxicity as highlighted by the low level of genomic expression of hematopoietic stem cells[16]. The biocompatibility of graphene-based nanomaterials apply to various cells including fibroblasts and epithelial cells at concentrations up to 100 µg/mL with 48 hours of incubation[17]. The source of bactericidal activity stems from the enhanced interaction the nanomaterial exerts on the cell membrane.

The bactericidal activity of graphene oxide stems from its extent of oxidation at high concentrations >40µg/mL. An intimate cell-to-nanoparticle interaction is exhibited by the graphene oxide sheet enveloped *E.coli* imaged via AFM[14, 15]. While the graphene oxide quantum dots provide bactericidal activity at high concentrations, such

cytotoxicity can prove to be detrimental to the host. The characteristic band structure of graphene oxide quantum dots provides a mechanism to utilize photon excitation to induce reactive oxygen species (ROS) formation from electron-hole separation. The band structure produced by the sp^2 hybridization of graphene allows for π^*-π , σ^*-n, and π^*-n transition which are defined by the size of sp^2 sites and oxygen moieties functionalized on the carbon structure[18, 19]. While the UV assisted bactericidal activity of GOQD is attributed to photolysis of aliphatic hydroxyl groups, the electron-hole separation may lead to electron transfer from or to a deposited photocatalytic active site on the sp^2 frame.

The leading mechanism of photo catalytically active metal oxide nanoparticles for dye degradation can be utilized for bactericidal activity[20-22]. The band-gap structure of the metal oxide nanoparticles allows for electron-hole separation where the excited electron serves to reduce a solvated species while the hole serves to oxidize a solvated species. The probability of the electron-hole separation leading to ROS formation depends on the ability of the excited electron to recombine with the valence band. Furthermore, the extent of dispersion is critical in producing

an effective metal oxide based photocatalyst due to the short-lived production of ROS. A metal oxide-based nanoparticle lacking solubility may lead to an increasing concentration of ROS production but render it inactive against bacteria[22, 23]. Therefore, a water-soluble metal oxide nanomaterial is a desirable biocompatible therapeutic, but the inherent insolubility of metal oxide nanoparticles inhibits their individual application as photoactive bactericidal nanomaterials.

1.3 Direction of Research

The chemical inertness and biocompatibility of metal oxide nanoparticles enhances its application as alternative antibacterial therapeutics. The application of photoactive metal oxide nanoparticles such as Mn_xO_y nanoparticles is credited to the presence of its ionic form in cellularly relevant enzymes. A key enzyme like superoxide dismutase utilizes Mn(II) and Mn(III) to sequester superoxide therein leading to the production of hydrogen peroxide[24, 25]. Also, the various valence states exhibited by Mn_xO_y provide for stable transition states during electron transfer reaction induced from photoexcitation process. MnO_2 nanoparticles are a

highly valent Mn_xO_y nanoparticles which lead to a high rate of ROS dependent dye degradation. To enhance the biocompatibility of MnO_2, a nanocomposite of MnO_2 with GOQD was designed to evaluate the photoactivity of MnO_2 nanoparticles against *E.coli* in chapter 3.

The photoactivity of MnO_2/GOQD at λ = 365 nm excitation emphasized the relevance of an effective metal oxide-carbon nanocomposite, although the source of photoactivity was confounded from the synergistic photoactivity illustrated by the oxidized GOQD and dispersed MnO_2. The nucleation of MnO_2 via oxidation of sp^2 carbon domains evidently yield a lower valent Mn^{n+} ion which interfaces GOQD and MnO_2 [26, 27]. The metal ion-oxygen defect interaction from GOQD potentially leads to trapped states leading to enhanced electron-hole charge separation [18, 28, 29]. The electrostatic interaction of metal ions with oxygen defects of GOQD provided for a suitable mechanism of metal ion deposition to test the bactericidal efficacy as a function of electron-hole separation from first-row transition metal ions with bactericidal activity[30, 31] [32-34]. In chapter 4 the role of metal-chelated graphene oxide as active site for photocatalysis was tested.

1.4 References

1. Gold, K., et al., *Antimicrobial Activity of Metal and Metal-Oxide Based Nanoparticles.* Advanced Therapeutics, 2018. **1**(3).
2. Zaman, S.B., et al., *A Review on Antibiotic Resistance: Alarm Bells are Ringing.* Cureus, 2017. **9**(6): p. e1403.
3. Blair, J.M., et al., *Molecular mechanisms of antibiotic resistance.* Nat Rev Microbiol, 2015. **13**(1): p. 42-51.
4. Kong, K.F., L. Schneper, and K. Mathee, *Beta-lactam antibiotics: from antibiosis to resistance and bacteriology.* APMIS, 2010. **118**(1): p. 1-36.
5. Zeng, X. and J. Lin, *Beta-lactamase induction and cell wall metabolism in Gram-negative bacteria.* Front Microbiol, 2013. **4**: p. 128.
6. Macheboeuf, P., et al., *Penicillin binding proteins: key players in bacterial cell cycle and drug resistance processes.* FEMS Microbiol Rev, 2006. **30**(5): p. 673-91.
7. Waldetoft, K.W. and S.P. Brown, *Alternative therapeutics for self-limiting infections-An indirect approach to the antibiotic resistance challenge.* Plos Biology, 2017. **15**(12).
8. Streicher, L.M., *Exploring the future of infectious disease treatment in a post-antibiotic era: A comparative review of*

alternative therapeutics. J Glob Antimicrob Resist, 2021. **24**: p. 285-295.

9. Hemeg, H.A., *Nanomaterials for alternative antibacterial therapy.* Int J Nanomedicine, 2017. **12**: p. 8211-8225.
10. Makabenta, J.M.V., et al., *Nanomaterial-based therapeutics for antibiotic-resistant bacterial infections.* Nat Rev Microbiol, 2021. **19**(1): p. 23-36.
11. Lee, N.Y., W.C. Ko, and P.R. Hsueh, *Nanoparticles in the Treatment of Infections Caused by Multidrug-Resistant Organisms.* Front Pharmacol, 2019. **10**: p. 1153.
12. Attarilar, S., et al., *The Toxicity Phenomenon and the Related Occurrence in Metal and Metal Oxide Nanoparticles: A Brief Review From the Biomedical Perspective.* Front Bioeng Biotechnol, 2020. **8**: p. 822.
13. Rojas-Andrade M., N.T., Mistler W., Armas J., Lu J., Roseman G., Hollingsworth W., Nichols F., Millhauser G., Ayzner A., Saltikov C., Chen S., *Antimicrobial activity of graphene oxide quantum dots: impacts of chemical reduction.* Nanoscale Adv., 2020. **2**: p. 1074-1083.
14. Liu, S., et al., *Antibacterial activity of graphite, graphite oxide, graphene oxide, and reduced graphene oxide: membrane and oxidative stress.* ACS Nano, 2011. **5**(9): p. 6971-80.

15. Liu, S., et al., *Lateral dimension-dependent antibacterial activity of graphene oxide sheets.* Langmuir, 2012. **28**(33): p. 12364-72.

16. Fasbender, S.Z., L.; Cadeddu, R.; Luysberg, M.; Moll, B.; Janiak, C.; Heinzel, T.; Haas, R., *The Low Toxicity of Graphene Quantum Dots is Reflected by Marginal Gene Expression Changes of Primary Human Hematopoietic Stem Cells.* Scientific Reports. **9**: p. 1-13.

17. Tabish, T.A., et al., *Biocompatibility and toxicity of graphene quantum dots for potential application in photodynamic therapy.* Nanomedicine (Lond), 2018. **13**(15): p. 1923-1937.

18. Li, M., et al., *Fingerprinting photoluminescence of functional groups in graphene oxide.* Journal of Materials Chemistry, 2012. **22**(44): p. 23374-23379.

19. Liang, H.F., et al., *The band structure of graphene oxide examined using photoluminescence spectroscopy.* Journal of Materials Chemistry C, 2015. **3**(48): p. 12484-12491.

20. Veziroglu, S., et al., *Photodeposition of Au Nanoclusters for Enhanced Photocatalytic Dye Degradation over TiO2 Thin Film.* Acs Applied Materials & Interfaces, 2020. **12**(13): p. 14983-14992.

21. Lam, S.M., et al., *Degradation of wastewaters containing organic dyes photocatalysed by zinc oxide: a review.*

Desalination and Water Treatment, 2012. **41**(1-3): p. 131-169.

22. Liu, J.L., et al., *Antimicrobial Activity of Zinc Oxide-Graphene Quantum Dot Nanocomposites: Enhanced Adsorption on Bacterial Cells by Cationic Capping Polymers.* Acs Sustainable Chemistry & Engineering, 2019. **7**(19): p. 16264-16273.

23. Liu, J., et al., *Photo-enhanced antibacterial activity of ZnO/graphene quantum dot nanocomposites.* Nanoscale, 2017. **10**(1): p. 158-166.

24. Keele, B.B., Jr., J.M. McCord, and I. Fridovich, *Superoxide dismutase from escherichia coli B. A new manganese-containing enzyme.* J Biol Chem, 1970. **245**(22): p. 6176-81.

25. Marklund, S.L., *Extracellular superoxide dismutase in human tissues and human cell lines.* J Clin Invest, 1984. **74**(4): p. 1398-403.

26. Fan, T.J., et al., *Controllable size-selective method to prepare graphene quantum dots from graphene oxide.* Nanoscale Research Letters, 2015. **10**: p. 1-8.

27. Lee, S.W., et al., *Structural Changes in Reduced Graphene Oxide upon MnO2 Deposition by the Redox Reaction between Carbon and Permanganate Ions.* Journal of Physical Chemistry C, 2014. **118**(5): p. 2834-2843.

28. Yeh, T.F., et al., *Elucidating Quantum Confinement in Graphene Oxide Dots Based On Excitation-Wavelength-Independent Photoluminescence.* Journal of Physical Chemistry Letters, 2016. **7**(11): p. 2087-2092.

29. Hu, C.C., et al., *Yellowish and blue luminescent graphene oxide quantum dots prepared via a microwave-assisted hydrothermal route using H2O2 and KMnO4 as oxidizing agents.* New Journal of Chemistry, 2018. **42**(6): p. 3999-4007.

30. Toh, R.J., et al., *Transition Metal (Mn, Fe, Co, Ni)-Doped Graphene Hybrids for Electrocatalysis.* Chemistry-an Asian Journal, 2013. **8**(6): p. 1295-1300.

31. Dixon, S.J. and B.R. Stockwell, *The role of iron and reactive oxygen species in cell death.* Nature Chemical Biology, 2014. **10**(1): p. 9-17.

32. Gunther, M.R., et al., *Hydroxyl Radical Formation from Cuprous Ion and Hydrogen-Peroxide - a Spin-Trapping Study.* Archives of Biochemistry and Biophysics, 1995. **316**(1): p. 515-522.

33. Latvala, S., et al., *Nickel Release, ROS Generation and Toxicity of Ni and NiO Micro- and Nanoparticles.* Plos One, 2016. **11**(7).

34. Leonard, S., et al., *Cobalt-mediated generation of reactive oxygen species and its possible mechanism.* Journal of Inorganic Biochemistry, 1998. **70**(3-4): p. 239-244.

Chapter 2 Design of an Optimal MnO_2 Deposited GOQD Nanocomposite with Enhanced Photodynamic Activity under UV-Irradiation due to MnO_2 Deposition and Mn^{2+} Chelation

2.1 Abstract

Nanocomposites materials are highly interesting due to their synergistic properties they elicit for antibacterial applications. The leading mechanism of such synthesized nanoparticles are ROS mediated pathways, but an understanding of how the structural aspect of the nanocomposites affects the electronic distribution which affects ROS formation is lacking. In the present study, a systematic variance of MnO_2/GOQD leads to an enhancement in antibacterial efficacy as a function of MnO_2 deposition onto the GOQD. The bactericidal properties were evaluated through a minimum inhibitory concentration (MIC) and photodynamic experiment to account for the antibacterial property. At a 0.1 mg/mL concentration under UV irradiation was found to deplete bacterial cell population after 120 seconds of irradiation of 2% MnO_2/GOQD. In order

to elucidate the nanocomposites' origin of antibacterial activity methylene blue due degradation was analyzed in concert with fluorescence microscopy to determine the antibacterial efficacy. The results demonstrate the utility of both GOQD and MnO_2 as photoactive catalysts for bacterial eradication.

Chapter 2.2 Introduction

The widespread infections of Gram-positive and Gram-negative bacteria have increased medical concern for the inherent genomic resistance of bacteria. Beta-lactam antibiotics have been utilized exhaustively to induce for bactericidal activity [1-3]. While such antibiotics have traditionally experienced high antibacterial efficacy, its overwhelming use against bacteria have rendered the therapeutics ineffective. The mechanism of bacterial inhibition originates from the production of β-lactamase, which degrades β-lactam antibiotics. Therefore, while a variety of β-lactam analogues have been developed to combat the rate of bacterial mutation, such therapeutics have also decreased in its antibacterial properties [4]. Therefore, other alternative therapeutics, like inorganic nanoparticles of ZnO, CuO, TiO_2, CeO_2, SiO_2, Al_2O_3, and Fe_2O_3,

are utilized due to their antibacterial properties under steady-state conditions [5-8]. The source of antibacterial activity from these metal oxides can also be attributed to the generation of reactive oxygen species (ROS) which can be modulated based upon the nanoparticle size and metal oxide type [8]. Such nanoparticles induce antibacterial activity under dark conditions, where the production of ROS is related to the concentration of surface defects on the metal oxide surface. For instance, Lakshmi *et al.* [9] prepared ZnO nanoparticles rich with surface defects, which facilitated the production of reactive oxygen species (ROS) even in the dark, such as superoxide ($O_2^{\bullet-}$) and hydroxyl radicals ($^{-\bullet}OH$). Applerot *et al.* [10] also observed the formation of hydroxyl radical ($^{-\bullet}OH$) by ZnO nanoparticles in the dark, which led to the disruption of the electron transport chain of the Gram-negative (*E. coli)* and Gram-positive (*S. aureus)* bacteria due to the close interaction between the ZnO nanoparticles and bacterial cells. Metal oxide nanoparticles which elicit multivalent oxidation states have their antibacterial activity in the dark defined by their oxidation state. For CuO NPs the production of ROS from CuO proved to be greater in contrast to Cu_2O, although the enhanced antibacterial activity was dominated by CuO NPs. According to *Meghana et al.* the

leading cause of antibacterial activity was the chelation of Cu(I) intracellularly to critical metabolic enzymes such as fumarase[11]. Due to the short lifetime of reactive oxygen species to cell membrane interaction for antibacterial activity, lipid peroxidation may influence antibacterial activity as proved by *Krishnamoorthy et al.* with MgO NP. A lipid peroxidation assay was found to induce cell lysis as a function of a high concentration of defects on the surface of MgO NP[12]. Synthesis of Fe_3O_4 NP led to no bactericidal activity even with a concentration of 300 mg/mL against Gram-Positive *S. aureus* [13]. Regardless of the high production of $^{\cdot}OH$ from iron (II) interaction with H_2O_2 forming $^{\cdot}OH$.

Enhancement of antibacterial activity present from metal oxide nanoparticles (MONP) is exhibited from the band-gap energy of such nanoparticles. Upon irradiation the MONP may reduce or oxidize a oxygen species thereby inducing antibacterial activity. According to *Li et al.* the efficacy of photodynamic activity is a function of the amount of ROS production. Source of ROS production is controlled by the conduction band and valence band position of metal oxide as well as their respective band gap energy under photodynamic excitation [8]. The highest bactericidal activity

for metal oxide nanoparticles is categorized TiO_2 > ZnO > Al_2O_3 > SiO_2 > Fe_2O_3 > SiO_2 with highest concentration of ROS produced from TiO_2 > ZnO > Al_2O_3 > SiO_2 > Fe_2O_3 > SiO_2. An increase in ROS production is elicited by the design of doped metal oxide nanoparticles such as Cr^{3+} doped ZnO nanoparticles which enhance photodynamic activity of ZnO against *E. coli* [14]. Deposition of metal nanoparticles such as Au(0) on ZnO and Ag(0) on TiO_2 demonstrate enhancement of antibacterial activity from the deposited metal nanoparticle by varying the Fermi Energy level of the structure, thereby increasing production of oxidized solvated species like $HO^{\cdot -}$ which are produced from H_2O oxidation under UV-irradiation [15-17].

Carbon based nanomaterials are also known to provide for antibacterial and bactericidal activity. An early investigation of various carbonaceous nanostructures studied by *Garza et al.* found an early correlation between reactive oxygen species and carbon nanoparticle aggregation on A549 cells [18]. The ROS generation in A549 cells has also been found to be closely related to the mechanism of bactericidal activity under dark conditions. The effects of chemical composition, nanoparticle size, and morphology of graphene particles influences the efficacy of antibacterial

activity as well as its mode of action. Various groups have proved the efficacy of graphene sheets inducing membrane damage through a graphene sheet-to-cell membrane interaction which inhibits cell proliferation. The role of cell death from graphene nanosheet was proved to affect the metabolic capacity of the cell through an increase of glucose in *E. coli* by *Akhavan et al.* which suggests a role of reduced graphene oxide in impeding metabolic activity[19]. The efficacy of antibacterial activity of graphene nanosheets was further quantified through a minimum inhibitory concentration (MIC) experiment where the MIC of *E. coli* was found to be 1 μg/mL which outperforms kanamycin high MIC of 64 μg/mL [20]. The source of the antibacterial activity elucidated by *Krisnamoorthy et al.* was due to increasing lipid peroxidation of reduced graphene oxide[20]. Although these findings are attributed to larger graphene nanosheets in comparison to graphene oxide quantum dots where enhanced antibacterial activity is due to smaller, more oxidized graphene structures[21]. Activity of graphene oxide sheets or quantum dots can deviate from each study due to a lack of systematic control of nanomaterial composition and structure [22, 23]. Further if the procedure to measure antibacterial activity of graphene oxide is developed on

planktonic cells versus deposited cells the activity measured can differ[24].

The utility of graphene oxide and metal oxide as a nanocomposite structure for antimicrobial activity can elicit enhanced biocidal activity from both structures but may also provide a venue for improved biocompatibility. Specially since graphene oxide quantum dots (GOQD) may elicit antibacterial activity under photo excitation [25]. Use of TiO_2/graphene oxide structure for bactericidal activity was measured by *Akhavan et al.* under visible light irradiation against *E. coli* [26]. An increased concentration of sp^2 domain was found to contribute to photo-induced bactericidal activity under visible light irradiation. Enhanced visible light absorption of TiO_2 deposited on Graphene Oxide (GO) is improved by the metal oxide reduction procedure [27]. Antibacterial activity of ZnO_2 deposited on GO has been quantified for Gram-Negative and Gram-Positive bacteria for their antibacterial activity under dark conditions [28, 29]. The MIC for ZnO_2/GO is measured between 5 µg/mL to 3.2 mg/mL, while the photodynamic activity reported for TiO_2/GO and ZnO_2/GO varies based on the wavelength of excitation.

Although the antibacterial efficacy of both metal oxides and organic nanoparticles has been documented for various nanomaterials, a high nanoparticle concentration is necessary to exert bactericidal activity under ambient conditions (>1 mg/mL). Such a high concentration of insoluble metal oxide nanoparticles can lead to increased cytotoxicity for medical treatment. The inherent solubility of oxidized graphene nanoparticles is a desirable substrate which metal oxide nanoparticles have been deposited onto for energy and catalytic applications.[30-34] Recently, in a study by *Liu et al.*[29] the antibacterial properties of a ZnO/GOQD nanocomposite was reported to have an MIC at 3.6 mg/mL. While the MIC proved to be higher for the ZnO/GOQD (3.6 mg/mL), in contrast to the MIC of ZnO (1.2 mg/mL). Its inherent solubility due to the ZnO/GOQD design leads to an ideal biomaterials candidate for systemic antibacterial treatment.

The antibacterial property elicited by ZnO/GOQD is not limited to ambient conditions. In a concentration of 1 mg/mL and under 365 nm irradiation of 100W light the antibacterial activity of the ZnO/GOQD was improved, in comparison to ZnO and GOQD. Band-gap energy of the ZnO can induce a photodynamic effect when excited at an energy

greater than the near-edge absorption of the metal oxide. Since metal oxides can exhibit a high band-gap energy, the design of a nanocomposite with a decrease in the band-gap energy is desirable in order to increase its biocompatibility.

Photodynamic activity of metal oxide deposited on graphene oxide has mainly been studied with metal oxides with one valence state. In a study by *Goncalves Jr. et al* a Hausmannite Mn_3O_4 nanoparticle exhibits electron transfer from Mn^{2+} to Mn^{3+} analyzed from the DOS from both Mn ions in the valence and conduction band. Furthermore, preferential adsorption of H_2O and desorption of $^{-}{}^{\cdot}OH$ on Mn^{2+} with -16.5 kcal/mol and -11.3 kcal/mol for each respective process[35]. A Mn^{2+} chelated GOQD structure has been hydrothermally synthesized by *Gan et al.* which is characterized with a charge transfer mechanism from Mn^{2+} to sp^2 sites on GOQD [36]. An optimal MnO_x deposited on GOQD could be synthesized by tuning an optimal concentration of Mn^{2+} within the MnO_x and GOQD structure in order to induce electron transfer from GOQD to the MnO_x. Previous experiments have demonstrated the antibacterial capacity of MnO_x nanoparticles when deposited on chitosan against Gram-negative and Gram-positive bacteria [37] but their MIC and photodynamic activity of MnO_x has not been

quantified. Furthermore the potential for application as a wound-based therapeutic is supported by the low percentage of hemolysis measured from erythrocytes [38].

In order to understand the synergistic effect of metal oxides and graphene oxide nanomaterials a series of MnO_2/GOQD nanocomposites were designed. The widespread use of MnO_2 deposition on GOQD from a solution driven reduction of Mn^{7+} to Mn^{4+} with the corresponding oxidation of reduced carbon to oxidized carbon makes it a facile and industrial level synthesis for antibacterial applications.

(1) $4MnO_4^- + 3C + H_2O \rightarrow 4\ MnO_2 + CO_3^{2-} + 2HCO_3^{2-}$

To control the extent of MnO_2 deposition, the ratio of the Mn precursor was increased with a constant concentration of GOQD. Upon heating at 60 ºC for two hours and after purification process the resulting solution was a translucent brown solution. TEM proved that MnO_2 nanorods with an average length of 14 to 16 nm and cross-sectional diameter of 2-3 nm were synthesized on the GOQD sheets for the 80% $KMnO_4$ to GOQD sample. The

antibacterial activity of the obtained MnO_2/GOQD nanocomposite was assessed and compared in ambient light and under UV irradiation. Enhancement was observed for an increase in deposited MnO_2 on the GOQD nanoparticle for both photodynamic and concentration dependent bactericidal activity.

2.3 Experimental Section

2.3.1 Chemicals

Potassium permanganate ($KMnO_4$, 99.0%), manganese sulfate ($MgSO_4$, 99.0%), pitch carbon fiber, potassium phosphate monobasic (KH_2PO_4, 99.0%), potassium phosphate dibasic (K_2HPO_4, 98.0%), nitric acid (HNO_3, 70%), ethylenediaminetetraacetic acid disodium salt dihydrate (EDTA-2Na, 99.0%), tert-butanol (TBA, 99.5%), and methylene blue dye (82.0%) were all purchased from Acros or Sigma Aldrich. Water was purified with a Barnstead Nanopure Water System (18 M Ω cm).

2.3.2 GOQD Synthesis

The synthesis of GOQD has been detailed previously [39, 40]. In brief, pitch carbon fiber (1 g) was immersed into a mixture of concentrated HNO_3 (40 mL) and H_2SO_4 (60 mL) in a round-bottom flask. After two hours of sonication, the carbon fibers were refluxed at 120 °C for 24 h. Once the solution was cooled to room temperature, its pH was adjusted to pH 7 with NaOH. The solution was left overnight to allow for salts to precipitate out of solution. The supernatant, which contained water-soluble GOQDs, was collected and transferred to a cellulose dialysis bag and placed in Nanopure water for several days to afford purified GOQD.

2.3.3 MnO_2/GOQD Synthesis

The GOQDs obtained above were then used for the preparation of GOQD/MnO_2 composites. In separate round-bottom flasks, a calculated amount of $KMnO_4$ (10.5, 21.0, 60.1, 180.2, and 300.0 mg) was dissolved in 500 mL of Nanopure water, into which was then added 50 mg of GOQDs under sonication for 2 h. Then, the mixture was heated for two hours at 60 °C. When cooled down naturally to room temperature, the mixture was placed in a cellulose bag for dialysis for three days, with a regular change of the water every 4 h. Five samples were prepared at different $KMnO_4$

feed ratios and denoted as GOQD/MnO_2-a, GOQD/MnO_2-b, GOQD/MnO_2-c, GOQD/MnO_2-d, and GOQD/MnO_2-e. To remove MnO_2 from the nanocomposite, the GOQD/MnO_2-c sample was mixed with 0.1 M HNO_3 under magnetic stirring for 2 h, and then dialyzed for 6 h in Nanopure water. Acid treatment of GOQDs was carried out in the same manner.

2.3.4 Characterization

The morphology and size of the samples were characterized by transmission electron microscopy measurements (TEM, Phillips CM 300 at 300 kV). UV-vis absorption spectra were acquired with a Perkin Elmer Lambda 35 UV-vis spectrophotometer, and photoluminescence measurements were conducted with a PTI fluorospectrophotometer. X-ray photoelectron spectra (XPS) were recorded with a PHI 5400/XPS instrument equipped with an Al K_α source operated at 350 W and 10^{-9} Torr. Time-resolved photoluminescence decay spectra was collected on a Horiba QM-3304 instrument at the pulsed laser excitation of 335 nm in the time-correlated single-photon counting (TCSPC) mode. Electron paramagnetic resonance (EPR) experiments were carried out with the MnO_2/GOQD-x series 63 K with a Bruker EMX EPR spectrophotometer operating at the X-band

frequency (~9.4 GHz) using an ER 4122SHQE resonator (Bruker).

2.3.5 Antimicrobial evaluation

E. coli cells were grown in Luria Broth (LB) agar in a 37 °C incubator. A single colony was selected and used to inoculate 3 mL of liquid LB and allowed to shake at 37 °C for 18 h. The resulting liquid was centrifuged at 5000 rpm for 5 min and resuspended in Nanopure water to an optical density of 0.1 at 600 nm. To determine the MIC, a 96-well plate was used to conduct a kinetic cell growth experiment in the dark at 37 °C. Each well was filled with a total volume of 200 µL with 30 µL of sterile LB, 10 µL of bacterial solution, and varied volumes of the GOQD samples prepared above. Sterile Nanopure water was used to bring the total volume in each well to 200 µL. Upon inoculation, the 96-well plate was placed in a Molecular Device VERSA max microplate reader, where the optical density (OD) was measured at 600 nm every minute and 30 seconds with intermittent shaking between each reading over a 24-hour incubation period. In photodynamic antibacterial assessments, 200 µL of *E. coli* (OD 0.1) was transferred to a 1 mL plastic centrifuge tube, into which 600 uL of 0.1 mg/mL the GOQD samples was added along with 200 µL of sterilized Nanopure water. For

the MnO_2 nanocatalyst, 6 mg of the sample was added to 1 mL of *E. coli* with sterilized Nanopure water solution. The centrifuge tubes containing the *E. coli* and nanoparticles were irradiated with UV photoirradiation (100 W, 1000-1500 lumen with a peak emission at 365 nm, Dongguan Hongke Lighting Co, China). After irradiating the sample, each centrifuge tube was diluted by 100 folds at each respective time point. From the diluted solution, 10 µL was distributed evenly on an LB agar plate utilizing sterilized glass beads. Upon dispersion of nanoparticle and *E. coli* suspension on the LB agar plate, the agar plates were placed in a 37 °C incubator.

2.3.6 Methylene blue photodegradation

Photocatalytic degradation of methylene blue was carried out by following a procedure described previously.[41] Experimentally, a calculated amount of methylene blue (MB 450 uM) was diluted to 3mL in a quartz cuvette to 45 uM with a corresponding sample prepared above. A volume of 140µL of 1.0 mg/mL concentration of GOQD/MnO_2-c and GOQD was added to a total volume of 3 mL pH 7.2 with 45 uM methylene blue , where the pH was made with a potassium phosphate monobasic and potassium phosphate dibasic

buffer. A 6 mg MnO_2 nanoparticle control sample was tested with pH 7.2 at a concentration of 45uM. For the methylene blue dye control, the volume of photocatalyst was supplemented with pH 7.2 buffer. The solution was then irradiated with a 365 nm LED lamp, and UV-vis spectra were acquired at different time intervals. Similar procedure was carried out with photocatalyst and experimental conditions with the addition of 300 µL of 6 mM EDTA.

2.4 Results and Discussion

Figure 1 shows GOQD/MnO_2-c produced from a feed ratio of 48.38% Mn/GOQD wt%. The production of MnO_2 is apparent from the needle structure present from the dark wires on from Figure 1a. The interplanar distance of 0.234 nm corresponds to a lattice (211) which is present in α-MnO_2 nanowires (Figure 1b) [42-45]. Nucleation of MnO_2 utilizing $KMnO_4$ as a precursor is an oxidation process which has been observed for a variety of GOQD structures[46] [36, 47, 48]. MnO_2 nucleation occurs along the edges of the GOQD structure via the oxidized moieties of graphene oxide [47] . The thermodynamic force of reduction from Mn^{7+} to Mn^{4+} is driven by GOQD oxidation and solvent composition[49]. The formation Mn^{7+} to Mn^{4+} is specifically due to reduction from isolated double bonds which lead to an eventual ketone [50].

Therefore, GOQDs provide a viable precursor for MnO_2 growth due to the nucleation sites and the redox active sites leading to MnO_2 growth.

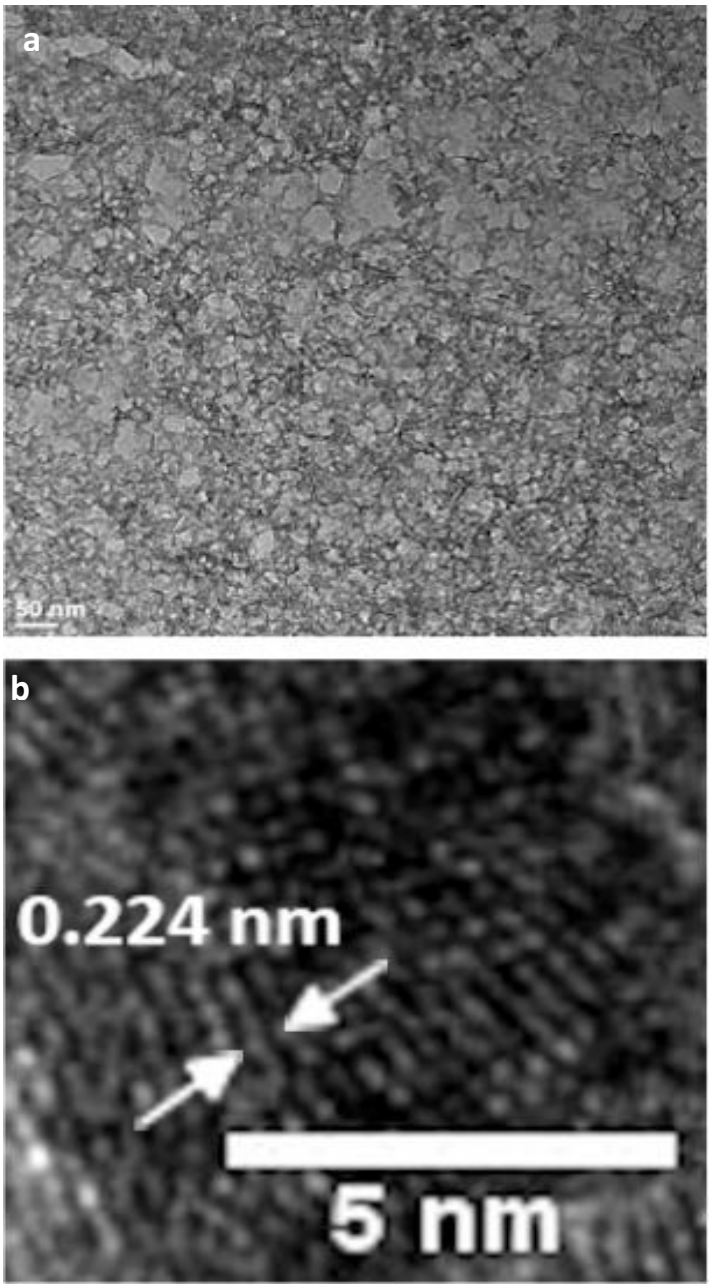

Figure 1. Representative TEM images of the a) GOQD/MnO_2-c and b) lattice fringes of GOQD/MnO_2-c

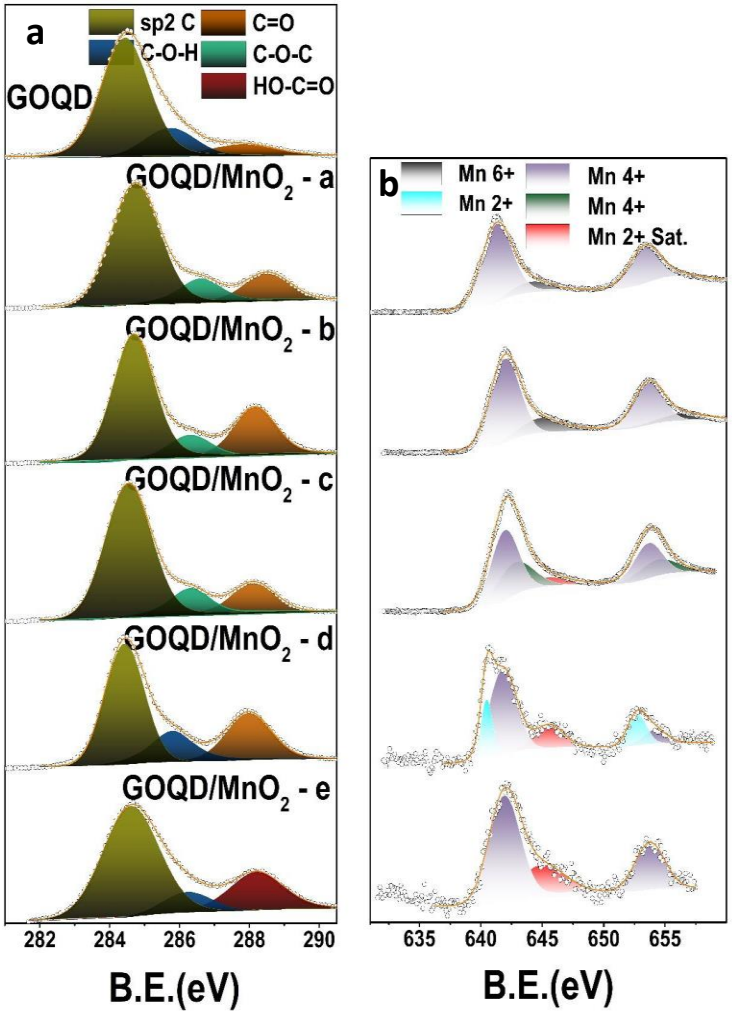

Figure 2: XPS of (a) High resolution C1s spectra for GOQD and GOQD/MnO_2-x samples, (b) Mn2 p spectra for GOQD and MnO_2/GOQD-x samples

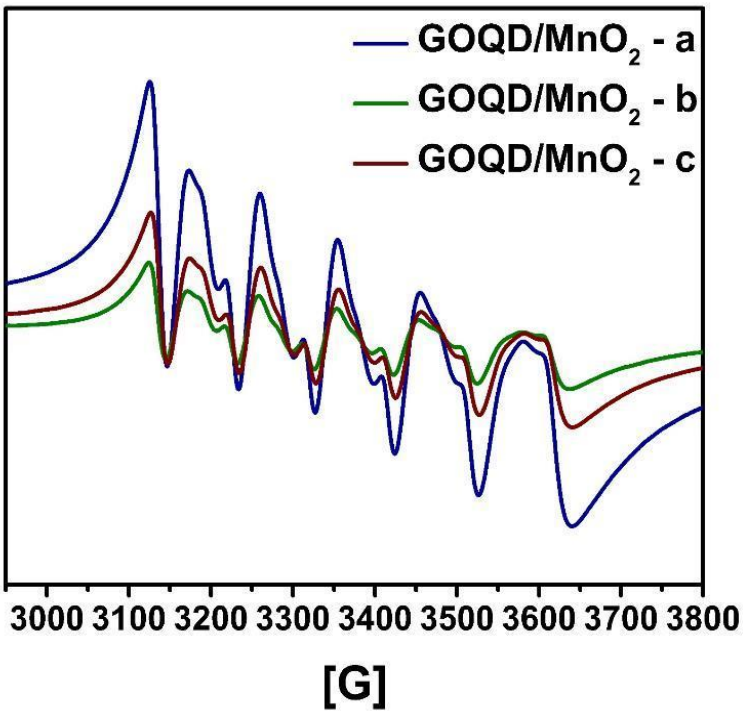

Figure 3: EPR Spectra of GOQD/MnO_2-a , GOQD/MnO_2-b , and GOQD/MnO_2-c

Time Resolved Fluorescence Lifetime Decay measured at an excitation wavelength of 365 nm for GOQD, GOQD/MnO_2-a, GOQD/MnO_2-b, and GOQD/MnO_2-c optimal concentration of MnO_2 deposited on GOQD is defined by the high level of dispersion as depicted from Figure 1a. A high concentration of MnO_2 deposited on GOQD is desirable due to the increased photocatalytic sites required for reactive oxygen species formation. Although an increased feed ratio of $KMnO_4$ to GOQD does not translate with increased MnO_2 deposition onto GOQD (Table S6). Furthermore, the total percentage of Mn^{n+}/Mn measured from Mn 2p XPS (Figure 2b) solely attributed to Mn^{4+} is demonstrated in GOQD/MnO_2-c and GOQD/MnO_2-e only. Also, the highest

extent of MnO_2 deposition onto GOQD is present in GOQD/MnO_2-c with a %Mn/C = 7.85%. Therefore, the optimal feed ratio produces a high degree of MnO_2 nanowires with no variation in Mn valency or Mn oxide. Due to the oxidative properties of $KMnO_4$, increasing concentrations of $KMnO_4$ leads to a higher degree of oxidized groups on GOQD structure (Figure 2a) [51-53].

As the graphene sheet becomes more oxidized the size of the GOQD also decreases which more evenly distributes HO-C=O moieties. The extent of carbon oxidation from GOQD substrate can be measured from a decrease in sp^2 carbon GOQD/MnO2-cconcentration and increase in the C-OH, C-O-C, C=O, and HO-C=O concentration. In Figure 2a the sp^2 character from the GOQD substrate composes 78.37% of the carbon structure. Increasing feed ratio of $KMnO_4$ lead to a decrease in sp^2 character of GOQD as calculated from C1s spectra from XPS (Table S4). Furthermore, the type of oxidized carbons changes with increasing $KMnO_4$. In samples GOQD/MnO_2-a,b, and c the prevalent oxidized carbon species become C-O-C and C=O (Figure 2a). Appearance of C-O-C is attributed to the cis-diol formation formed from oxidation of $KMnO_4$ via carbon double bonds. A higher extent of oxidation is present in

GOQD/MnO_2-d and GOQD/MnO_2-e which is attributed to a low sp^2 or high HO-C=O content (Table S4). A high extent of oxidation may lead to disruption of the sp^2 domains which contain the π-orbitals required to produce the quantum transitions produced via UV excitation.

The deposition of MnO_2 onto GOQD can be measured via UV-VIS by measuring the peak absorbance around 400 nm which is attributed to d□d orbital transition of octahedral Mn[54, 55]. The most prominent absorption at 400 nm is present in GOQD/MnO_2-c (Figure S1a). Further the absorption of GOQD/MnO_2-c extends from 2.75 eV to 4.8eV based on its measured Tauc's plot, which is broader in its absorption region in contrast to GOQD's of 3.2 eV to 3.8eV (Figure S1b). A decrease in the band-gap energy of GOQD/MnO_2 is attributed to MnO_2 nanorod production on the GOQD substrate[56, 57] [58]. The increase in the band-gap range from 3.8 eV to 4.8 eV is due to oxidation of GOQD structure which lead to a decrease in sp^2 domains of GOQD therein increasing band-gap energy of GOQD[59, 60]. A continuous increase in band-gap energy is present gradually

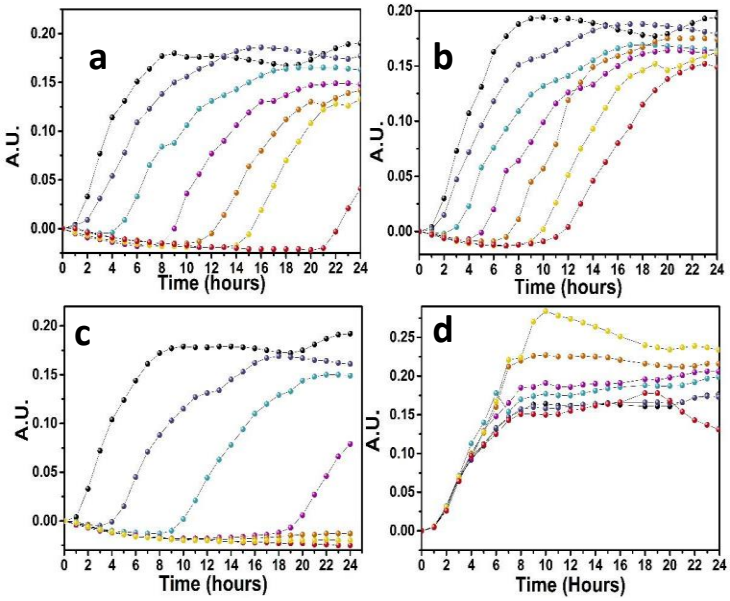

Figure 4 Minimal Inhibitory Concentration (MIC) measurements of *E. coli* with various GOQD/MnO_2 samples in the dark: (a) GOQD/MnO_2-a, (b) GOQD/MnO_2-b, (c) GOQD/MnO_2-c, and (d) GOQD with concentrations of: black circle 0 mg/mL, navy blue 1.25 mg/mL, cyan 2.5 mg/mL, purple 4 mg/mL, orange 5 mg/mL, yellow 7 mg/mL, and red 8 mg/mL

from GOQD/MnO_2-a to GOQD/MnO_2-e due to various extent of $KMnO_4$ oxidation (Table S1). Therefore, while proving to be a facile process for MnO_2 growth, a high extent of GOQD oxidation may affect sp^2 electronic transition.

The fluorescence profile of GOQD illustrates how oxidation of GOQD and MnO_2 deposition affects its electronic transitions. In Figure 3a GOQD contains two prominent peaks

at 335 nm and 465 nm which are either due to $\pi \rightarrow \pi^*$ or $n \rightarrow \sigma^*$ from sp^2 or sp^3 domains of GOQD. The normalized fluorescence intensity of GOQD/MnO_2-a and GOQD/MnO_2-b excited at 365 nm is similar or higher in contrast to GOQD. The

increase in photoluminescence can be attributed to a transition from Mn^{2+} to GOQD's π^* system [36]. The presence of Mn^{2+} is exhibited by the six hyperfine peaks exhibited from samples MnO_2/GOQD-a, MnO_2/GOQD-b, and MnO_2/GOQD-c (Figure 4) which have been exhibited by the incorporation of Mn^{2+}within a metal oxide lattice [61]. Based on a study by *Gan et al*. the excitation of Mn^{2+}-RGO from 360 nm to 400 nm lead to an allowed $^6A^1 \rightarrow {}^4T_2$ transition (Figure 3a). For the GOQD/MnO_2-a and GOQD/MnO_2-b samples the average excitation wavelength increases from 342 nm to ~ 360nm (Figure 3a). A broad excitation peak at 360nm corresponds to Mn^{2+}allowed $^6A^1 \rightarrow {}^4T_2$ transition which occurs within an excitation wavelength of 360-400nm. The corresponding emissions of the nanocomposites becomes centered at 515 nm in contrast to the 488 nm emission of the GOQD excited at 342 nm (Figure 3a). The emission average centered around 515 nm is attributed to the emission of the $\pi^* \rightarrow \pi$ from

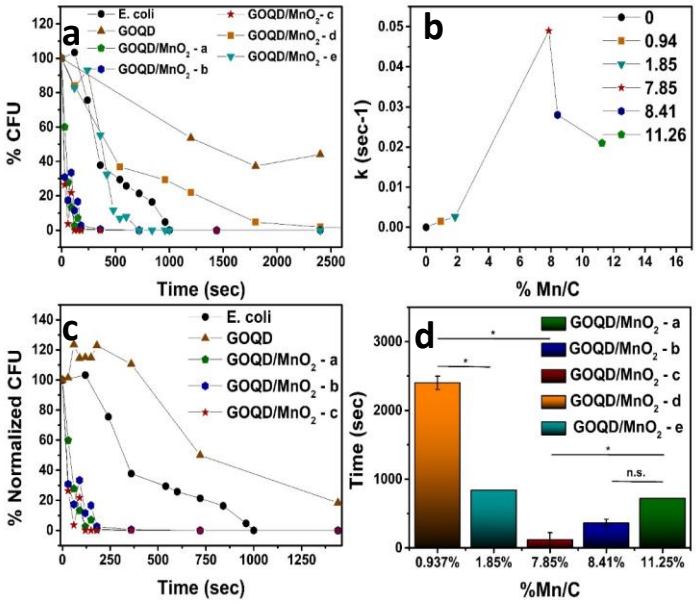

sp^2 domains in GOQD [62]. Therefore a red shift in excitation wavelength and increase in normalized fluorescence intensity for GOQD/MnO_2-a and GOQD/MnO_2-b is due to

Figure 5. (a,c) Photodynamic curves measured from Colony Forming Units (CFU) inoculated on Luria Bertani Broth (LB) after 16 hours incubation. (b) Rate of E. coli cell death as a function of 365 nm excitation irradiation. d) Time of Cell Death (TCD) measured from all MnO_2/GOQD -x samples after irradiation. Statistical significance was evaluated by two-tailed t-tests

Mn^{2+} electron transfer to π^* system of GOQD. In samples GOQD/MnO_2-c, and d the excitation at 465 nm disappears due to oxidation of larger sp^2 domains leading to such excitations or quenching of such transitions due to MnO_2

deposition. The GOQD/MnO_2-e sample contains no fluorescence at an excitation wavelength of 365 nm which can be attributed to a large extent of oxidation as evidenced by the low concentration of MnO_2 deposition and high carbon oxidation as measured from Mn 2p and C1s XPS.

The quenched emission for MnO_2/GOQD-c could be due to an efficient electron-hole separation due to the low extent of sp^2 oxidation and high percentage of MnO_2 [63]. The measured fluorescence lifetime constants for GOQD/MnO_2-c is greater (τ_c = 2.56 ns) in contrast to GOQD, GOQD/MnO_2-a, and b (Table 1). Furthermore, oxidation of GOQD/MnO_2-c via HNO_3 diminishes the fluorescence lifetime constant measured at 365 nm excitation ($\tau_{HNO3\ c}$ = 2.28 ns). A decrease in fluorescence lifetime constant due to HNO_3 treatment of GOQD/MnO_2-c indicates the MnO_2 and GOQD chemical interaction leads to enhanced electron-hole separation. Also, the reconstitution of 465 nm excitation and its respective emission peak for HNO_3 GOQD/MnO_2-c (Figure S2b) confirms the MnO_2 and GOQD interaction.

(2) $$y = Ae^{-bt} + Ce^{-dt}$$

(3) $$\sum \quad \tau = \sum_{i=1}^{n} \quad A_i \tau_i$$

The antibacterial activity of GOQD/MnO_2 was quantified by utilizing a Minimal Inhibitory Concentration Method (MIC) [64-66]. The MIC was measured by monitoring the growth of *E. coli* in liquid media over time. Figure 5 show the antimicrobial activity of *E. coli* in LB for GOQD/MnO_2-x and GOQD. The lowest MIC is exhibited for GOQD/MnO_2-c with %Mn/C = 7.85 % (Figure 5c). The GOQD/MnO_2-a and GOQD/MnO_2-b with %Mn/C = 8.42% and 11.26% have no MIC at or lower concentrations than 8 mg/mL (Figure 5 a,b). Although both GOQD/MnO_2-a and GOQD/MnO_2-b exhibit an increase in lag time (t_L) as a function of GOQD/MnO_2 concentration. At a concentration of 8 mg/mL GOQD/MnO_2-a t_L = 21 hours while GOQD/MnO_2-b t_L = 9 hours (Figure 5 a,b) . For most GOQD/MnO_2-x samples, excluding GOQD/MnO_2-c, a low MIC is defined by a high concentration of %Mn/C. Although GOQD/MnO_2-c contains a total Mn^{4+} concentration of 100%, the dispersion of MnO_2 on GOQD can be attributed to the enhanced interaction of the MnO_2 with the bacterial cell wall. Evidence of improved dispersion is rationalized by the absence of antibacterial activity from GOQD which suggests MnO_2 concentration is not a sole indicator of high

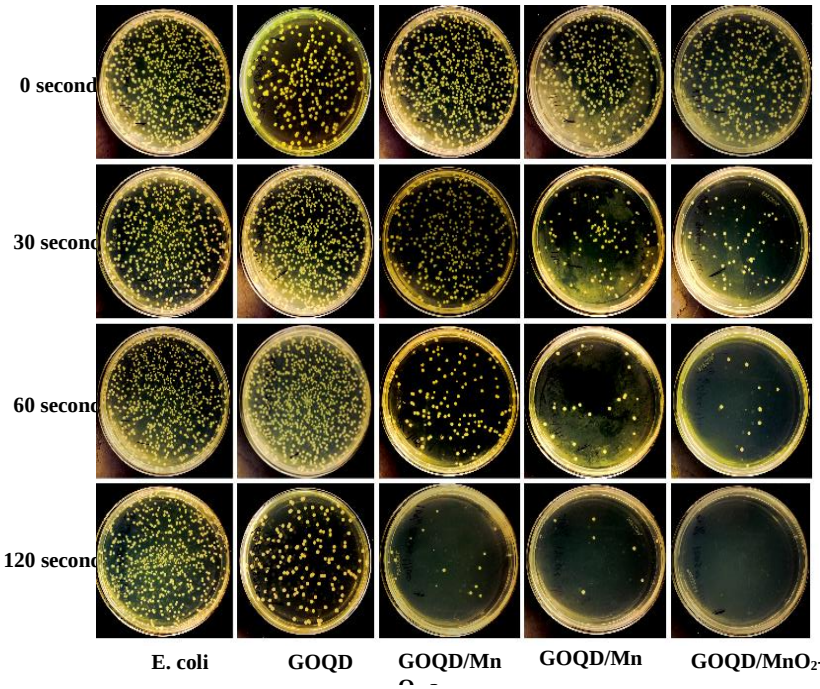

Figure 6: Photographs of *E.coli* with GOQD, GOQD/MnO_2-x, and in absence of catalyst after excitation at 365 nm at respective time points

antibacterial activity (low MIC and high t_L). The enhanced antibacterial properties of metal oxide against gram-negative and gram-positive bacteria due to structural damage of the cell wall or dissolution of metal ions is the attributed antibacterial mechanism for metal oxide nanoparticles[5-7, 10, 11, 67-69]. For ZnO nanoparticles, dissolution of ZnO into Zn^{2+} is an energetically low expenditure thermodynamic process since its ΔH_{Me+} is 662 kcal mol^{-1} [5]. A higher valence metal oxide, such as TiO_2, SiO_2 , and Fe_2O_3 , have relatively low MIC due to the high valency of the metal. Increase in the metal oxide's oxidation state will decrease the ionization energy, which is the origin of the high MIC values for the x%

GOQD/MnO_2 samples in contrast to other nanocomposites [29, 68].

The photodynamic studies were conducted to quantify the antibacterial property of the GOQD/MnO_2 system under UV excitation. To prevent the antibacterial activity of GOQD/MnO_2-x in ambient condition, the photodynamic experiments were run at a concentration of 0.1 mg/mL for all samples. The time of cell death (TCD) and rate of cell death (RCD) was determined by counting the

Colony Forming Units (CFU) and normalizing to the (CFU) at their initial time point. The TCD for the x% MnO_2/GOQD increased as follows: MnO_2/GOQD-c < MnO_2/GOQD-b < MnO_2/GOQD-a < MnO_2/GOQD-d < E. coli < MnO_2/GOQD-e < GOQD (Figure 6a,b). While GOQD is known to elicit antibacterial activity against Gram-Negative bacteria [21, 22, 24, 70, 71], a larger and more reduced GOQD will have decreased antibacterial activity and can even induce cell growth [72]. Photodynamic activity of MnO_2/GOQD follows an volcano relationship as a function of %Mn/C with an optimal loading of Mn^{4+} at 7.85% %Mn/C (Figure 6d).

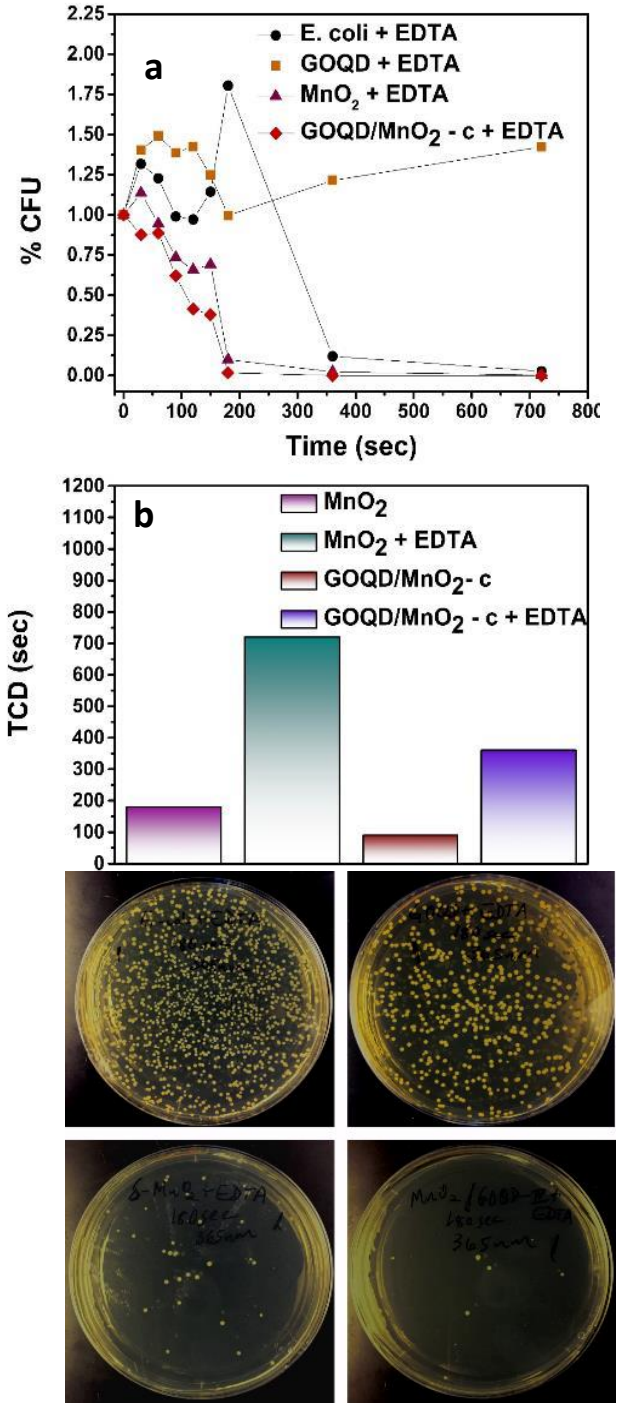

The optimal percentage of MnO_2 deposited on GOQD for photodynamic activity at an excitation of 365 nm occurs at

Figure 7: a) Photodynamic activity of *E.coli* with GOQD,

Figure 7: a) Photodynamic activity of *E.coli* with GOQD,

MnO_2, GOQD/MnO_2-c, and in the absence of photocatalyst with EDTA b) TCD measurements for *E.coli* with MnO_2 and GOQD/MnO_2-c with and without EDTA c) CFU of *E.coli*

MnO_2, GOQD/MnO_2-c, and in the absence of photocatalyst with EDTA b) TCD measurements for *E.coli* with MnO_2 and GOQD/MnO_2-c with and without EDTA c) CFU of *E.coli*

7.85% of total Manganese per total carbon composition from the GOQD. Analysis of the Manganese oxidation state demonstrates that a higher concentration of Mn^{4+} leads to enhanced photodynamic activity. The nature of the enhancement can be attributed to 1) Enhanced electron excitation process within the Manganese Oxide and 2) intersystem crossing from GOQD to MnO_2 structure. Photocatalytic studies of Manganese Oxide demonstrate the role of a high valent Manganese in the oxidation of organic molecules such as phenols [73] . The MnO_2 valence band is mainly composed of O2p orbitals, while the conduction band is mainly composed of Mn 3d orbitals[74] [75]. Therefore a MnO_x nanostructure with a higher concentration of Mn^{4+} yields higher vacancy for electrons from the valence band O2p of MnO_x nanostructures. Furthermore, charge mobility within the MnO_x is defined by the conversion of higher valent

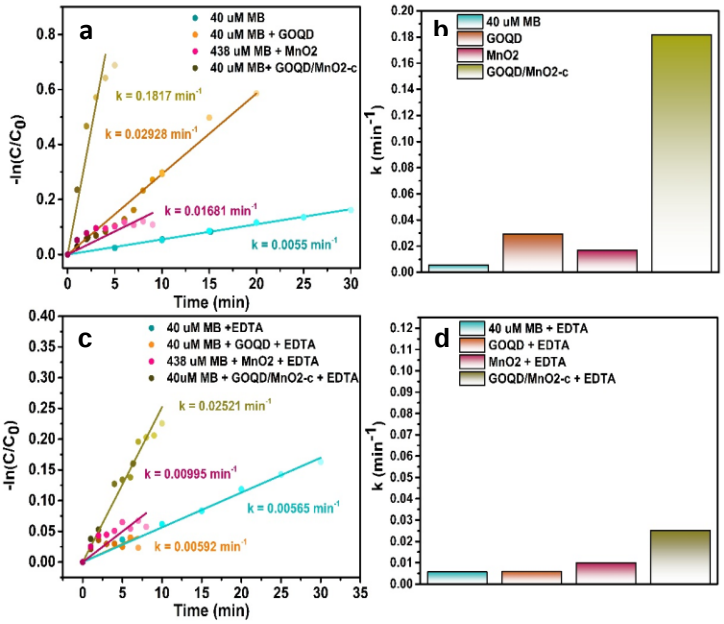

Figure 8: a,b) Calculated Rates of Methylene Blue Dye Degradation for GOQD, MnO_2, and GOQD/MnO_2-c c,d) Calculated Rates of Methylene Blue Dye Degradation for GOQD, MnO_2, and GOQD/MnO_2-c with EDTA

Mn^{4+} into Mn^{2+} as evidenced by the degradation of phenol from *Zhang et al.* were metal oxide nanoparticle with the highest degradation of phenol was correlated with an increase in Mn^{2+}.The optimal GOQD/MnO_2-c contains the highest lifetime constant for the GOQD/MnO_2 series which can be attributed to an effective number of MnO_2 sites acquired to induce electron-charge separation.

Therefore due to the high concentration of Mn^{4+} and dispersed concentration of the GOQD/MnO_2-c induces

at 532 nm.

enhanced photodynamic activity. To identify the mechanism of photodynamic activity under UV irradiation, the

GOQD/MnO_2-c nanocomposite was irradiated in the presence of EDTA (Figure 10 a,b). The interaction of EDTA with the holes of MnO_2 would lead to a depletion of holes from MnO_2 produced under UV-irradiation of the nanocomposite. The facile kinetics of EDTA with holes from a on deposited metal oxide has been measured by *Silva et al.* where Au/TiO_2 in the presence of EDTA using monochromatic laser pulses

Luria Broth Agar taken at 180 seconds for *E.coli*, d) GOQD, e) MnO_2, and f) GOQD/MnO_2-c all done in the presence of EDTA Due to the percentage of Au deposited onto the TiO_2 structure a higher volume of H_2 (mL) were produced on the surface of the metal doped metal oxide structure. An essential aspect is the high yield of H_2 obtained from the nanocatalyst by preventing adsorbed H_2O from interacting with the hole of TiO_2 to form $HO^{\cdot -}$. Instead EDTA is oxidized to $EDTA^{\cdot +}$ which prevents electron-hole recombination and a high yield of H_2 production from the nanomaterial[76]. The

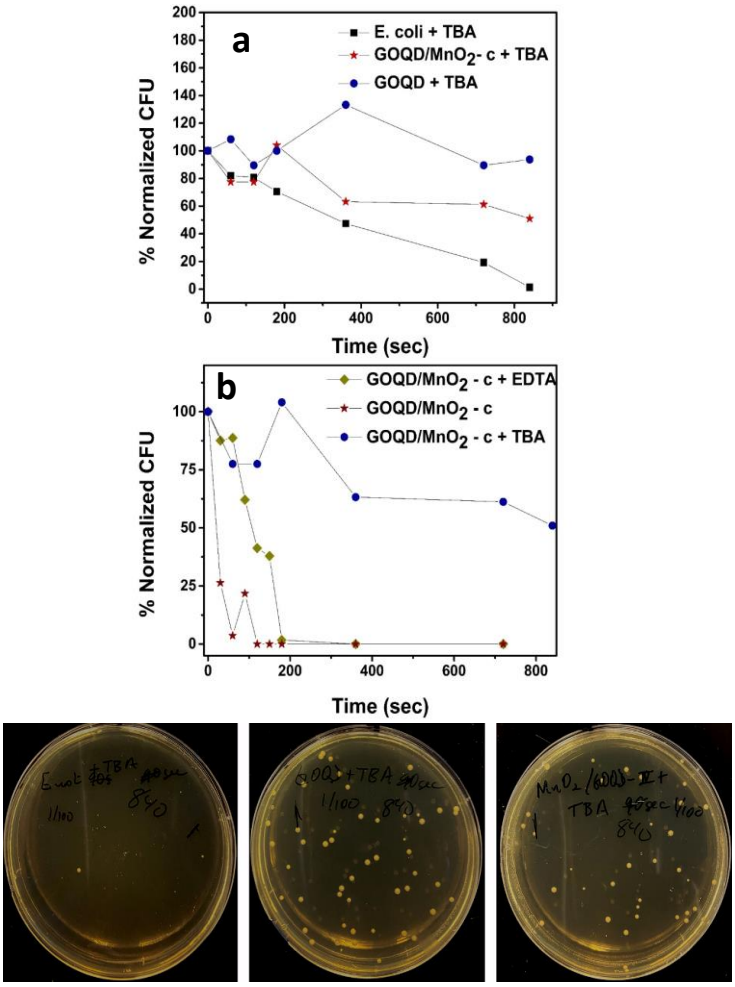

TCD of GOQD/MnO_2-c with EDTA increases fourfold to 360

Figure 9: (a) Normalized Colony Forming Units with *E.coli* + tert-butyl alcohol (TBA), GOQD/MnO_2-c + TBA, and GOQD + TBA with a 365 nm LED for respective time points d) GOQD with TBA and e) GOQD/MnO_2-c with TBA enumerated after 16 hr

seconds in contrast to the photodynamic activity of GOQD/MnO_2-c of TCD = 90 seconds (Figure 10 a,b). The images of CFU more clearly depicts the presence of *E.coli* for

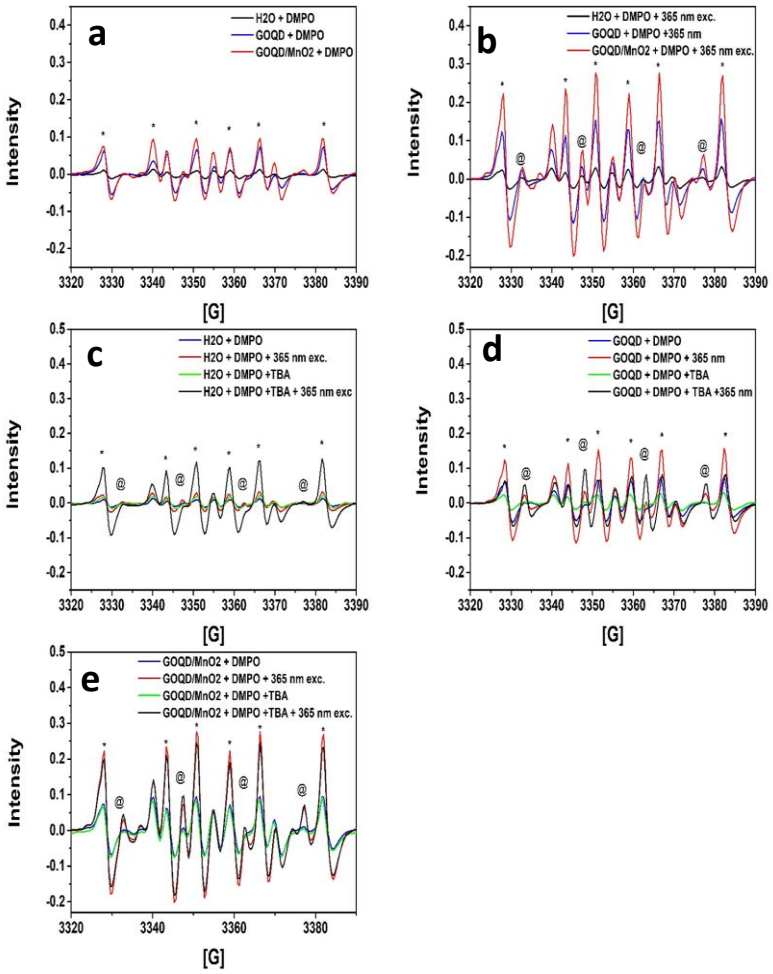

Figure 10: EPR spectra of H_2O, GOQD, and GOQD/MnO_2-c under a) steady state condition, b) excited by 365 nm LED, and c,d,e) in steady state and excited at 365 nm and treated with TBA an active site on GOQD/MnO_2-c.

EDTA treated GOQD/MnO_2-c upon 150 seconds of irradiation (Figure 8 c). The inactivity of GOQD/MnO_2-c illustrates the importance of MnO_2 as Normalized Colony Forming Units

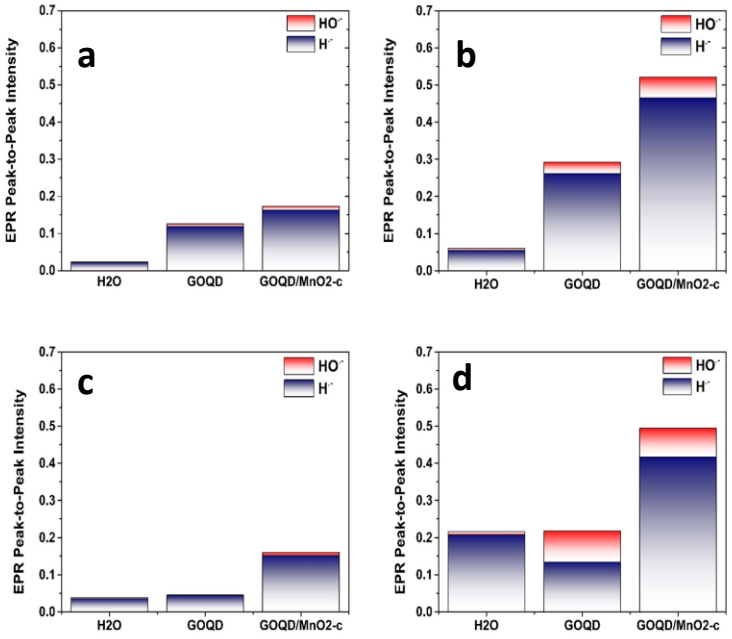

Figure 11: EPR Peak-to-Peak intensity spectra of H_2O, GOQD, and GOQD/MnO_2-c under a) steady state condition, b) excited by 365 nm LED, c) steady state condition in the presence of TBA, and d) excited by 365 nm LED in the presence of TBA

(CFU) of E. coli and GOQD/MnO_2-c after 365 nm irradiation with TBA, EDTA, and no radical scavenger enumerated after 16 hrs. of incubation. c) Photographs of E. coli with TBA and

. incubation once irradiated at 365 nm at 840 seconds

Although presence of a lower TCD indicates the relevance of oxidized GOQD as an active site appears relevant due to the newly developed TCD of 360 seconds for GOQD/MnO_2-IV upon treatment with EDTA (Figure 9b). The TCD of HNO_3 GOQD ($TCD_{HNO3\ GOQD}$ = 360 sec) demonstrates oxidation of sp^2

and sp^3 carbons activity of oxidized carbon can be attributed to an increase in hydroxyl groups present in both HNO_3 GOQD and HNO_3 GOQD/MnO_2- of GOQD which leads to photodynamic enhancement similar to the HNO_3 treated GOQD/MnO_2-c ($TCD_{HNO3\ GOQD/MnO2\text{-}c}$ = 360 sec) (Figure S6a,b). The enhancement in photocatalytic for both HNO_3 GOQD and HNO_3 GOQD/MnO_2-c contain 41.18% and 42.55% elemental composition of hydroxide, respectively.

In contrast to GOQD and GOQD/MnO_2-c the elemental compositions of hydroxide are 12.37% and 0% respectively (Table S4). In a study by *Rojas-Andrade et al.* a GOQD structure with higher concentrations of hydroxides conjugated with aliphatic carbons produced enhanced photodynamic activity at 400 nm excitation due to hydroxide radical production[77]. The photocatalytic activity is driven via lysis of HO bonded to aliphatic GOQD which is supported by the similarity of fluorescence lifetime constants between GOQD and HNO_3 GOQD (Figure S3).

To more closely inspect the role of GOQD from the GOQD/MnO_2-c structure in the photocatalytic driven cell death of *E. coli* the latter structure was photoexcited at 365 nm with methylene blue dye [78-80] Since enhanced

photocatalytic activity of methylene blue dye is driven by production of reactive oxygen species, examining the photoactivity of GOQD/MnO_2-c and methylene blue dye can further elicit the mechanism of photocatalytic cell death. In contrast to GOQD and MnO_2 the degradation of methylene blue of GOQD/MnO_2-c is enhanced in contrast to GOQD and MnO_2 tested independently (Figure 8a,b). In the presence of EDTA the photoactivity of GOQD, MnO_2, and GOQD/MnO_2-c are diminished due to the scavenging activity of holes (Figure 9c,d). Although in contrast to GOQD and MnO_2 photoactivity of methylene blue dye in the presence of EDTA, the photoactivity of GOQD/MnO_2-c remains enhanced in contrast to both independent catalysts. The source of the photocatalytic activity cannot be the photolysis of HO- from vinyl groups since the photocatalytic degradation of methylene blue dye from GOQD is driven by hole generation (Figure 9). Furthermore, the concentration of hydroxide is too low to have an observable effect on the photocatalytic generation of hydroxyl radical species as proposed by *Rojas-Andrade et al*. Therefore, the prevailing photoactivity observed for GOQD/MnO_2-c may not be only driven by hole production from MnO_2.

While MnO_2 is highlighted as an active site, the photoactivity of GOQD from the GOQD/MnO_2-c is unclear specially since the hydroxide concentration from the nanocomposite structure is lower in contrast to HNO_3 GOQD. To understand the photodynamic enhancement of GOQD/MnO2 more closely-c, the sample was treated photocatalytic with tert-butyl alcohol (TBA). The TBA polymerizes with other TBA molecules via a carbanion polymerization driven by $^{-}$OH oxidation process[81, 82]. The treatment of GOQD and E. coli with TBA produce no change in the photodynamic activity since TCD of E. coli + TBA ~ 840 sec, which is similar to the photodynamic activity of E.coli irradiated at 365 nm (TCD ~ 840 sec). Furthermore, the GOQD+TBA photoexcited sample yield no change in the viability of E. coli over photoexcitation period, like its photodynamic activity in the absence of TBA. In contrast to the GOQD and E. coli with TBA controls the photodynamic activity is drastically different for GOQD/MnO_2-c treated with TBA in comparison to the photodynamic activity of GOQD/MnO_2-c alone (Figure 9b). The effect of TBA upon the photodynamic activity GOQD/MnO_2-c is more poignant in contrast with EDTA (TCD_{EDTA} = 360 sec, TCD_{TBA} > 840 sec) (Figure 9c). Therein highlighting the importance of $^{-}$OH

production from GOQD/MnO_2-c nanocomposite due to the intricate junction between MnO_2 and GOQD. Therefore, production of -·OH is the prevalent driving species for photoactivity of GOQD/MnO_2-c.

To understand the catalytic role of GOQD/MnO_2 junction, EPR spectra was employed to identify the radical species formed under various experimental conditions. In Figure 7a the sextet peaks, labeled by an asterisk (*), are attributed to a hydrogen radical species with a_N = 22.9 G and a_H = 15.6 G [83]. In contrast to H_2O control, the GOQD and GOQD/MnO_2-c produce a higher concentration of hydrogen radical. Upon excitation at 365 nm (Figure 10b) both the GOQD and GOQD/MnO_2-c produce a quartet peak alongside a more intense sextet peak attributed to the hydrogen radical. The quartet peaks produced from GOQD and GOQD/MnO_2-c upon 365 nm excitation are attributed to a hydroxide radical with $a_N = a_H$ = 15 G (@) [84, 85]. Due to the quenching activity of TBA the radical scavenger was utilized with GOQD/MnO_2-c, GOQD, and H_2O to determine the radical species quenched by it. For the H_2O with TBA control, the hydroxyl radical species measured upon 365 nm excitation is quenched by TBA (Figure 10c). Alternatively, the hydrogen radical species is enhanced upon 365 nm excitation

and in the presence of TBA. The increase in hydrogen radical can be attributed to the slow rate of reaction of TBA with hydrogen radical (k_H =1.7 x 10^5 M^{-1} s^{-1}) in contrast to hydroxide radical (k_{OH} = 6.6 x 10^8 M^{-1} s^{-1}). The low bonding energy of tert-butyl carbon to hydrogen bonds (400.4 kJ/mol) lead to hydrogen radical production upon photolysis from tert-butyl alcohol[86]. The GOQD sample demonstrates hydrogen radical quenching in the presence of TBA while the hydroxyl radical species is enhanced (Figure 10d). Like GOQD, the GOQD/MnO_2-c sample has its hydrogen radical species quenched and its hydroxyl radical species enhanced in the presence of TBA (Figure 7e). Since the H_2O upon 365 nm exc with TBA control enhances its hydrogen radical signal, the quenching of the hydrogen radical formation at 365 nm for GOQD and GOQD/MnO_2-c can be attributed to the facile kinetics of hydrogen radical quenching in the presence of TBA.

To quantify the radical species formed from H_2O, GOQD, and GOQD/MnO_2 a peak-to-peak intensity measurement were measured from a specific peak attributed to each radical species (Figure 11). Under steady state conditions GOQD/MnO_2-c, GOQD, and H_2O produce varying intensities of radical species with GOQD/MnO_2-c

producing the highest concentration of radical species (Figure 11a). Hydrogen radicals constitute 94% of radical production from all samples under steady state conditions. Similarly upon excitation at 365 nm GOQD/MnO_2-c maintains the highest concentration of radical species although the hydrogen radical production from all samples decreases to 90% of all radical production (Figure 11b). Also the total concentration of radical production increases for all samples upon 365 nm excitation. Under steady state conditions with TBA the radical production of GOQD is quenched, decreasing from 0.12557 to 0.04523 intensity (Figure 11 c). The radical species concentration for H_2O and GOQD/MnO_2-c was consistent in the presence of TBA as in the absence of TBA under steady state conditions. The concentrations and percentage of radical species is variant between each sample under 365 nm excitation while in the presence of TBA (Figure 11d). The H_2O and TBA excited under 365 nm excitation produces a more enhanced radical intensity for both hydrogen and hydroxide radical with an overall radical signal peak-to-peak intensity of 0.21561 in contrast to its radical signal peak-to-peak intensity in the absence of TBA of 0.05973. In contrast to H_2O and TBA sample, the GOQD/MnO_2-c and GOQD with TBA under 365 nm exc. have

its overall radical intensities decrease. Furthermore, the GOQD/MnO_2-c and GOQD hydrogen radical signals decrease in the presence of TBA from 89.63% and 89.36% to 84.36% and 61.42% respectively. Since TBA produces hydrogen radicals under 365 nm excitation and in the absence of either GOQD and GOQD/MnO_2-c its ability to quench hydrogen radicals from such samples is due to its facile hydrogen radical quenching kinetics (k_H =1.7 x 10^5 M^{-1} s^{-1}). The enhanced hydroxyl radical signals produced under 365 nm excitation in the presence of TBA can be attributed to a decrease in hydrogen radical production (Figure 8d). The rate of water formation from hydroxyl and hydrogen radical reconstitution is faster (k = 1.53 x 10^{10} M^{-1} s^{-1}) than TBA's hydrogen radical quenching[87]. Therefore in the absence of TBA the low concentration of hydroxide radical produced from GOQD and GOQD/MnO_2-c is unobserved due to its production of water from its reaction with hydrogen radical (Figure 11b). Although during the excitation of both GOQD and GOQD/MnO_2-c in the presence of TBA leads to a substantial loss of hydrogen radical formation which prevents water formation via radical recombination (Figure 11d).

Although $^{\cdot}OH$ species may be the leading cause for photodynamic activity the enhancement of GOQD/MnO_2-c is enhanced in contrast to GOQD and MnO_2 independently. The source of the activity can be elucidated from the band structure of the GOQD/MnO_2-c.The band-gap for MnO_2 is defined by the energy difference between the t_{2g} and e_{2g} which differs for various valence states of Mn[88, 89]. Theoretically, a Mn^{4+} structure should maintain a band-gap energy of 2.5 eV. Inspection of the direct band gap measured from UV-VIS assigns a 2.7 eV to MnO_2 which agrees closely with theory. Furthermore band gap energy for α-MnO_2 nanowires is consistent for similar MnO_2 nanostructures synthesized which maintain a band gap ~2.2 eV to 2.5 eV [90, 91]. In a study by *Pinaud et al.* the conduction band potential (E_{cb}) was measured between 2.7 eV – 3.2 eV measured via various electrochemical methods[90]. The position of the conduction band is supported by the low efficiency of the incident photon-to-current efficiency (IPCE), which estimates a conduction band with a higher potential than H^+/H_2 which occurs at 0eV. Therefore the valence band positions for the MnO_2 from the GOQD/MnO_2-c can be estimated to be 2.7 V – 3.2 V while the conduction band, estimated from the band-

gap measured from the Tauc's plot (Figure S1), is positioned 0V – 0.5V.

The photoactivity of GOQD for hydroxyl radical production is driven by $\pi \rightarrow \pi^*$ which occurs near the excitation wavelength utilized for the photoactivity conducted in this work (i.e. 365 nm or 3.29 eV). The band-gap energy calculated for GOQD is supported by the theoretical calculation and experimental measurements of energy generated by sp^2 domains from graphene oxide structures[92, 93]. The conduction band which is determined from a band gap difference of the calculated valence band is measured at -0.79 V and 4.0 V for its respective valence band [94]. The proposed electronic structure of GO in *Hsu et al.* allows for the reduction of CO_2 into methanol via the hydrolysis of water redox positions. Since the photoreduction of CO_2 from *Hsu et al.* is driven by photoexcitation of sp^2 domains and the extent of oxidation enhances the photoreduction of CO_2 to methanol, then we can attribute the conduction band of this work's GOQD from GOQD/MnO_2-c to be positioned at -0.79 V. Then the valence band position for GOQD is calculated to be positioned at 2.5 V specifically for sp^2 domains contributing to the photocatalytic activity against *E.coli*.

In summary the band structure of MnO_2 would be 2.7-3.2 V for its valence band and 0-0.5 V for its conduction band while the band structure of GOQD is positioned at 2.5 V for its valence band and -0.79 V for its conduction band. The photodynamic studies comparing radical species scavengers demonstrate the extent of quenching of tert-butyl alcohol which is specific for hydrogen and hydroxyl formation. The redox potential of $H^{\cdot -}$ formation from H^+ occurs at 0 V which near or lower in potential than the valence band from MnO_2 and GOQD[95]. While the redox potential of $HO^{\cdot -}$ from H_2O occurs at 2.23 V which is lower in potential than the valence band of GOQD and MnO_2. Since the GOQD/MnO_2-c nanocomposite is excited at 365 nm (i.e. 3.29 eV), the energy of excitation is enough to induce an electron-hole separation within the MnO_2 and GOQD from the GOQD/MnO_2-c sample. Such electron-hole separation would induce holes within both MnO_2 and GOQD which would need to be replenished when photoexcited electrons are consumed by hydrogen radical. The efficiency for the photodynamic activity of GOQD/MnO_2-c indicate the photoexcited electrons react with a water-soluble species. Therefore, both GOQD and MnO_2 are replenished by photolysis of H_2O into $HO^{\cdot -}$ which would explain the extent of

quenching observed for EDTA which scavenges for holes on the valence band of the nanocomposite (Figure 9b). The TCD is higher for EDTA treated GOQD/MnO_2-c ($TCD_{EDTA\ GOQD/MnO2-c}$ = 360 seconds) in contrast to GOQD/MnO_2-c (TCD GOQD/MnO2/c < 180 seconds) the latter maintains a higher TCD in contrast to TBA treated GOQD/MnO_2-c (Figure 9b). Therefore $^{-}\cdot OH$ formation is not solely driven via hydrolysis of water into $^{-}\cdot OH$ but also from a photoreduction process.

Inspection of the conduction band structure of GOQD/MnO_2-c sets a band position at 0-0.5 V for MnO_2 and -0.79 V for GOQD. The hydrogen radical species measured via EPR document a high concentration of such a species for GOQD/MnO_2-c under 365 nm exc. The valence band structure of GOQD/MnO_2-c allows for electron movement from GOQD to MnO_2 via their respective conduction band which can react with H^+ to produce a high concentration . The bactericidal role of H^{-} is attributed to its degradation of methylene blue dye in the presence of EDTA were GOQD/MnO_2-c maintains its enhanced photodegradation of methylene blue dye in contrast to samples with low hydrogen radical production. Furthermore the decrease of hydrogen radical concentration quenched in the presence of TBA depletes the photoactivity of GOQD/MnO_2-c against

E.coli. The conduction band position of GOQD would enable the electron transfer from GOQD to the conduction band of MnO_2, therein inducing a higher population density of excited electrons utilized to produce $H^{\cdot -}$ from H^+. The GOQD/MnO_2-c produces an advantageous frame for photocatalytic bactericidal activity due to the facile synthetic strategy required to produce a water-soluble nanocomposite structure with enhanced photoactivity derived from its composite structure.

2.5 Conclusion

The band structure of GOQD/MnO_2-c provides for an ideal candidate for photocatalytic activity against *E. coli*. The formation of $H^{\cdot -}$ from GOQD/MnO_2-c provides evidence of the role of MnO_2 as the active site for photocatalysis via electron-hole separation. The appropriate feed ratio of $KMnO_4$ to GOQD produce a manganese oxide with a prevailing 4+ oxidation state for manganese which is related to the MnO_2 structure supported by TEM. The high percentage of MnO_2 deposited on GOQD leads to a dispersion of various active sites with a ~2.7 eV band gap ideal for electron-hole separation at an excitation wavelength of 365 nm (i.e. 3.29 eV). Simultaneously GOQD participates in this system by providing a substrate for MnO_2

nucleation and by contributing photoexcited electrons as evidenced by TRFL data. The excitation wavelength (3.29 eV) induces electron-hole separation in both GOQD and MnO_2 for the GOQD/MnO_2c structure. The electronic band structure for GOQD/MnO_2-c allows for ROS generation in both photoreduction and photooxidation pathways which is prevalent amongst many of the GOQD/MnO_2 samples in contrast to photocatalytic experiments conducted independently on GOQD and MnO_2. Although clearly the valence state of Mn, oxidation state of GOQD, and dispersion of MnO_2 is ideal for GOQD/MnO_2-c which ultimately determines the source of its enhanced photocatalytic activity.

2.6 Supporting Information

Table S1. Band gap energy (eV) of GOQD and MnO_2/GOQD with their respective HNO_3 treated samples

Sample	%Mn/ C	$\tau_{avg.}$ (ns)	Bandgap Energy (eV)	Bandgap Energy (nm)
GOQD	0	1.724	3.2 – 3.8	316 - 375
GOQD/ MnO_2-a	11.26	1.316	3.2 – 4.2	285 - 375
GOQD/ MnO_2-b	8.42	1.675	3.25 – 4.25	282 - 369
GOQD/ MnO_2-c	7.85	2.564	2.75 – 4.8	250 -387
GOQD/ MnO_2-d	0.9369	-	3.5 – 4.75	252 - 342
GOQD/ MnO_2-e	1.846	-	3.2 – 4.8	250 - 375
HNO_3 GOQD/ MnO_2-c	0.92	2.74	2.7 – 3.5	342 - 444
HNO_3 GOQD	0	1.66	2.8 – 3.8	315 - 428

Table S2. Average %CFU and standard deviation of *E. coli*, GOQD, and MnO_2/GOQD-x under photoirradiation at 365 nm for varied periods of time.

Sample	**t = 0**	**180 s**	**360 s**	**720 s**
E. coli	100	77.86 ± 6.42	32.76 ± 8.67	1.26 ± 0.90
GOQD	100	100.64 ± 23.27	88.06 ± 22.11	85.25 ± 19.37
GOQD/ MnO_2-a	100	11.96 ± 8.28	5.27 ± 5.83	2.47 ± 3.24
GOQD/ MnO_2-b	100	10.68 ± 5.67	3.53 ± 4.09	0.37 ± 0.52
GOQD/ MnO_2-c	100	2.42 ± 3.43	0	0
GOQD/ MnO_2-d	100	-	98.02 ± 0.75	86.37 ± 2.43
GOQD/ MnO_2-e	100	-	58.23 ± 34.53	6.58 ± 8.15

Table S3. C1s peak positions and Intensity for GOQD and MnO_2/GOQD Samples

Sample	C1s (C=C)	C1s (C-O)	C1s (C-O-C)	C1s (C=O)	C1s (HO-C=O)
GOQD	284.4 ± 0.03	285.8 ± 0.11	-	287.66 ± 0.14	-
GOQD/ MnO_2-a	284.47 ± 0.06	-	286.26 ± 0.05	288.04 ± 0.09	-
GOQD/ MnO_2-b	284.705 ± 0.025	-	286.31 ± 0.05	288.14 ± 0.01	-
GOQD/ MnO_2-c	284.72 ± 0.01	-	286.32 ± 0.06	288.16 ± 0.01	-
GOQD/ MnO_2-d	284.5 ± 0.09	285.96 ± 0.16	-	288.02 ± 0.07	-
GOQD/ MnO_2-e	284.72 ± 0.12	286.115 ± 0.115	-	--	288.36 ± 0.115
HNO_3 GOQD	284.75 ± 0.04	285.62 ± 0.10	-	-	288.91 ± 0.08
HNO_3 GOQD/ MnO_2-c	284.99 ± 0.19	285.15 ± 0.04	-	-	288.63 ± 0.04

Table S4. Percent compositions of varied carbon species in the MnO_2/GOQD Series

Sample	sp^2 C (%)	C-OH (%)	C-O-C (%)	C=O (%)	HO-C=O (%)
GOQD	78.37	12.37	0	10.30	0
GOQD/MnO_2-a	71.98	0	12.95	15.07	0
GOQD/MnO_2-b	61.84	0	10.39	27.78	0
GOQD/MnO_2-c	66.46	0	14.93	18.61	0
GOQD/MnO_2-d	58.24	13.99	0	27.77	0
GOQD/MnO_2-e	66.27	17.57	0	0	18.49
HNO_3 GOQD	41.58	41.18	0	0	17.23
HNO_3 GOQD/MnO_2-c	45.48	42.55	0	0	11.97

Table S5. Mn2p Peak Positions for GOQD and MnO_2/GOQD Samples with Average and Standard

Sample	Mn2p $2p^{3/2}$ (pos.1)	Mn2p $2p^{1/2}$ (pos.1)	ΔB.E.	Mn2p $2p^{3/2}$ (pos. 2)	Mn2p $2p^{1/2}$ (pos.2)	ΔB.E.
GOQD	-	-	-	-	-	-
MnO_2/GOQD-a	641.99 ± 0.1	653.65 ± 0.06	11.66	644.46 ± 0.23	656.20 ± 0.20	11.74
MnO_2/GOQD-b	642.15 ± 0.005	653.86 ± 0.001	11.7	-	-	-
MnO_2/GOQD-c	641.70 ± 0.205	653.4 ± 0.205	11.70	642.61 ± 0.07	654.31 ± 0.07	11.7
MnO_2/GOQD-d	640.53 ± 0.059	652.62 ± 0.158	12.1	641.86 ± 0.07	653.93 ± 0.24	12.1
MnO_2/GOQD-e	642.38 ± 0.025	654.22 ± 0.035	11.84	-	-	-

Table S6. Mn2p Intensity for MnO_2/GOQD-x with Standard Deviation

Sample	%Mn/C (total C)	%Mn^{4+}/Mn (total Mn)	%Mn^{4+}/Mn (total Mn)	Mn^{6+}/Mn (total Mn)	Mn^{2+}/Mn (total Mn)
MnO_2/GOQD-a	11.26	82.69	0	17.30	0
MnO_2/GOQD-b	8.42	83.95	0	16.05	0
MnO_2/GOQD-c	7.85	100	0	0	0
MnO_2/GOQD-d	0.936	69.11	0	0	30.89
MnO_2/GOQD-e	1.85	100	0	0	0

Table S7. Binding energy of varied oxygen species in the MnO_2/GOQD series

Sample	O1s (lattice O MnO_x)	O1s (C=O)	O1s (C-O) (aliphatic)	O1s (C-O) (aromatic)	O1s (adsorbed H_2O)
GOQD	-	531.35 ± 0.01	532.22 ± 0.17	-	535.66 ± 0.06
GOQD/MnO_2-a	529.61 ± 0.13	531.24 ± 0.06	532.63 ± 0.03	-	-
GOQD/MnO_2-b	529.54 ± 0.07	531.08 ± 0.04	532.38 ± 0.04	533.24 ± 0.03	-
GOQD/MnO_2-c	529.74 ± 0.02	531.13 ± 0.03	532.46 ± 0.19	-	535.19 ± 0.16
GOQD/MnO_2-d	530.53 ± 0.05	531.22 ± 0.07	532.34 ± 0.10	-	534.7 ± 0.01
GOQD/MnO_2-e	530 ± 0.01	530.98 ± 0.03	532.10 ± 0.005	533.15 ± 0.001	536.15

Table S8. Percent compositions of varied oxygen species in the MnO_2/GOQD series

Sample	Csp^2 = O (%)	aliphatic-O Oxygen (%)	Csp^2-O Oxygen (%)	H_2O (%)	Lattice Oxygen on MnO_2 (%)
GOQD	54.11	39.04	0	6.85	0
GOQD/ MnO_2-a	46.90	31.36	0	0	21.74
GOQD/ MnO_2-b	43.20	25.94	16.80	0	14.05
GOQD/ MnO_2-c	36.07	40.50	0	4.48	18.95
GOQD/ MnO_2-d	35.11	48.15	0	2.54	21.87
GOQD/ MnO_2-e	7.87	36.59	39.10	13.16	3.28

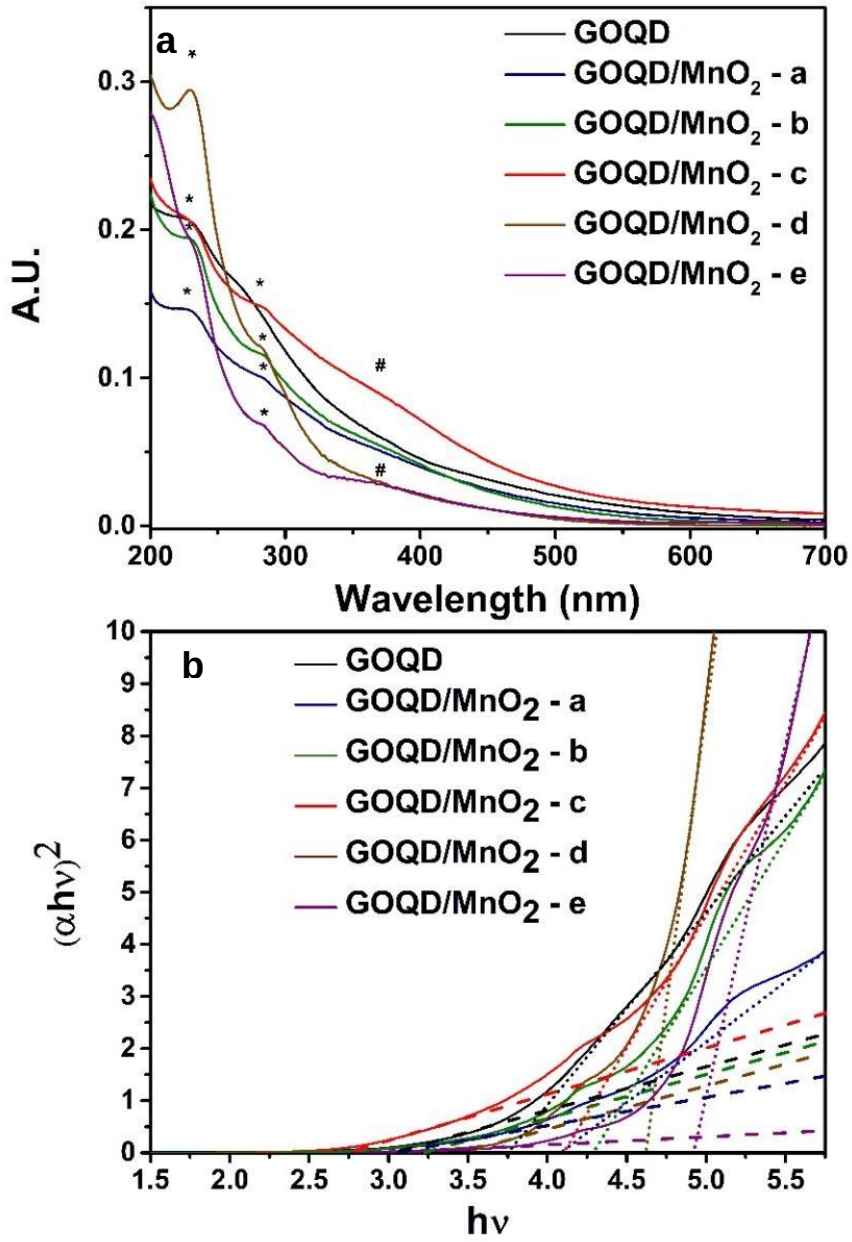

Figure S1. a) UV-VIS absorption spectrum of GOQD, GOQD/MnO_2-a, GOQD/MnO_2-b , GOQD/MnO_2-c , GOQD/MnO_2-d, and GOQD/MnO_2-e b) Direct-Band Gap measurement of GOQD, GOQD/MnO_2-a, GOQD/MnO_2-b , GOQD/MnO_2-c , GOQD/MnO_2-d, and GOQD/MnO_2-e

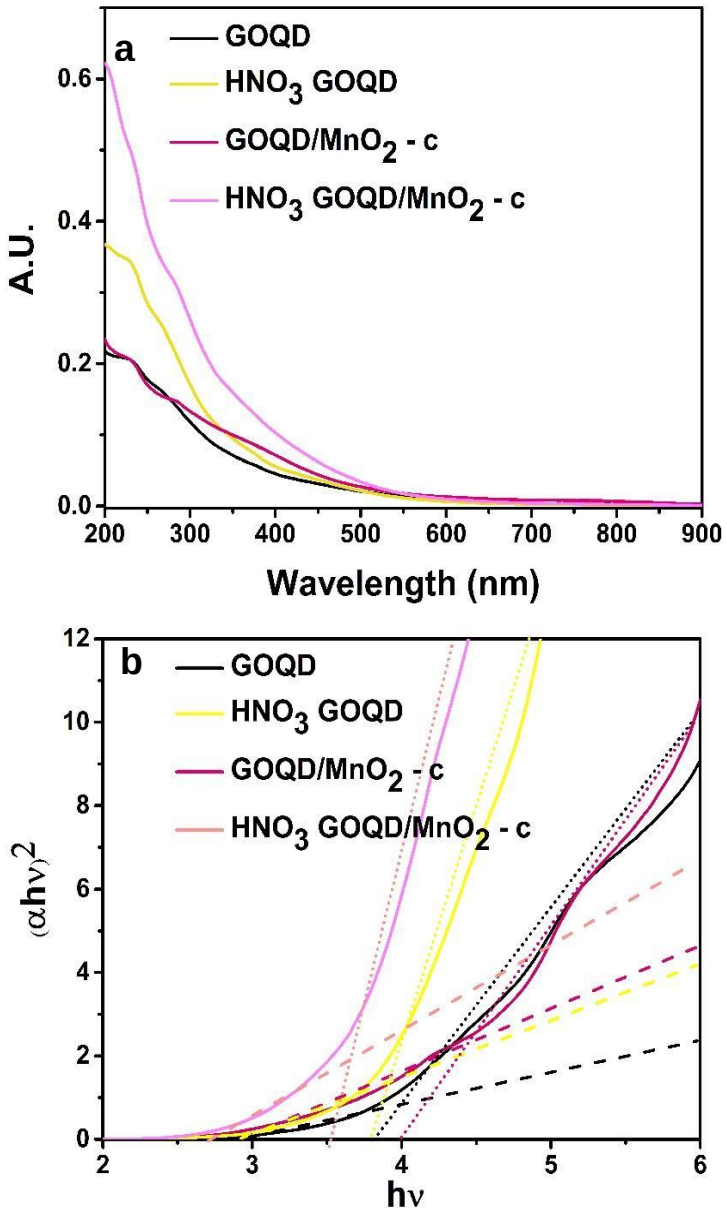

Figure S2. a) UV-VIS spectra of GOQD, HNO_3 GOQD, HNO_3 MnO_2/GOQD-c, and MnO_2 b) Direct Band Gap Measurement of GOQD, HNO_3 GOQD, MnO_2/GOQD-c, and HNO3 MnO_2/GOQD-c

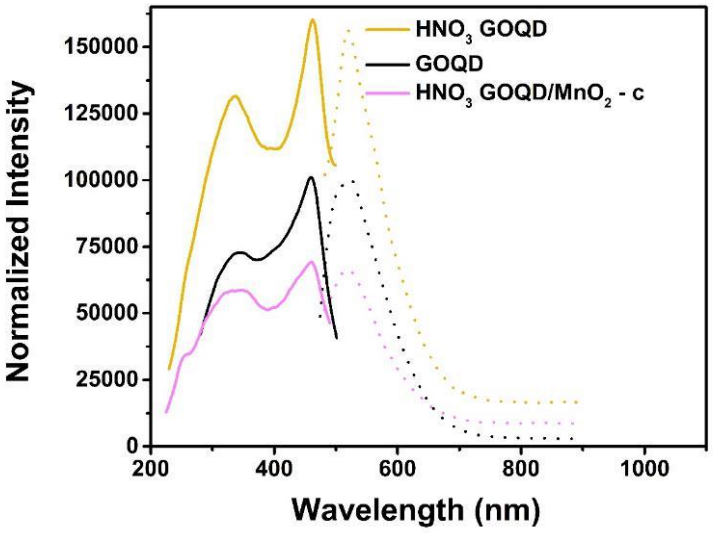

Figure S3. Photoluminescence spectra of GOQD, HNO_3 GOQD, and HNO_3 MnO_2/GOQD-IV at 465 nm excitation

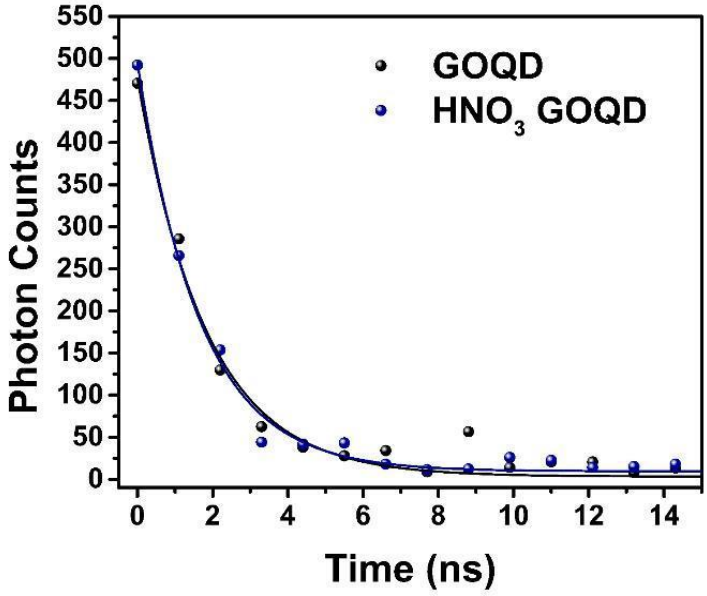

Figure S4. Fluorescence Lifetime Decay Measurements for GOQD and HNO_3

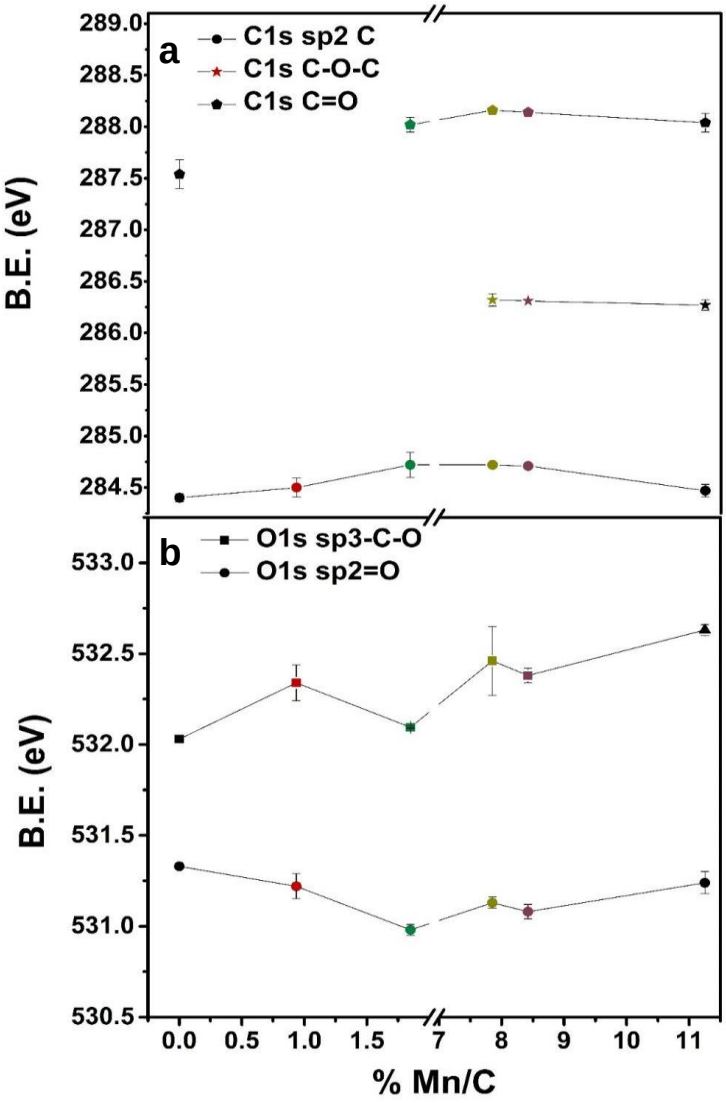

Figure S5. a) Binding energy positions from C1s spectra for GOQD/MnO_2-x samples and GOQD b) Binding energy positions from O1s spectra for MnO_2/GOQD-x samples and GOQD

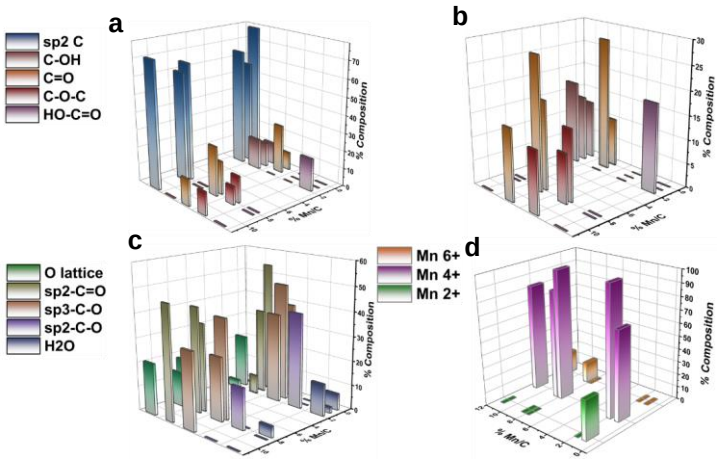

Figure S6. a,b) Percent composition of C1s spectra from sp^2 C, C=O, C-OH, C-O-C, and O=C-OH as a function of % Mn/C for MnO_2/GOQD-x series c) Percent composition of O1s spectra from O lattice, sp^2-C=O, sp^3-C-O, sp^2-C-O, and adsorbed H_2O as a function of % Mn/C a from MnO_2/GOQD-x series d) Percent composition of Mn^{4+} and Mn^{6+} as a function of %Mn/C from MnO_2/GOQD-x series

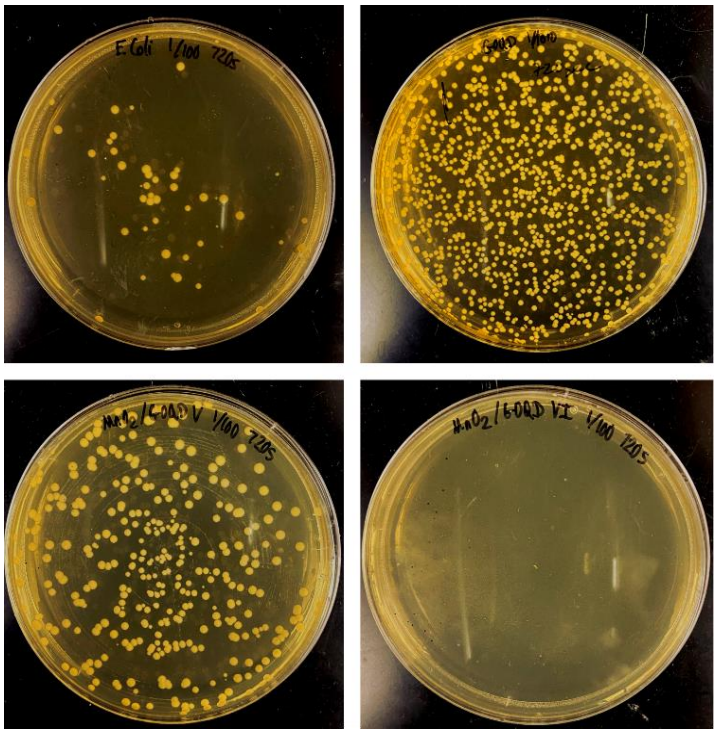

Figures S7: Colony Forming Units (CFU) of *E.coli* with GOQD, GOQD/MnO_2-d, GOQD/MnO_2-e, and in the absence of photocatalyst excited at 365 nm for 720 seconds

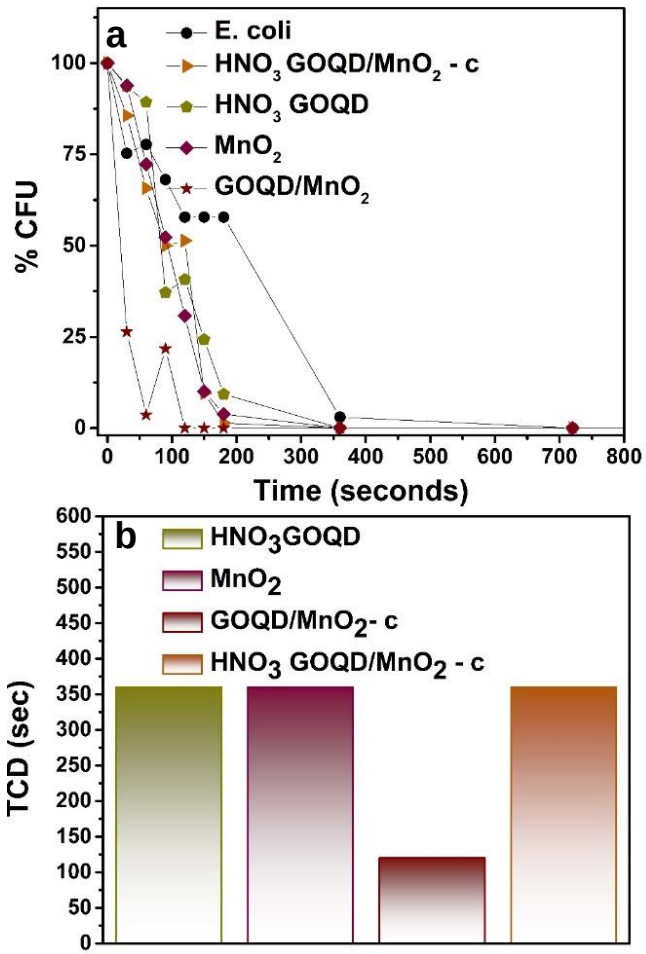

Figures S8: a) Photodynamic activity of *E.coli* with HNO_3 GOQD/MnO_2-c, HNO_3 GOQD, MnO_2, GOQD/MnO_2-c, and without photocatalyst b) TCD of *E.coli* with HNO_3 GOQD/MnO_2-c, HNO_3 GOQD, MnO_2, GOQD/MnO_2-c, and without photocatalyst

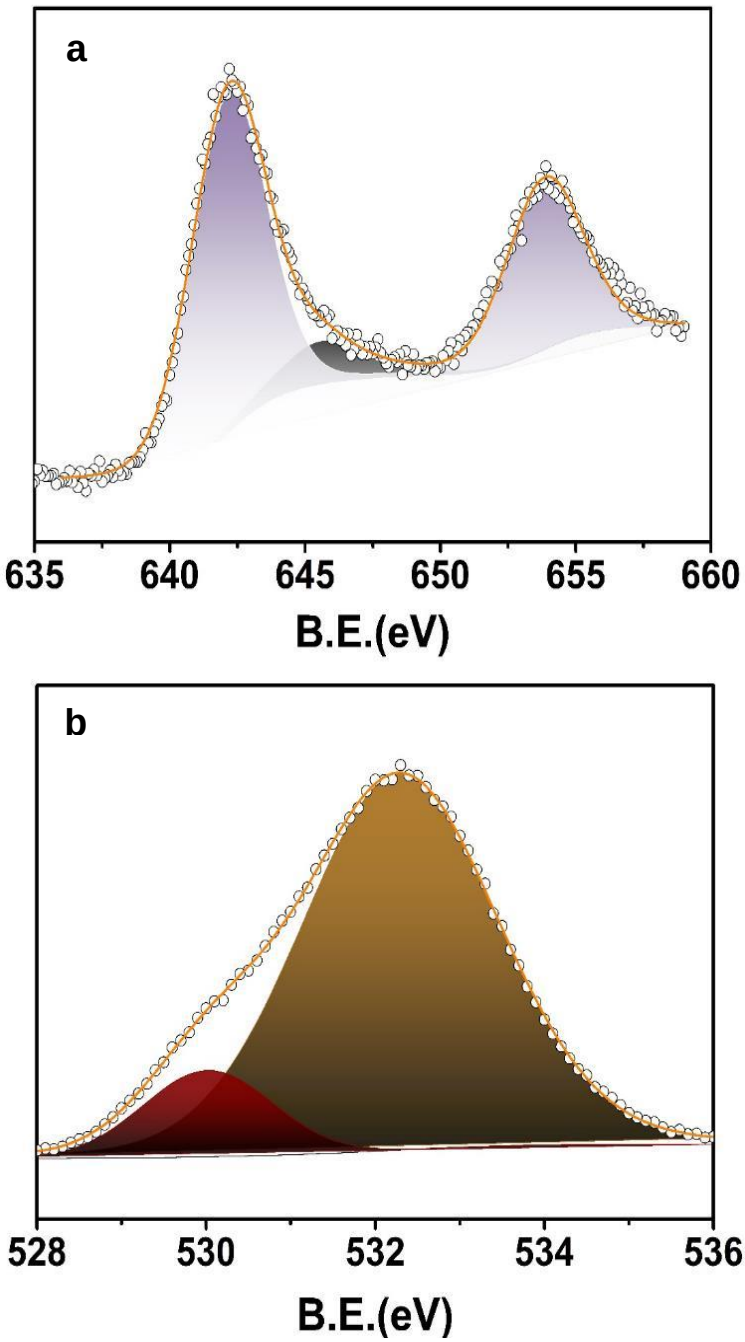

Figures S9: A) XPS Mn2p spectra for δ-MnO_2 B) XPS O1s spectra for δ-MnO

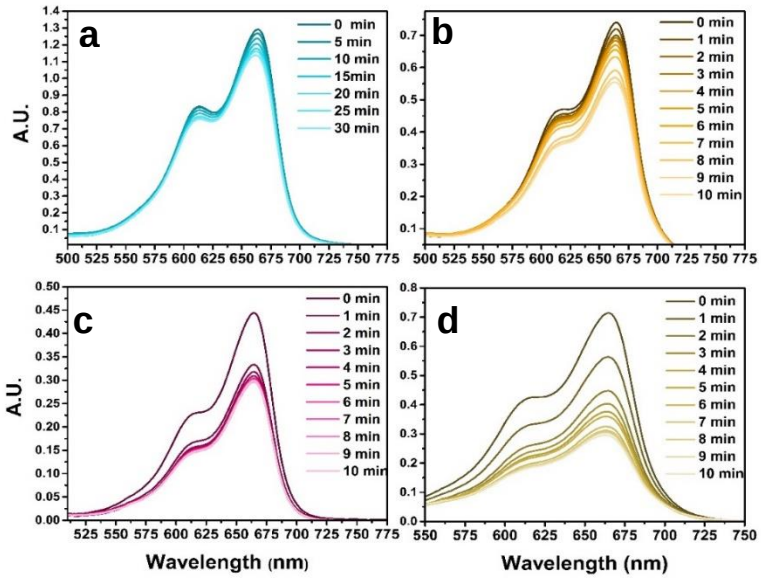

Figures S10: UV-VIS spectra for Methylene Blue and respective photocatalysts at an excitation wavelength of 365 nm for A) Methyelene Blue Dye B) GOQD, Methylene Blue Dye C) δ-MnO_2, Methylene Blue Dye D) GOQD/MnO_2-c , Methylene Blue Dye

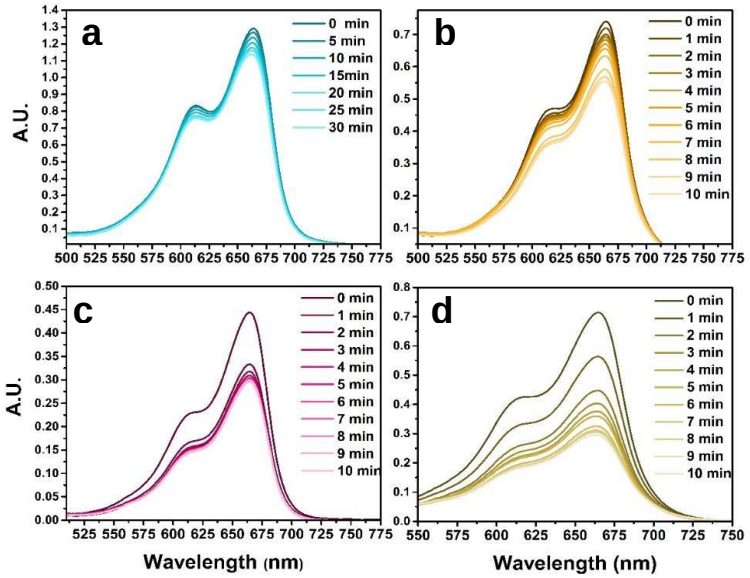

Figures S11: UV-VIS spectra for Methylene Blue and respective photocatalysts at an excitation wavelength of 365 nm for A) Methyelene Blue Dye and EDTA B) GOQD, Methylene Blue Dye, and EDTA C) δ-MnO_2, Methylene Blue Dye, and EDTA D) GOQD/MnO_2-c , Methylene Blue Dye, and EDTA

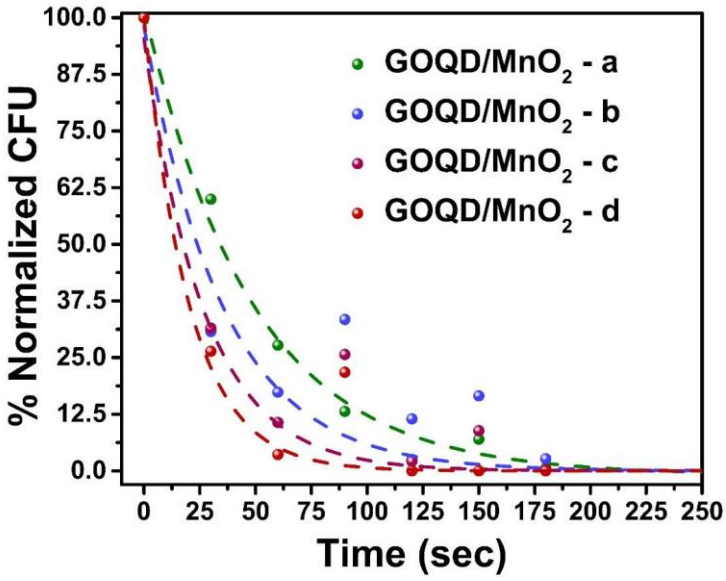

Figures S12: First order exponential decay fit for GOQD/MnO_2 -a, b, c, and d series for %CFU decayed over time for an excitation wavelength of 365 nm

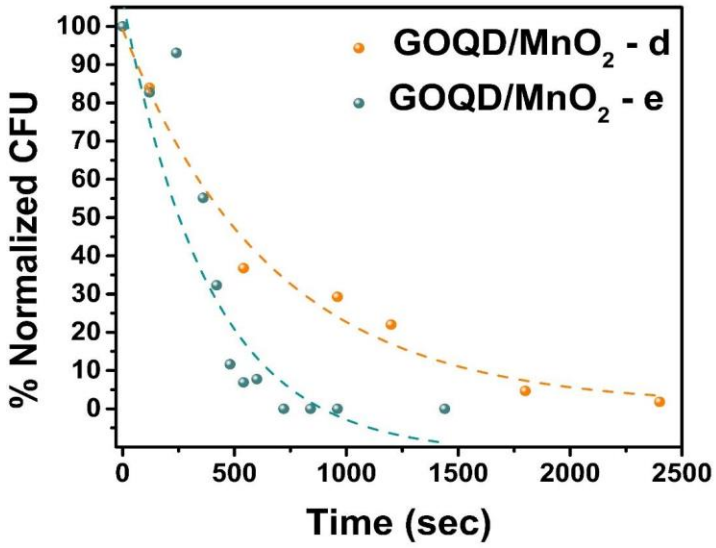

Figures S13: First order exponential decay fit for GOQD/MnO_2 -d and e series for %CFU decayed over time for an excitation wavelength of 365 nm

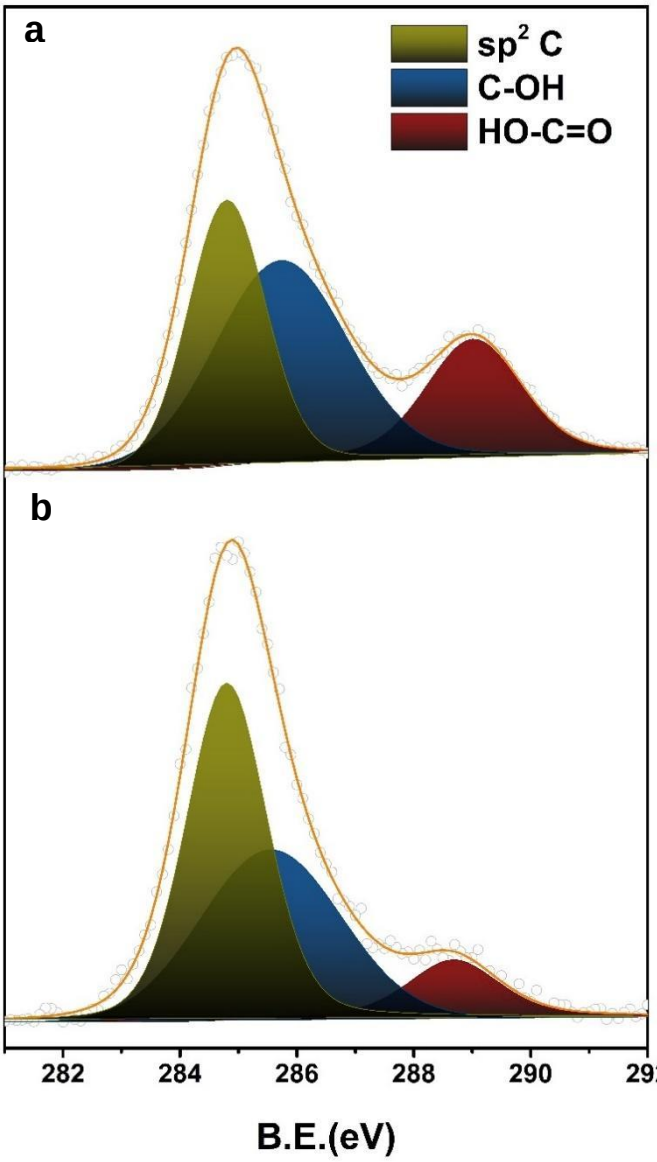

Figure S14: XPS Spectra of C1s for a) HNO_3 treated GOQD and b) GOQD/MnO_2-c

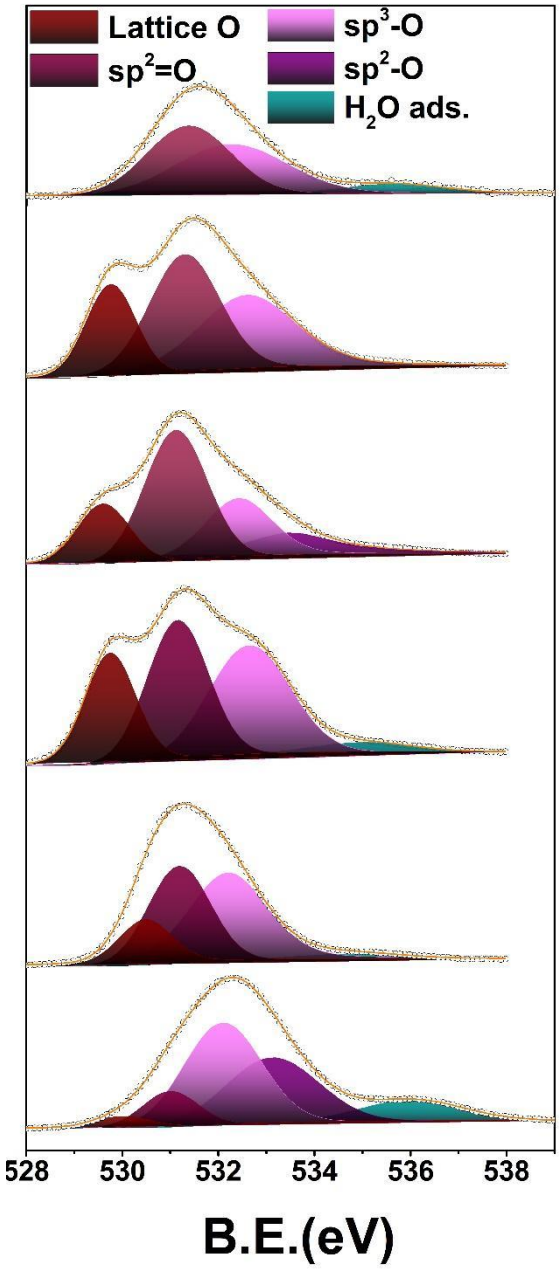

Figure S15: XPS O1s Spectra for a) GOQD, b) GOQD/MnO_2-a, c) GOQD/MnO_2-b, d) GOQD/MnO_2-c, e) GOQD/MnO_2-d, GOQD/MnO_2-e

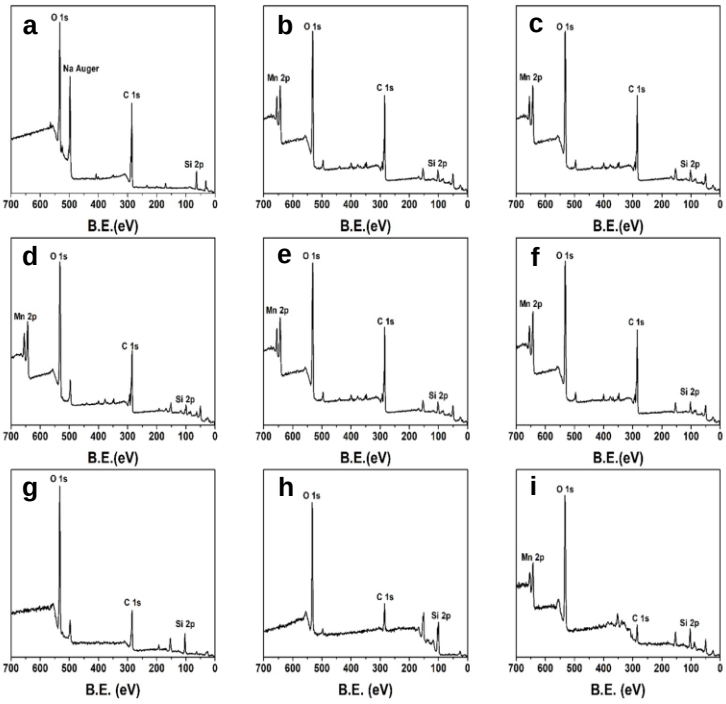

Figure S16: XPS Survey Scan of a) GOQD, b) GOQD/MnO_2-a, c) GOQD/MnO_2-b, d) GOQD/MnO_2-c, e) GOQD/MnO_2-d, f) GOQD/MnO_2-e, g) HNO_3 GOQD, h) HNO_3 GOQD/MnO_2-c, and i) MnO_2

Acknowledgments This work was supported in part by the National Science Foundation (CHE-1710408 and CBET-1848841). TEM and XPS work were carried out at the National Center for Electron Microscopy and Molecular Foundry of the Lawrence Berkeley National Laboratory as part of a user project.

2.6 References

1. Livermore, D.M., *Mechanisms of resistance to beta-lactam antibiotics.* Scand J Infect Dis Suppl, 1991. **78**: p. 7-16.
2. Wilke, M.S., A.L. Lovering, and N.C.J. Strynadka, *beta-lactam antibiotic resistance: a current structural perspective.* Current Opinion in Microbiology, 2005. **8**(5): p. 525-533.
3. Kotra, L.P. and S. Mobashery, *beta-Lactam antibiotics, beta-lactamases and bacterial resistance.* Bulletin De L Institut Pasteur, 1998. **96**(3): p. 139-150.
4. Ashraf, Z., et al., *Novel Penicillin Analogues as Potential Antimicrobial Agents; Design, Synthesis and Docking Studies.* PLoS One, 2015. **10**(8): p. e0135293.
5. Puzyn, T., et al., *Using nano-QSAR to predict the cytotoxicity of metal oxide nanoparticles.* Nature Nanotechnology, 2011. **6**(3): p. 175-178.
6. Jones, N., et al., *Antibacterial activity of ZnO nanoparticle suspensions on a broad spectrum of microorganisms.* Fems Microbiology Letters, 2008. **279**(1): p. 71-76.
7. Azam, A., et al., *Antimicrobial activity of metal oxide nanoparticles against Gram-positive and Gram-negative*

bacteria: a comparative study. Int J Nanomedicine, 2012. **7**: p. 6003-9.

8. Li, Y., et al., *Mechanism of Photogenerated Reactive Oxygen Species and Correlation with the Antibacterial Properties of Engineered Metal-Oxide Nanoparticles.* Acs Nano, 2012. **6**(6): p. 5164-5173.
9. Prasanna, V.L. and R. Vijayaraghavan, *Insight into the Mechanism of Antibacterial Activity of ZnO: Surface Defects Mediated Reactive Oxygen Species Even in the Dark.* Langmuir, 2015. **31**(33): p. 9155-9162.
10. Applerot, G., et al., *Enhanced Antibacterial Activity of Nanocrystalline ZnO Due to Increased ROS-Mediated Cell Injury.* Advanced Functional Materials, 2009. **19**(6): p. 842-852.
11. Meghana, S., et al., *Understanding the pathway of antibacterial activity of copper oxide nanoparticles.* Rsc Advances, 2015. **5**(16): p. 12293-12299.
12. Krishnamoorthy, K., et al., *Antibacterial activity of MgO nanoparticles based on lipid peroxidation by oxygen vacancy.* Journal of Nanoparticle Research, 2012. **14**(9): p. 1063-1063.

13. Tran, N., et al., *Bactericidal effect of iron oxide nanoparticles on Staphylococcus aureus.* International Journal of Nanomedicine, 2010. **5**: p. 277-283.

14. Vijayalakshmi, K. and D. Sivaraj, *Enhanced antibacterial activity of Cr doped ZnO nanorods synthesized using microwave processing.* Rsc Advances, 2015. **5**(84): p. 68461-68469.

15. Levanon, M.J.a.H., *Charge Distribution between UV-Irradiated TiO2 and Gold Nanoparticles: Determination of Shift in the Fermi Level.* Nano Letters, 2003. **3**(3): p. 353-358.

16. He, W.W., et al., *Photogenerated Charge Carriers and Reactive Oxygen Species in ZnO/Au Hybrid Nanostructures with Enhanced Photocatalytic and Antibacterial Activity.* Journal of the American Chemical Society, 2014. **136**(2): p. 750-757.

17. Zhang, L.Z., et al., *Ambient light reduction strategy to synthesize silver nanoparticles and silver-coated TiO2 with enhanced photocatalytic and bactericidal activities.* Langmuir, 2003. **19**(24): p. 10372-10380.

18. Garza, K.M., K.F. Soto, and L.E. Murr, *Cytotoxicity and reactive oxygen species generation from aggregated carbon*

and carbonaceous nanoparticulate materials. Int J Nanomedicine, 2008. **3**(1): p. 83-94.

19. Akhavan, O., E. Ghaderi, and A. Esfandiar, *Wrapping bacteria by graphene nanosheets for isolation from environment, reactivation by sonication, and inactivation by near-infrared irradiation.* J Phys Chem B, 2011. **115**(19): p. 6279-88.

20. Krishnamoorthy, K., et al., *Antibacterial Efficiency of Graphene Nanosheets against Pathogenic Bacteria via Lipid Peroxidation.* Journal of Physical Chemistry C, 2012. **116**(32): p. 17280-17287.

21. Liu, S.B., et al., *Antibacterial Activity of Graphite, Graphite Oxide, Graphene Oxide, and Reduced Graphene Oxide: Membrane and Oxidative Stress.* Acs Nano, 2011. **5**(9): p. 6971-6980.

22. Liu, S.B., et al., *Lateral Dimension-Dependent Antibacterial Activity of Graphene Oxide Sheets.* Langmuir, 2012. **28**(33): p. 12364-12372.

23. Akhavan, O. and E. Ghaderi, *Toxicity of Graphene and Graphene Oxide Nanowalls Against Bacteria.* Acs Nano, 2010. **4**(10): p. 5731-5736.

24. Perreault, F., et al., *Antimicrobial Properties of Graphene Oxide Nanosheets: Why Size Matters.* Acs Nano, 2015. **9**(7): p. 7226-7236.

25. Ristic, B.Z., et al., *Photodynamic antibacterial effect of graphene quantum dots.* Biomaterials, 2014. **35**(15): p. 4428-4435.

26. Akhavan, O. and E. Ghaderi, *Photocatalytic Reduction of Graphene Oxide Nanosheets on TiO2 Thin Film for Photoinactivation of Bacteria in Solar Light Irradiation.* Journal of Physical Chemistry C, 2009. **113**(47): p. 20214-20220.

27. Fan, W.Q., et al., *Nanocomposites of TiO2 and Reduced Graphene Oxide as Efficient Photocatalysts for Hydrogen Evolution.* Journal of Physical Chemistry C, 2011. **115**(21): p. 10694-10701.

28. Chowdhuri, A.R., et al., *A ZnO decorated chitosan-graphene oxide nanocomposite shows significantly enhanced antimicrobial activity with ROS generation.* Rsc Advances, 2015. **5**(61): p. 49420-49428.

29. Liu, J.L., et al., *Photo-enhanced antibacterial activity of ZnO/graphene quantum dot nanocomposites.* Nanoscale, 2018. **10**(1): p. 158-166.

30. Akhavan, O., *Photocatalytic reduction of graphene oxides hybridized by ZnO nanoparticles in ethanol.* Carbon, 2011. **49**(1): p. 11-18.

31. Williams, G. and P.V. Kamat, *Graphene-Semiconductor Nanocomposites: Excited-State Interactions between ZnO Nanoparticles and Graphene Oxide.* Langmuir, 2009. **25**(24): p. 13869-13873.

32. Jiang, G.D., et al., *TiO2 nanoparticles assembled on graphene oxide nanosheets with high photocatalytic activity for removal of pollutants.* Carbon, 2011. **49**(8): p. 2693-2701.

33. Wang, H., et al., *Recyclable enzyme mimic of cubic Fe3O4 nanoparticles loaded on graphene oxide-dispersed carbon nanotubes with enhanced peroxidase-like catalysis and electrocatalysis.* Journal of Materials Chemistry B, 2014. **2**(28): p. 4442-4448.

34. Yin, Z.Y., et al., *Electrochemical Deposition of ZnO Nanorods on Transparent Reduced Graphene Oxide Electrodes for Hybrid Solar Cells.* Small, 2010. **6**(2): p. 307-312.

35. Goncalves, P.R., H.A. De Abreu, and H.A. Duarte, *Stability, Structural, and Electronic Properties of Hausmannite (Mn3O4) Surfaces and Their Interaction with Water.* Journal of Physical Chemistry C, 2018. **122**(36): p. 20841-20849.

36. Gan, Z.X., et al., *Mn2+-Bonded Reduced Graphene Oxide with Strong Radiative Recombination in Broad Visible Range Caused by Resonant Energy Transfer.* Nano Letters, 2011. **11**(9): p. 3951-3956.

37. Anwar, Y., *Antibacterial and lead ions adsorption characteristics of chitosan-manganese dioxide bionanocomposite.* International Journal of Biological Macromolecules, 2018. **111**: p. 1140-1145.

38. Khan, S., et al., *In vitro evaluation of anticancer and biological activities of synthesized manganese oxide nanoparticles.* Medchemcomm, 2016. **7**(8): p. 1647-1653.

39. He, G.Q., et al., *Oxygen Reduction Catalyzed by Platinum Nanoparticles Supported on Graphene Quantum Dots.* Acs Catalysis, 2013. **3**(5): p. 831-838.

40. Song, Y. and S.W. Chen, *Graphene Quantum-Dot-Supported Platinum Nanoparticles: Defect-Mediated Electrocatalytic Activity in Oxygen Reduction.* Acs Applied Materials & Interfaces, 2014. **6**(16): p. 14050-14060.

41. Peng, Y., et al., *Point of Anchor: Impacts on Interfacial Charge Transfer of Metal Oxide Nanoparticles.* Journal of the American Chemical Society, 2018. **140**(45): p. 15290-15299.

42. Jampaiah, D., et al., *Nanowire Morphology of Mono- and Bidoped alpha-MnO2 Catalysts for Remarkable Enhancement in Soot Oxidation.* Acs Applied Materials & Interfaces, 2017. **9**(38): p. 32652-32666.

43. Wu, B., et al., *Graphene Scroll-Coated alpha-MnO2 Nanowires as High-Performance Cathode Materials for Aqueous Zn-Ion Battery.* Small, 2018. **14**(13): p. e1703850.

44. Vigil, J.A., et al., *Nanoscale Carbon Modified alpha-MnO2 Nanowires: Highly Active and Stable Oxygen Reduction Electrocatalysts with Low Carbon Content.* ACS Appl Mater Interfaces, 2018. **10**(2): p. 2040-2050.

45. Ma, Z.P., et al., *Construction of Hierarchical alpha-MnO2 Nanowires@Ultrathin delta-MnO2 Nanosheets Core-Shell Nanostructure with Excellent Cycling Stability for High-Power Asymmetric Supercapacitor Electrodes.* Acs Applied Materials & Interfaces, 2016. **8**(14): p. 9050-9058.

46. Zhang, H.N., et al., *Synthesis of KMnO4-treated magnetic graphene oxide nanocomposite (Fe3O4@GO/MnOx) and its application for removing of Cu2+ ions from aqueous solution.* Nanotechnology, 2018. **29**(13): p. 35706-35706.

47. Chen, S., et al., *Graphene Oxide-MnO2 Nanocomposites for Supercapacitors.* Acs Nano, 2010. **4**(5): p. 2822-2830.

48. Varela-Rizo, H., et al., *Graphene oxide nanoplatelets of different crystallinity synthesized from helical-ribbon carbon nanofibers and multiwall carbon nanotubes.* Journal of Materials Research, 2011. **26**(20): p. 2632-2641.

49. Peng, W.C., S.B. Wang, and X.Y. Li, *Shape-controlled synthesis of one-dimensional alpha-MnO2 nanocrystals for organic detection and pollutant degradation.* Separation and Purification Technology, 2016. **163**: p. 15-22.

50. Dimiev, A.E.S., *Graphene Oxide Fundamental Applications* 2017: Wiley. 16-17.

51. Sun, J.J., et al., *Fully Converting Graphite into Graphene Oxide Hydrogels by Preoxidation with Impure Manganese Dioxide.* Acs Applied Materials & Interfaces, 2015. **7**(38): p. 21356-21363.

52. Dimiev, A.M. and J.M. Tour, *Mechanism of Graphene Oxide Formation.* Acs Nano, 2014. **8**(3): p. 3060-3068.

53. Marcano, D.C., et al., *Improved Synthesis of Graphene Oxide.* Acs Nano, 2010. **4**(8): p. 4806-4814.

54. Chen, Q., et al., *Intelligent Albumin-MnO2 Nanoparticles as pH-/H2 O2 -Responsive Dissociable Nanocarriers to Modulate Tumor Hypoxia for Effective Combination Therapy.* Adv Mater, 2018. **30**(8).

55. Abulizi, A., et al., *Synthesis of MnO2 nanoparticles from sonochemical reduction of MnO4(-) in water under different pH conditions.* Ultrason Sonochem, 2014. **21**(5): p. 1629-34.

56. Kitchaev, D.A., et al., *Energetics of MnO2 polymophs in density functional theory.* Physical Review B, 2016. **93**(4).

57. Pinaud, B.A., et al., *Thin Films of Sodium Birnessite-Type MnO2: Optical Properties, Electronic Band Structure, and Solar Photoelectrochemistry.* Journal of Physical Chemistry C, 2011. **115**(23): p. 11830-11838.

58. Li, T.Q., et al., *Band gap engineering of MnO2 through in situ Al-doping for applicable pseudocapacitors.* Rsc Advances, 2016. **6**(17): p. 13914-13919.

59. Jeong, H.K., et al., *Tailoring the characteristics of graphite oxides by different oxidation times.* Journal of Physics D-Applied Physics, 2009. **42**(6): p. 65418-65418.

60. Eda, G., et al., *Blue Photoluminescence from Chemically Derived Graphene Oxide.* Advanced Materials, 2010. **22**(4): p. 505-+.

61. Kaftelen, H., et al., *Mn-substituted spinel Li4Ti5O12 materials studied by multifrequency EPR spectroscopy.* Journal of Materials Chemistry A, 2013. **1**(34): p. 9973-9982.

62. Li, M., et al., *Fingerprinting photoluminescence of functional groups in graphene oxide.* Journal of Materials Chemistry, 2012. **22**(44): p. 23374-23379.

63. Shafi, P.M., V.K. Jose, and A.C. Bose, *Graphene Oxide-MnO2 Nanocomposite for Supercapacitor Application.* Carbon Nanotubes, Graphene, and Emerging 2d Materials for Electronic and Photonic Devices Ix, 2016. **9932**.

64. Liu, J., et al., *Photo-enhanced antibacterial activity of ZnO/graphene quantum dot nanocomposites.* Nanoscale, 2017. **10**(1): p. 158-166.

65. Zerfass, C., J.A. Christie-Oleza, and O.S. Soyer, *Manganese Oxide Biomineralization Provides Protection against Nitrite Toxicity in a Cell-Density-Dependent Manner.* Appl Environ Microbiol, 2019. **85**(2).

66. Raghupathi, K.R., R.T. Koodali, and A.C. Manna, *Size-Dependent Bacterial Growth Inhibition and Mechanism of Antibacterial Activity of Zinc Oxide Nanoparticles.* Langmuir, 2011. **27**(7): p. 4020-4028.

67. Sawai, J., *Quantitative evaluation of antibacterial activities of metallic oxide powders (ZnO, MgO and CaO) by conductimetric assay.* Journal of Microbiological Methods, 2003. **54**(2): p. 177-182.

68. Wang, Y.W., et al., *Superior Antibacterial Activity of Zinc Oxide/Graphene Oxide Composites Localized around Bacteria.* Acs Applied Materials & Interfaces, 2014. **6**(4): p. 2791-2798.

69. Banoee, M., et al., *ZnO nanoparticles enhanced antibacterial activity of ciprofloxacin against Staphylococcus aureus and Escherichia coli.* Journal of Biomedical Materials Research Part B-Applied Biomaterials, 2010. **93B**(2): p. 557-561.

70. Hui, L.W., et al., *Availability of the Basal Planes of Graphene Oxide Determines Whether It Is Antibacterial.* Acs Applied Materials & Interfaces, 2014. **6**(15): p. 13183-13190.

71. Tu, Y.S., et al., *Destructive extraction of phospholipids from Escherichia coli membranes by graphene nanosheets.* Nature Nanotechnology, 2013. **8**(8): p. 594-601.

72. Ruiz, O.N., et al., *Graphene Oxide: A Nonspecific Enhancer of Cellular Growth.* Acs Nano, 2011. **5**(10): p. 8100-8107.

73. Xia, P.F., et al., *2D/2D g-C3N4/MnO2 Nanocomposite as a Direct Z-Scheme Photocatalyst for Enhanced Photocatalytic Activity.* Acs Sustainable Chemistry & Engineering, 2018. **6**(1): p. 965-973.

74. Kitchaev, D.A., et al., *Energetics of MnO2 polymorphs in density functional theory.* Physical Review B, 2016. **93**(4): p. 5132-5132.

75. Young, M.J., et al., *Band Diagram and Rate Analysis of Thin Film Spinel LiMn2O4 Formed by Electrochemical Conversion of ALD-Grown MnO.* Advanced Functional Materials, 2016. **26**(43): p. 7895-7907.

76. Silva, C.G., et al., *Influence of Excitation Wavelength (UV or Visible Light) on the Photocatalytic Activity of Titania Containing Gold Nanoparticles for the Generation of Hydrogen or Oxygen from Water.* Journal of the American Chemical Society, 2011. **133**(3): p. 595-602.

77. Rojas-Andrade M., N.T., Mistler W., Armas J., Lu J., Roseman G., Hollingsworth W., Nichols F., Millhauser G., Ayzner A., Saltikov C., Chen S., *Antimicrobial activity of graphene oxide quantum dots: impacts of chemical reduction* Royal Society of Chemistry, 2020. **2**: p. 1074-1083.

78. Yin, X., et al., *Simultaneous N-doping of reduced graphene oxide and TiO2 in the composite for visible light photodegradation of methylene blue with enhanced performance.* Rsc Advances, 2013. **3**(40): p. 18474-18481.

79. Seema, H., et al., *Graphene-SnO2 composites for highly efficient photocatalytic degradation of methylene blue*

under sunlight. Nanotechnology, 2012. **23**(35): p. 55705-55705.

80. Xu, J.J., M.D. Chen, and Z.M. Wang, *Preparation of CdWO4-deposited reduced graphene oxide and its enhanced photocatalytic properties.* Dalton Transactions, 2014. **43**(9): p. 3537-3544.

81. Zhu, C.Y., et al., *Contribution of alcohol radicals to contaminant degradation in quenching studies of persulfate activation process.* Water Research, 2018. **139**: p. 66-73.

82. Liu, C.N., et al., *Degradation of Rhodamine B by the alpha-MnO2/Peroxymonosulfate System.* Water Air and Soil Pollution, 2016. **227**(3): p. 92-92.

83. Buettner, G.R., *Spin trapping: ESR parameters of spin adducts.* Free Radic Biol Med, 1987. **3**(4): p. 259-303.

84. Chauvin, J., et al., *Analysis of reactive oxygen and nitrogen species generated in three liquid media by low temperature helium plasma jet.* Sci Rep, 2017. **7**(1): p. 4562.

85. Wang, H., et al., *Visible light induced electron transfer from a semiconductor to an insulator enables efficient photocatalytic activity on insulator-based heterojunctions.* Nanoscale, 2018. **10**(33): p. 15513-15520.

86. M., H.W., *CRC Handbook of Chemistry and Physics*. 96 ed. 2015, Boca Raton, FL: Taylor & Francis Group.

87. Ferradini, C. and J.P. Jay-Gerin, *The effect of pH on water radiolysis: A still open question - A minireview.* Research on Chemical Intermediates, 2000. **26**(6): p. 549-565.

88. de Groot, F.M., et al., *Oxygen 1s x-ray-absorption edges of transition-metal oxides.* Phys Rev B Condens Matter, 1989. **40**(8): p. 5715-5723.

89. Qiao, R.M., et al., *Spectroscopic fingerprints of valence and spin states in manganese oxides and fluorides.* Current Applied Physics, 2013. **13**(3): p. 544-548.

90. Pinaud, B.A., Chen Z., Abram D, Jaramillo T., *Thin Films of Sodium Birnessite-Type MnO2 : Optical Properties, Electronic Band Structure, and Solar Photochemistry.* The Journal of Photochemistry C, 2011 (115): p. 11830-11838.

91. Sakai, N., et al., *Photocurrent generation from semiconducting manganese oxide nanosheets in response to visible light.* J Phys Chem B, 2005. **109**(19): p. 9651-5.

92. Liang, H.F., et al., *The band structure of graphene oxide examined using photoluminescence spectroscopy.* Journal of Materials Chemistry C, 2015. **3**(48): p. 12484-12491.

93. Mei, Q.S., et al., *Graphene Oxide: From Tunable Structures to Diverse Luminescence Behaviors.* Advanced Science, 2019. **6**(14): p. 855-855.

94. Hsu, H.C., et al., *Graphene oxide as a promising photocatalyst for CO2 to methanol conversion.* Nanoscale, 2013. **5**(1): p. 262-268.

95. Lee, J.Y., et al., *Hydrogen-atom-mediated electrochemistry.* Nat Commun, 2013. **4**: p. 2766.

Chapter 3: Metal Chelated of GOQD via a Facile Aqueous Sonication Method with Biologically Active Second-Row Transition Metals

Gustavo Chata[a], Jia En Lu[a], Rene S. Mercado[a], Dion Chang[a], Chad Saltikov[b], and Shaowei Chen[a]

Department of Chemistry and Biochemistry, University of California, 1156 High Street, Santa Cruz, California 95064, USA

Department of Microbiology and Environmental Toxicology, University of California, 1156 High Street, Santa Cruz, California 95064, USA

The photocatalytic property of nanomaterials provides for a desirable tool for facile antibacterial activity. Photocatalytic efficacy of metal oxide, graphene oxide, and composite nanoparticles induce photodynamic activity towards Gram-Negative and Gram -Positive bacteria with excitation of monochromatic or visible light. The extent of antibacterial efficiency of such nanomaterials is attributed to the production of reactive oxygen species (ROS) which lack

cellular specificity. Therefore, when nanomaterials are utilized medically, ROS production may induce cell lysis to eukaryotic cells of the host. While the source of ROS production on nanomaterials play a critical role in the photodynamically driven antibacterial activity it hinders its biomedical application due to its non-site-specific cell targeting. Visible light driven excitation of metal oxide and composite nanoparticles have been found to induce cell death due to the high rate of ROS production. While such nanomaterials are efficacious for *in-vitro* activity against bacterial cells the efficacy of activity for *in-situ* experiments may be hampered. Herein, we utilize 3d transition metals chelated with graphene oxide to tune the overproduction of ROS by bypassing necessity of a large ensemble of metal oxide, metal, and carbon-based nanocomposites which lack biocompatibility due to overproduction of ROS. Among the examined GOQD-M^{2+} the metal ions tested included Co^{2+}, Cu^{2+}, Mn^{2+}, Fe^{2+}, Fe^{3+}, and Ni^{2+}. Enhanced photodynamic activity was found for GOQD-Co^{2+} under 365 nm excitation with atomic percentage of 0.75 Co/C evaluated via XPS..

3.1 Introduction

Bacterial resistance to antibiotics is driven by the genomic mutations which reconstruct bacterial metabolism to combat antibacterial activity. The rate of genomic mutation demands the application of novel antibiotics or combinations to prevent variation in an organisms' MIC [1]. Consistent exposure of a specific antibiotic to a microbial organism will inevitably inherit antibiotic resistance. Therefore, the continuous development of novel antibiotic procedure to combat the high rate of bacterial mutation is imperative in maintaining the efficacy of antibiotics [2-5]. Although methodical variations in antibiotic administration may provide a temporary solution to bacterial resistance, the high mutational rate of bacteria can eventually reconfigure the machinery of bacteria. The extent of adaption is such that even microorganisms treated with combinations of various antibiotics may exhibit resistance upon prolonged exposure [6]. Therefore, due to the surmounting necessity of alternative therapeutics the utility of nanoparticles as a vector for antibacterial activity has become more relevant.

A plethora of nanoparticles have been widely utilized against a variety of bacterial organisms. The mechanism of

bactericidal activity from biologically active nanoparticles spurs from ionization, nanoparticle-membrane interaction, or photon-induced ROS generation. The biomedical application of nanoparticles inducing bactericidal activity via ionization and nanoparticle-membrane interaction are limited by the extent of toxicity [7-12]. Nanoparticles utilizing such mechanisms require a relatively high concentration to induce bactericidal activity which unequivocally induces cytotoxic activity of eukaryotic cells due to ionization or nanoparticle-membrane interaction. Therefore, to enhance the biocompatibility of such nanomaterials it is critical to minimize the concentration of graphene oxide, metal oxide, and nanocomposite structures. The biomedical potential of nanoparticles is most prominent for metal oxide and graphene oxide composites which increase the electron-hole separation via photoexcitation mechanism which lead to production of ROS[13-17]. Photodynamic activity of ZnO nanoparticle structures have been found to be widely efficient in inducing antibacterial activity against Gram-Negative and Gram-Positive bacteria. The efficacy of photodynamic activity of ZnO is attributed to the band-gap energy and potential energy positions of its conductive and valence band. Although the compatibility of Zn^{2+} is present in

various biomolecules including superoxide dismutase (SOD), DNA/RNA polymerase, d-Amino-levulinic acid (dALA) dehydrogenase its low ionization energy facilitates its uncontrolled ionization[18].

Even the enhancement ZnO nanomaterials via ligand and structure modification suffer from increased Zn^{2+} ionization and destructive cell-membrane interaction[19-21]. The adaptation of ZnO functionalized on graphene oxide structures has enhanced its biocompatibility by decreasing total atomic ZnO concentration while utilizing the synergistic optical properties of both structures. In the pursuit of minimizing ionization of photoactive metal oxide, a series of second row transition metals were designed to explore the relevance of metal-oxide deposition onto graphene oxide quantum dots (GOQD) via complexation of the metal-ion to oxygen moieties. The facile sonication method of water-soluble M^{n+} ions produced a series of metal oxide free carbon structure with metal chelated structures as examined by high resolution transmission electron microscopy (HRTEM) and X-ray photoelectron spectroscopy (XPS). The rate constant of emission measured from time resolved fluorescence lifetime (TRFL) increased for GOQD-Co^{2+} at 365 nm excitation and GOQD-Mn^{2+} at 465 nm excitation in contrast to GOQD and

GOQD-M^{n+} samples. The enhanced photodynamic activity of GOQD-Co^{2+} at 365 nm correlates with enhanced lifetime of the excited electron. Methylene blue dye (MBD) degradation experiment at 365 nm excitation of GOQD-Co^{2+} did not exhibit an enhanced photocatalytic activity suggesting a ROS independent photocatalytic bactericidal mechanism.

3.2 Experimental Section

3.2.1 Chemicals

Cobalt nitrate hexahydrate (98 %), Manganese Chloride Tetrahydrate (99%), Ferrous Chloride Tetrahydrate (100%), Copper Acetate Monohydrate (98%), Nickel Acetate Tetrahydrate (99%), Ferric Chloride Hexahydrate (97.0%), potassium phosphate monobasic (99.0%), potassium phosphate dibasic (98.0%), pitch carbon fiber, Methylene Blue Dye (99.0%), nitric acid (70%) were supplied by Sigma Aldrich. Water was purified with a Barnstead Nanopure Water System (18 MΩ cm^{-1})

3.2.2 GOQD Synthesis

The synthesis of GOQD has been detailed previously. Pitch carbon fiber (1g) was immersed into a mixture of concentrated HNO_3 (40 mL) and H_2SO_4 (60 mL) in a round-

bottom flask. After two hours of sonication the carbon fibers were refluxed at 120 °C for 24 h. Once the solution was cooled to room temperature its pH was adjusted to pH 7 with NaOH. The solution was left overnight to allow for salts to precipitate out of solution. The supernatant, which contained the water-soluble GOQDs, were displaced from the solution and transferred to a cellulose dialysis bag and placed in Nanopure water for several days to afford purified GOQD.

3.2.3 Metal-chelated GOQD Synthesis

The GOQDs obtained was utilized to chelate a variety of transition metals including cobalt nitrate hexahydrate, manganese chloride tetrahydrate, ferrous chloride tetrahydrate, copper acetate monohydrate, nickel acetate tetrahydrate, and ferric chloride hexahydrate. The 25 mg of GOQD was solubilized in 2.5 mL of Nanopure Water with 250 µg of each respective metal salt. Each of the metal chelated GOQDs was sonicated at 25°C for 10 minutes. The solution was then transferred to a cellulose dialysis bag and placed in Nanopure water for several 48 hours with intermittent substitution of Nanopure water.

3.2.4 Characterization

The morphology and size of the samples were characterized by transmission electron microscopy measurements (TEM, Phillips CM 300 at 300 kV). UV-VIS absorption spectra were acquired with a Perkin Elmer Lambda 35 UV-VIS spectrophotometer and photoluminescence measurements were conducted with a PTI fluorospectrophotometer. X-ray photoelectron spectra (XPS) were recorded with a PHI 5400/XPS instrument equipped with an Al K_{α} source operated at 350 W and 10^{-9} Torr. TRPL decay spectra was collected on a Horiba QM-3304 instrument at the pulsed laser excitation of 335 nm in the time-correlated single-photon counting (TCSPC) mode.

3.2.5 Antimicrobial evaluation

In photodynamic antibacterial assessments, 200 µL of *E. coli* (OD 0.1) was transferred to a 1 mL plastic centrifuge tube, into which 600 uL of 0.1 mg/mL nanoparticles was added along with 200 µL of sterilized Nanopure water. The centrifuge tubes containing the *E. coli* and nanoparticles were irradiated with UV- photoirradiation (100 W, 1000-

1500 lumen with a peak with a peak emission at 365 nm and 465 nm, Dongguan Hongke Lighting Co, China). After irradiating the sample, each centrifuge tube was diluted by 100 folds at each respective time point. From the diluted solution, 10 µL was distributed evenly on an LB agar plate utilizing sterilized glass beads. Upon dispersion of nanoparticle and *E. coli* suspension on the LB agar plate, the agar plates were placed in a 37 °C incubator.

3.2.6 Methylene Blue Dye Preparation

Photocatalytic degradation of methylene blue was carried out by following a procedure described previously. Experimentally, a calculated amount of methylene blue (MB 450 uM was diluted to 3mL in a quartz cuvette to 45 uM with a corresponding sample prepared above. A volume of 140µL of 1.0 mg/mL concentration of M^{2+}-GOQD and GOQD was added to a total volume of 3 mL pH 7.2 with 45 uM methylene blue dye, where the pH was made with a potassium phosphate monobasic and potassium phosphate dibasic buffer. For the methylene blue dye control, the volume of photocatalyst was supplemented with pH 7.2 buffer. The solution was then irradiated with a 365 nm LED lamp, and UV-vis spectra were acquired at different time

intervals. For the methylene blue dye control, the volume of photocatalyst was supplemented with pH 7.2 buffer. The solution was then irradiated with a 365 nm LED lamp, and UV-vis spectra were acquired at different time intervals.

3.3 Results

The modified Hummer's method for GOQD synthesis leads produces a large sheet like structure which extends in size beyond 50 nm (Figure 1 a,b). Close examination of large sheet-like GOQD structures depict GOQD nanoparticles with distinct lattice fringes of 0.24 nm corresponding to a lattice fringe of (1120) [22-24]. The macromolecular morphology of GOQD is present due to its distribution of sp^2 domains within the GOQD structure, therein creating an agglomerate of smaller domains separated via oxidized functional groups[25] [26]. A 16 hour reflux of pitch fiber with nitric acid and sulfuric acid leads to an average diameter size of 10-20 nm which is observed in Figure 1 c) and d) corresponding to a similar domain size exhibited by *Rojas-Andrade et al*. [26]. While the structural composition of (Figure 1 a-d) corresponds to GOQD-Co^{2+}, the sample does not demonstrate the appearance of Co oxide structures which may have developed via hydrolysis reaction. Specially since Co oxide formation does not occur unless

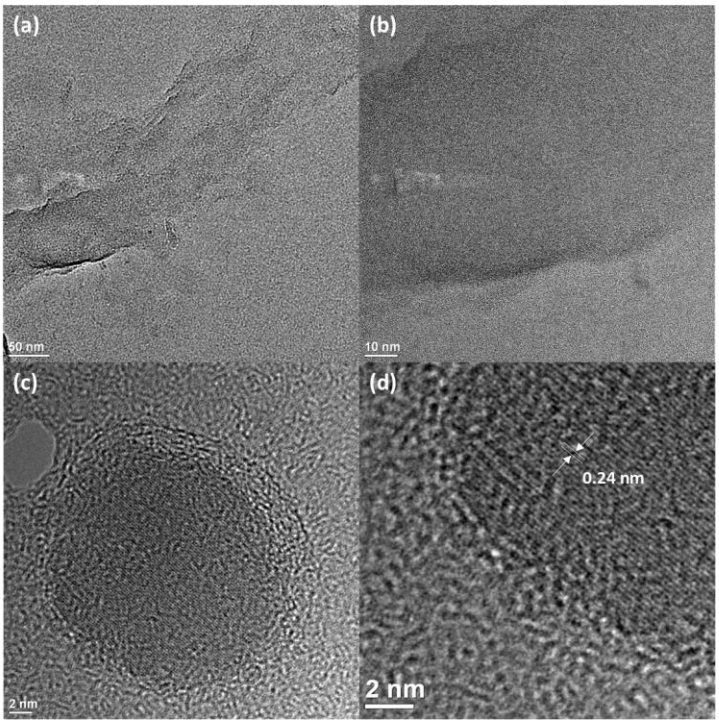

Figure 1: a,b) Representative TEM image of a GOQD-Co^{2+}nanosheets c,d)

synthesized under a high temperature reaction over 100 ^{o}C [27-31]. Although the synthesis technique by *Tonh et al.* [32] was utilized to produce the chelated M^{2+} - GOQD structure, the resulting modified GOQD structure was not treated at high temperature in the presence of reducing agents like H_2. Further observation of the UV-VIS spectra

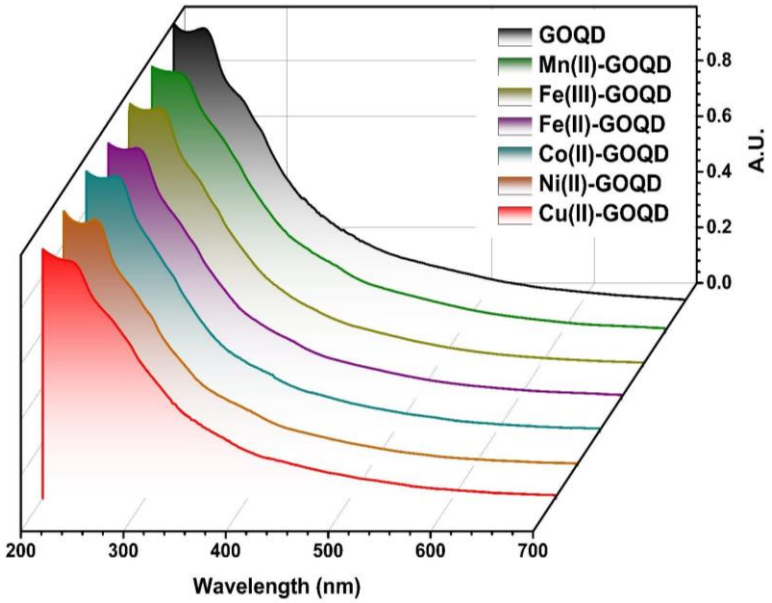

Figure 2: UV-VIS Spectra of GOQD and the GOQD-M^{2+} series

representative TEM image of Co^{2+}-GOQD nanoparticle electronic transitions of chemical moieties functionalized onto GOQD.

depicts the electronic transitions of GOQD and M^{2+}-GOQD structures shows the presence of the major peaks at 240nm, 260 nm, and 280 nm are due to the $\pi\square\pi^*$ electronic transition which are dominated by the size of the sp^2 structures and presence of sp^3 groups charge mobility through GOQD structure [33, 34]. The presence of such spectroscopic features through all GOQD chelated M^{2+} suggest the sonication of GOQD in the presence of each respective metal salt maintains the GOQD chemical and structural composition (Figure 2). Furthermore, the decrease in

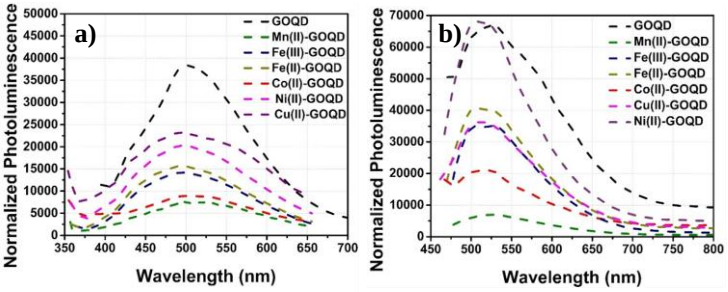

Figure 3 a) Photoluminescence Emission Spectra of GOQD and M^{2+}-GOQD series corresponding to a 335 nm excitation wavelength b) Photoluminescence Emission Spectra of GOQD and M^{2+}-GOQD series corresponding to a 465 nm excitation wavelength.

absorption from all peaks associated with $\pi \rightarrow \pi^*$ transitions lead to the inclusion of an electronic state throughout all GOQD-M^{2+} samples which affect the predominant $\pi \rightarrow \pi^*$ transition existent in bare GOQD sample.

The excitation wavelengths of 335 nm and 465 nm from GOQD are present due to the size of sp^2 domains and presence of sp^3 functional groups. The dependence of emission wavelength from the excitation wavelength can be attributed to an excitation mechanism originating from dissimilar functional groups. The 500 nm emission from an excitation wavelength of 335 nm corresponds to a $\sigma^* \rightarrow n$ transition which is a dominant transition in GOQD structures with an increased concentration of functionalized. A

broadened excitation wavelength from 300 nm to 420 nm correlates to electronic transitions from C=O moieties[35]. In a study by *Li et al.* oxidation of GOQD with HNO_3 produces a -OH and C=O functionalized GOQD structure with emission wavelengths present at 470 nm and 520 nm, which are respective to $\sigma^* \rightarrow n$ and $\pi^* \rightarrow \pi$ transitions. The broad emission from 400 nm to 600nm from 335 nm excitation of GOQD indicates that such an excitation is due to sp^2 domains, C-OH, and C=O functional groups on GOQD. The emission profile from the 335 nm excitation of GOQD contains a larger FWHM in contrast to the emission from 450 nm excitation. Furthermore, the emission peak is centered at 550 nm which corresponds mainly to $\pi^* \rightarrow \pi$ transitions[34]. Herein the GOQD fluorescence spectra is due to either a contribution of sp^2 and sp^3 moieties from the 335 nm excitation and a contribution mainly from sp^2 moieties. Although the theoretical bandgap for $\pi \rightarrow \pi^*$ transitions is 3.86 eV (i.e. 310 nm) [36] the dominant peak at 335 nm is due to the high oxidation of the graphene

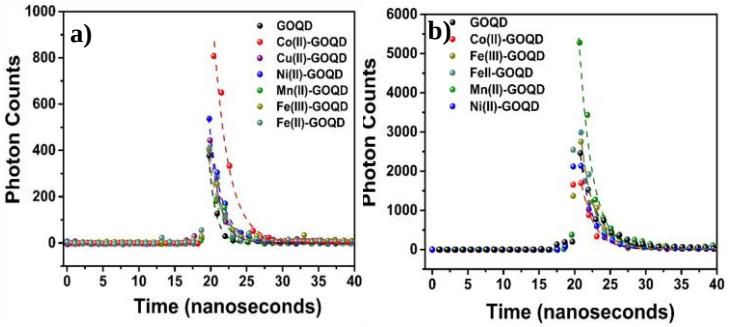

Figure 4 a)Time Resolved Fluorescence Lifetime (TRFL) at 365 nm excitation for GOQD and GOQD-M^{2+} series b) TRFL at 465 nm excitation for GOQD and GOQD-M^{2+}

series frame [37]. Furthermore, the presence of bimodal excitation spectra

hydroxide groups (Figure 3 a) is due to larger sp^2 frames as evidenced by *Dong et al.* via fine tuning of Graphene Oxide by tuning the carbonization degree of citric acid[38].

Due to the acidity of metal salts, they can readily interact with more basic moieties functionalized on the GOQD. A diminished fluorescence emission intensity for all GOQD-M^{2+} samples is measured under both 335 nm and 465 nm excitation (Figure 3 a,b). Regardless of excitation wavelength the normalized fluorescence intensity of GOQD-M^{2+} diminishes when GOQD is chelated with a metal with a

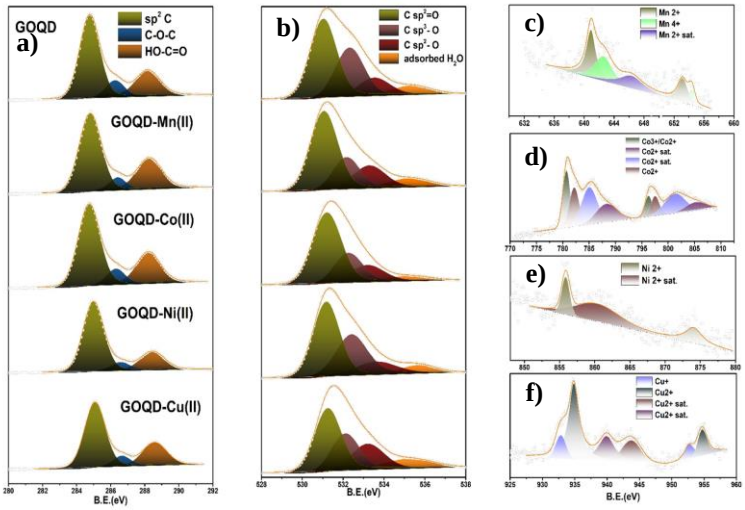

Figure 5: XPS of a) High resolution C1s spectra for GOQD and GOQD-M^{2+} samples b) O1s spectra for GOQD and GOQD-M^{2+} samples c) Mn 2p d) Co 2p e) Ni 2p and f) Cu 2p spectra for GOQD-M^{2+} samples lower atomic number. At 335 nm excitation the normalized intensity for GOQD-M^{2+} decreases in the following order Cu(II) > Ni(II) > Fe(II) > Fe(III) > Co(II) > Mn (II) (Figure 3 a). Similarly at 465 nm excitation the normalized intensity for GOQD-M^{2+} decreases in the following order Ni(II) > Fe(II) > Fe(III) ~ Cu(II) Co (II) > Mn (II) (Figure 3 b). fluorescence intensity for GOQD structure has been attributed to the vacancy of the 3d orbital for transition metals has been attributed by various groups [39-42]. The high extent of quenching for Fe(III) instead of Mn(II) can be attributed to the high concentration of phenol sites which was evaluated by

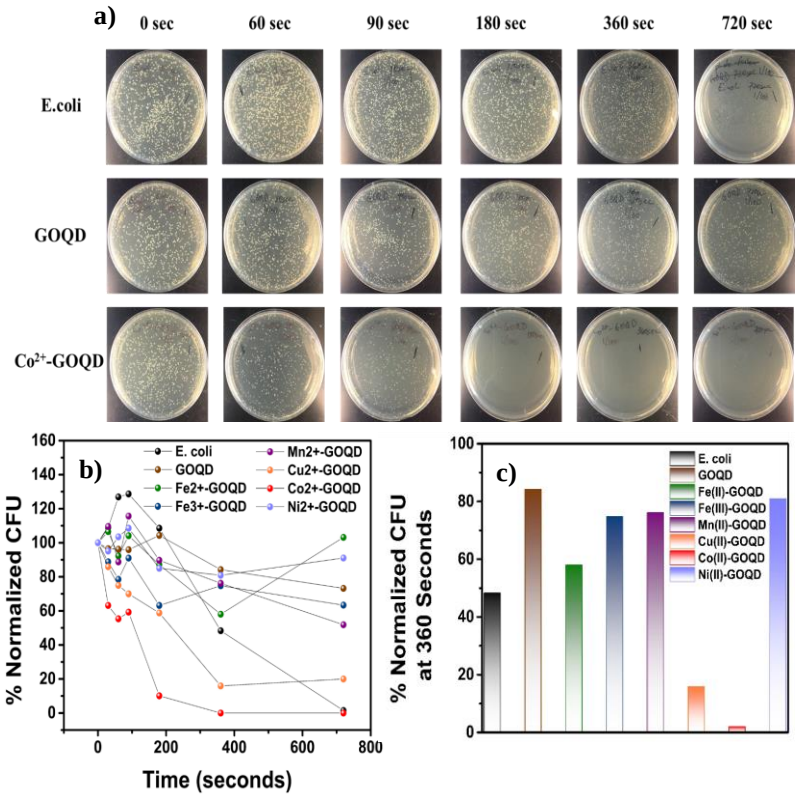

Figure 6: a) Photodynamic Activity of *E. coli* measured at respective time points of 365 nm LED irradiation b) Normalized CFU of *E.coli* irradiated at 365 nm LED at various tie points c) Percentage of Normalized CFU with respect to initial CFU measured at 360 seconds of irradiation

Wang et al. who found a GOQD with extensive concentration of phenols to be more sensitive to Fe(III)[42]. Smaller sp^2 domain sites do not quench GOQD fluorescence due to the vacancy of the 3d orbital of the 3d transition metal. An example of these structures include fullerene derived

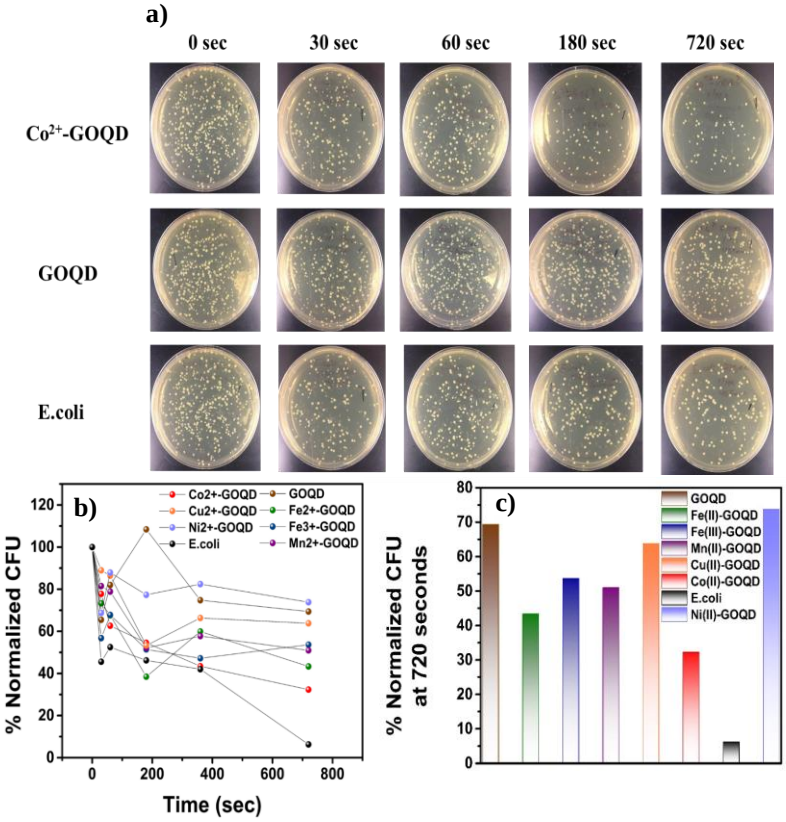

Figure 7: a) Photodynamic Activity of *E. coli* measured at respective time points of 465 nm LED irradiation b) Normalized CFU of *E.coli* irradiated at 465 nm LED at various tie points c) Percentage of Normalized CFU with respect to initial CFU measured at 720 seconds of irradiation

graphene oxide quantum dots or unfolded fullerene quantum dots (UFQD) which are quenched vastly by Cu(II)

[43, 44].Energy charge transfer between UFQD and to chelated metal ions as well as the change in nonradiative

charge transfer of aggregated UFQDs is associated with decreased fluorescence according to *Ciotta et al.*[44].

The lower electron configuration of 3d orbitals from the 3d block transition metals could allow for enhanced electron transfer from the GOQD structure to the metal chelated to GOQD sites. A diminished fluorescence lifetime data supports the observed quenched fluorescence from GOQD-M^{2+} structures. At 365 nm excitation all GOQD-M^{2+} maintain a higher average lifetime constant $\tau_{avg.}$ (from equation 1) to GOQD. The τ_{avg} for all GOQD-M^{2+} and GOQD at an excitation of 365 nm increased in the following order GOQD < Cu (II) < Mn (II) < Fe (II) ~ Fe (III) ~ Ni (II) < Co (II) . The variation of τ_{avg} from the GOQD-M^{2+} closely resemble the diminished fluorescence intensity of GOQD at 365 nm excitation (Figure 4 a). The direct correlation between normalized fluorescence intensity indicates the relaxation of excited electrons to the π energy state of GOQD. Deviations of such a relationship between τ_{avg} indicate the excited electrons are relaxing to lower energic state via nonradiative pathways or are reactive with dissolved oxygen or water molecules via trapped states. The samples which do not follow a direct correlation with normalized fluorescence intensity and τ_{avg} include Mn(II)-

GOQD, Cu(II)-GOQD, and Co(II)-GOQD. In contrast to the τ_{avg} at 365 nm excitation, the τ_{avg} at 465 nm increased in the following order GOQD < Cu(II) < Fe(II) ,Ni(II) < Co (II) ~ Mn (II) < Fe (III) (Figure 4b). The 365 nm emission spectra, which is closer to the 335 nm excitation position, originates fluorescence from both sp^2 and sp^3 functional groups while 465 nm emission originates from sp^2 functional groups. The drastic effect of Fe(III) on τ_{avg} at 465 nm excitation is supported by the known interactions of Fe(III) with phenolic functional groups on GOQD which readily quench fluorescence [42]. In the C1s and O1s spectra of GOQD, Mn(II)-GOQD, Co(II)-GOQD, Ni(II)-GOQD, and Cu(II)-GOQD the peaks related to oxygenated functional groups on GOQD maintain the binding energy found for GOQD (Figure 5). The similarity of the binding energy of C1s and O1s of GOQD-M^{2+} to GOQD is attributed to the high percentage of 2+ valency measured from the 2p spectra of each respective metal. In contrast to the other M^{2+}-GOQD samples, the Cu(II)-GOQD sample contains a peak at the $2p^{3/2}$ peak at 932.85 eV and $2p^{3/2}$ to $2p^{1/2}$ peak splitting of 20 eV which is distinguishable peak for a Cu(0) or Cu(I)[45-50]. Since the $Cu(NO_3)_2$ salt is sonicated in the presence of GOQD in order to chelate the Cu(II) onto the GOQD the vibrational energy of water along

with the positive redox potential for Cu (II) + e^- = Cu(I) can lead to the production of Cu_2O nanoparticles. According to *Bau et al.* sonication of $Cu(NO_3)_2$ in water leads to the production of Cu_2O nanoparticles as evidenced from XPS and TEM [50]. The elemental percentage of Cu(I) from the total Cu composition of Cu(II)-GOQD is 26.39% measured from Cu 2p spectra. The absence of 530.0 eV peak, corresponding to the O_{lat} of Cu_2O, suggests the total concentration of Cu_2O to be relatively low[50]. Similar to formation of Cu_2O nanoparticles from sonication of $Cu(NO_3)_2$ sonication in water, the sonication of manganese salt in water leads to formation of Mn_3O_4 nanoparticles. The Mn 2p spectra from Figure XX c contains two distinct Mn $2p^{3/2}$ peaks at 640.91 eV and 642.59 eV which corresponds to Mn^{2+} and Mn^{4+} respectively[51, 52]. The difference in binding energy between $2p^{3/2}$ and $2p^{1/2}$ between Mn^{2+} and Mn^{4+} is near 12.0 eV for both Mn signals (Figure 5 c). In a study by *Suktha et al.* nanoparticles of Mn_3O_4 by ultrasonication of Mn^{2+}, which is proposed to occur via hydrolysis [53, 54]. Therefore, oxidation of Mn^{2+} may be facilitated under an ultrasonicating environment. In contrast to GOQD-Mn^{2+} and GOQD-Cu^{2+} which produce metal oxide nanoparticles via ultrasonication of M^{2+} with GOQD, the ultrasonication of Co^{2+} and Ni^{2+} with

GOQD maintain their 2+ valency regardless of the ultrasonication procedure (Figure 5 d,e). The Co 2p (Figure 5 d) depicts two major peaks for Co $2p^{3/2}$ at 780.87 eV and 782.01 eV which can both be attributed to Co^{2+}. The variance in binding energy position of 2 $p^{3/2}$ peak of Co arises from the coordination of oxygen atoms surrounding the Co^{2+} atom. A $2p^{3/2}$ binding energy at 780.4 eV is attributed to CoOOH while a binding energy at 782.01 eV is attributed to $Co(OH)_2$ [55-58]. Furthermore, the two set of satellite peaks designated at 785.38 eV and 788.71 eV is within the region of the satellite peak of Co with an oxidation state of 2+. Another set of satellite peaks are found at higher binding energies of 801.21 eV and 804.5 eV which are also within the satellite region Co^{2+} [25, 59]. Two signature satellite peaks for Co^{2+} sample indicates variation in the valence band structure of Co^{2+} due to different coordinated sites [56, 59]. Previous studies have found chelation of Co^{2+} to phenol structures on benzoquinones and hydroxide on bis(salicylidene) based ligands [60, 61]. Therefore, the two discrete Co^{2+} peaks in the $2p^{3/2}$ region of Co 2p

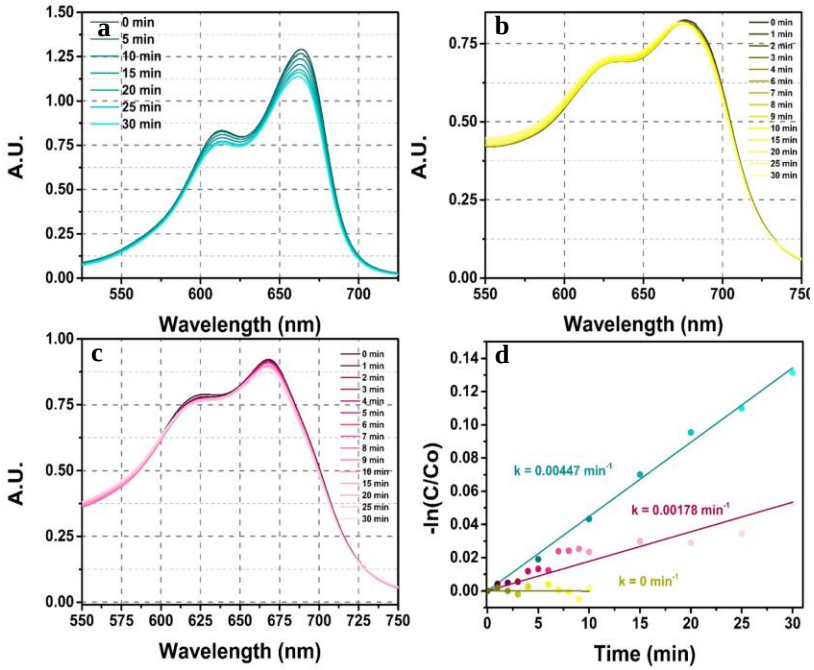

Figure 8: a) Methylene Blue Dye degradation at 365 nm excitation with a) no catalyst, b) GOQD-Co^{2+}, and c) GOQD-Cu^{2+}. d) measures the rate of degradation of methylene blue tested in the presence and absence of catalyst with 365 nm excitation LED

spectra could be originating from Co-OH of Co-O= coordination. The GOQD-Ni^{2+} sample also maintains its 2+ valency as indicated by the Ni 2p spectra (Figure 5 e). A binding energy for $2p^{3/2}$ of the Ni 2p spectra at 855.8 eV is consistent for a Ni^{2+}, specifically for a $Ni(OH)_2$ structure[51, 62, 63]. The photodynamic activity of GOQD-M^{2+} was quantified by measuring CFU over irradiation time at 365 nm

and 465 nm excitation (Figure 6 and 7). At 365 nm the Co^{2+}-GOQD demonstrated an enhanced photodynamic activity in contrast to *E. coli* and GOQD with *E. coli* irradiated at 365 nm excitation (Figure 6 a). The time of cell death (TCD) for *E. coli* at an excitation wavelength of 365 nm occurs at 720 sec, but in the presence of GOQD-Co^{2+} the TCD decreases to 360 seconds. The chelation of Co^{2+} to GOQD structure substantially enhances the photodynamic activity since GOQD contains no TCD within the irradiated time lapse (Figure 6 b). The photodynamic activity of GOQD-Co^{2+} contains the lowest TCD in contrast to other transition metals chelated with GOQD (Figure 6 c) since it contains the lowest percentage of normalized colony forming units in contrast to other GOQD-M^{2+}. The GOQD-Cu^{2+} exhibits a 18% normalized CFU at 360 seconds which is lower than the percentage of normalized CFU (~50%) at 360 seconds of irradiation with 365 nm light with only *E. coli* (Figure 6 c). Although the GOQD-Cu^{2+} is not effective in complete eradication of the *E. coli* population since the percentage of normalized CFU stays constant at 18 % normalized CFU at 720 seconds (Figure 6 c). The photodynamic activity of GOQD-M^{2+} was also tested at an excitation wavelength of 465 nm (Figure 6). The GOQD-M^{2+} were found to not have enhanced photodynamic activity

in comparison to *E. coli* irradiated at the excitation wavelength of 465 nm (Figure 7a). Like the photodynamic activity tested at 365 nm excitation, GOQD-Co^{2+} maintained the lowest percentage of normalized CFU at 720 sec for the GOQD-M^{2+} samples and GOQD (Figure 7c). In contrast to the photodynamic activity at 365 nm, GOQD-Cu^{2+} proves to be a less effective phototherapeutic at an excitation wavelength of 465 nm since the percentage of normalized CFU is ~ 65% at 720 sec, which is greater than the percentage of normalized CFU recorded at an excitation wavelength of 365 nm ~18%. Under both excitation wavelengths the photodynamic activity of GOQD-M^{2+} proves to have a lower percentage of CFU at the respective measured time point in contrast to GOQD.

To understand the mechanism of photodynamic activity of GOQD-Co^{2+} and GOQD-Cu^{2+}, both samples were irradiated at 365 nm and 465 nm in the presence of methylene blue dye (Figure 8 and 9). Under both excitation wavelengths the rate constant k_{MBD} was found to be lower for both GOQD-Co^{2+} and GOQD-Cu^{2+} in contrast to the methylene blue dye control (Figure 8 and Figure 9). The GOQD-Co^{2+} maintained a higher rate of degradation (k_{MBD}) in

contrast to GOQD-Cu^{2+} under both 365 nm and 465 nm excitation.

3.4 Discussion

The photodynamic activity of GOQD-Co^{2+} proves to be the most efficient under both tested excitation wavelengths (Figure 6 and 7). Photoluminescence spectra and lifetime decay measurements suggest that excited electrons from GOQD structure lead to the observed photodynamic activity. Specifically, the chelation of M^{2+} to GOQD structure enhances the photodynamic activity of GOQD structure at both excitation wavelengths of GOQD (Figure 6 and 7). In contrast to other GOQD-M^{2+} samples, GOQD-Co^{2+} contains a highly quenched photoluminescence at excitation wavelengths of 365 nm and 465 nm. The greatest lifetime constant τ_{365nm} can be attributed to GOQD-Co^{2+} which suggests the quenched signal from photoluminescence spectra results from efficient separation of electron-hole separation via inclusion of Co^{2+} (Figure 3). While GOQD-Co^{2+} is highly quenched at an excitation of 465 nm excitation, the fluorescent lifetime constant at 465 nm does not starkly contrast the lifetime of GOQD (Figure 4). Like GOQD-Co^{2+}, the difference τ_{465nm} for all GOQD-M^{2+} with GOQD is lower than at excitation of 365nm. The decrease in

the lifetime constant difference between GOQD-M^{2+} and GOQD can be due to the variation in functional groups excited at each respective wavelength. At an excitation wavelength of 365 nm sp^2 and sp^3 functional groups are excited, such functional groups include carbonyls, hydroxide, epoxides, ketones which M^{2+} can be functionalized to GOQD via oxidized functional groups. effective coordination of M^{2+} to hydroxyl functional groups of GOQD depends on the reduction potential of M^{2+} and effective electronic interaction of oxygen moieties functionalized on GOQD with M^{2+}.

Upon sonication of the GOQD structure, the GOQD initiates an exfoliation mechanism which can lead to bond cleavage near GOQD edge sites [64, 65]. Diffusion of the M^{2+} is assisted by a facile exfoliation of GOQDs domains from aggregates, although chemical diffusion from charged functional groups is driven by dissolved metal ions. Hydrolysis of metal ion in water may lead to metal oxide formation dependent on the reduction potential of specific metal ion [66, 67]. The reduction of Cu^{2+} to Cu^{1+} is spontaneous under conditions due to its standard reduction potential of E^o = 0.16 V. Therefore, the chelation of Cu^{2+} onto GOQD at pH = 7.0 and temperature of 25.0 ^oC could have

been hampered by Cu_2O formation in solution which could have led to a lower concentration of chelated Cu^{2+} onto GOQD. Inspection of Cu 2p spectra demonstrate presence of Cu^{1+} species which could be due to a reduced ionic species formed from solvent or GOQD oxidation (Figure 5 f). In contrast to GOQD-Cu the GOQD-Co and Ni sample maintain an oxidation state of 2+ which can be attributed to the negative standard reduction potential of Co^{2+} to Co(0) and Ni^{2+} to Ni(0) (E^o_{Co} = -0.28 Vand E^o_{Cu} = -0.25 V) (Figure 5 d and e). Therefore, a higher concentration of Co^{2+} and Ni^{2+} maintained in its ionic state upon chelation of hydroxyl and phenol moieties of GOQD. The GOQD-Mn^{2+} contains a higher oxidation state of 4+ although the reduction potential of Mn 2+ to Mn 4+ is -1.29 V (Figure 5 c). The oxidation of Mn^{2+} into Mn^{4+} can occur via H_2O_2 formation which is produced upon ultrasonication via hydroxyl radical formation[68]. In methylene blue dye (MBD) degradation experiments at 365 nm and 465 nm the rate of degradation decreased for both GOQD-Co^{2+} and GOQD-Cu^{2+} in comparison to the control (Figure 8 and 9). A decrease in the rate of degradation suggests a close interaction with the *E. coli* cell membrane were the H_2O_2 generation is higher intracellularly. In the

photodynamic experiments the intracellular H_2O_2 could be utilized to $HO^{\cdot -}$ via the metal chelated GOQD site.

3.5 Conclusion

The sonication of 3d transition metals in the presence of GOQD leads to the chelation of metal ions onto the GOQD structure as measured via XPS (Figure 5). Although the efficacy of chelation is dependent upon the metal ion's standard reduction potential, diffusion, and rate of chemical exfoliation of GOQD sheets from aggregates. Variation of the chelated metal ion's oxidation state suggest possible oxidation or reduction through solvent facilitation. An oxidation state of 2+ appears to be preferable for enhanced photodynamic activity as depicted by the enhanced photodynamic activity of GOQD-Co^{2+} and GOQD-Cu^{2+} which maintain high percentage oxidation state of 2+ as calculated from Co 2p and Cu 2p XPS spectra. Although the orbital configuration of Co2+ and Cu2+ may be ideal if there is charge transfer during the photodynamic process since GOQD-Ni also maintains an oxidation state of 2+ but photodynamic activity at both excitation wavelengths is like GOQD. Fluorescence spectroscopy indicates the successful chelation of all metal ions tested, with Co^{2+} and Mn^{2+} chelated GOQD samples with the most pronounced

quenching. Although the fluorescence lifetime constant at 365 nm of GOQD-Co^{2+} is substantially longer than other GOQD-M^{2+}. A drastic difference in the fluorescence lifetime at 365 nm for GOQD-Co^{2+} suggests the photodynamic activity of GOQD-M^{2+} occurs in the conduction band of GOQD where electrons could be transferred to Co^{2+}. Although the methylene blue dye degradation experiments at 365 nm indicate that in the absence of H_2O_2 the photodynamic activity of GOQD-Co^{2+} is lower than GOQD. Therefore in order to understand the photodynamic mechanism of GOQD-Co^{2+} the methylene blue dye experiment should be reevaluated in the presence of H_2O_2 to determine if intracellular H_2O_2 concentration of *E.coli* could impact the photodynamic activity.

3.6 References

1. Didelot, X., et al., *Transforming clinical microbiology with bacterial genome sequencing.* Nat Rev Genet, 2012. **13**(9): p. 601-612.
2. Rose, W.E., et al., *Ability of Bicarbonate Supplementation To Sensitize Selected Methicillin-Resistant Staphylococcus aureus Strains to beta-Lactam Antibiotics in an Ex Vivo Simulated Endocardial Vegetation Model.* Antimicrob Agents Chemother, 2020. **64**(3).
3. H. Miller, M.B., *Beta-Lactam Antibiotic Potentiation in MRSA Using Small Molecule Adjuvants* Federation of American Societies for Experimental Biology. **34**(1): p. 1.
4. Gallagher, L.A., et al., *Impaired Alanine Transport or Exposure to d-Cycloserine Increases the Susceptibility of MRSA to beta-lactam Antibiotics.* J Infect Dis, 2020. **221**(6): p. 1000-1016.
5. T. Kauss, C.A., L. Bientz, P. Vinh Nguyen, B. Vialet, S. Benizri, & P. Bathelemy, *Lipid Oligonucleotides as a New Strategy for Tackling Antibiotic Resistance.* Scientific Reports, 2020. **10**(1): p. 1-6.

6. J. Liu, O.G., I. Rorin, M. Bar-Meir, N. Q. Balaban, *Effect of Tolerance on the Evolution of Antibiotic Resistance under Drug Combinations* Science, 2020. **367**(6474): p. 200-204.

7. I. Persaud, A.R., A. Paruthi, N. Alsaleh, V. Minarchick, J. Roede, R. Podila, J. Brown, *Defect-Induced Electronic States Amplify the Cellular Toxicity of ZnO Nanoparticles.* Nanotoxicology, 2019. **14**(2): p. 145-161.

8. I. Ivanova, D.S., E. Nenova, A. Kostadinova, A. Staneva, *Antimicrobial and Cytotoxic Properties of Metal Nanoparticles and Graphene Materials.* Journal of Chemical Technology and Metallurgy, 2020. **55**(2): p. 239-250.

9. M. Saliani, R.J., and E. K. Goharshadi, *Mechanism of Oxidative Stress Involved in the Toxicity of ZnO Nanoparticles Against Eukaryotic Cells.* Nanomedicine Journal, 2016. **3**(1): p. 1-14.

10. J. Gagnon, K.F., *Toxicity and Protective Effects of Cerium Oxide Nanoparticles (Nanoceria) Depending on Their Preparation Method, Particle Size, Cell Type, and Exposure Route.* European Journal of Inorganic Chemistry, 2015. **2015**(27): p. 4510-4517.

11. Rozhina, E., et al., *Kaolin alleviates the toxicity of graphene oxide for mammalian cells.* Medchemcomm, 2019. **10**(8): p. 1457-1464.

12. Q. Yu, B.Z., J. Li, T. Du, X. Yi, M. Li, *Graphene Oxide Significantly Inhibits Cell Growth at Sublethal Concentrations by Causing Extracellular Iron Deficiency.* Nanotoxicology, 2017. **11**(9-10): p. 1102-1114.

13. L. Sun, T.D., C. Hu, J. Chen, J. Lu, Z. Lu, and H. Han, *Antibacterial Activity of Graphene Oxide/g-C_3N_4 Composite through Photocatalytic Disinfection under Visible Light.* Acs Sustainable Chemistry & Engineering, 2017. **5**: p. 8693-8701.

14. Kumar, R., et al., *Efficient ZnO-based visible-light-driven photocatalyst for antibacterial applications.* ACS Appl Mater Interfaces, 2014. **6**(15): p. 13138-48.

15. O. Akhavan, R.A., S. Safa, and M. M. Larijani, *Visible Light Photo-Induced Antibacterial Activity of CNT-doped TiO_2 thin films with various CNT contents.* Journal of Materials Chemistry 2010. **20**: p. 7386-7392.

16. Y. Wang, H.F., Y. Zheng, R. Ye, X. Tao, and J. Chen, *Controllable Assembly of Well-Defined Monodisperse Au Nanoparticles on Hierarchical ZnO Microspheres for Enhanced Visible-Light-Driven Photocatalytic and Antibacterial Activity.* Nanoscale, 2015. **7**: p. 19118-19128.

17. R. Gupta, N.E., J. Modak, and G. Madras, *Visible Light Driven Efficient N and Cu co-doped ZnO for Photoianctivation of Escherichia coli.* Rsc Advances, 2016. **6**: p. 85675-85687.

18. H. Qiu, B.M., Y. Wang, and C. Woll, *Ionization Energies of Shallow Donor States in ZnO Created by Reversible Formation and Depletion of H Interstitials.* Physical Review Letters, 2008: p. 1-4.

19. L. Zhao, R.Z., J. Zhang, and S. Sun, *Synthesis and Characterization of Biocompatible of ZnO Nanoparticles.* Crystengcomm, 2012. **14**: p. 945-950.

20. Yin, Y., et al., *Cytotoxic effects of ZnO hierarchical architectures on RSC96 Schwann cells.* Nanoscale Res Lett, 2012. **7**: p. 439.

21. J. Zhou, N.X., and Z. Wang, *Dissolving Behavior and Stability of ZnO Wires in Biofluids: A Study on Biodegradability and Biocompatability of ZnO Nanostructures.* Advanced Materials, 2006. **18**: p. 2432-2435.

22. Peng, J., et al., *Graphene Quantum Dots Derived from Carbon Fibers.* Nano Letters, 2012. **12**(2): p. 844-849.

23. Wu, J.X., et al., *Investigation of the Microstructures of Graphene Quantum Dots (GQDs) by Surface-Enhanced Raman Spectroscopy.* Nanomaterials, 2018. **8**(10): p. 864-864.

24. Deng, J.H., et al., *Large scale preparation of graphene quantum dots from graphite oxide in pure water via one-step electrochemical tailoring.* Rsc Advances, 2015. **5**(38): p. 29704-29707.

25. Wenkai Zhang, Y.L., Xianrui Meng, Tao Ding, Yuanqing Xu, Hao Xu, Yanrong Ren, Baoying Liu, Jiajia Huang, Jinghe Huang, Jinghe Yang, and Xiamin Fang, *Graphenol Defects Induced Blue Emission Enhancement in Chemically Reduced Graphene Quantum Dots* Physical Chemistry Chemical Physics, 2015. **17**: p. 22361-22366.

26. Mauricio D. Rojas-Andrade, T.A.N., William P. Mistler, Juan Armas, Jia En Lu, Graham Roseman, William R. Hollingsworth, Forrest Nichols, Glenn L. Millhauser, Alexander Ayzner, Chad Saltikov, Shaowei Chen, *Antimicrobial Activity of Graphene Oxide Quantum Dots: Impacts of Chemical Reduction.* Nanoscale Advances, 2020. **2**: p. 1074-1083.

27. Fu, L., et al., *Beaded cobalt oxide nanoparticles along carbon nanotubes: Towards more highly integrated electronic devices.* Advanced Materials, 2005. **17**(2): p. 217-+.

28. Yang, J., et al., *Synthesis and Characterization of Cobalt Hydroxide, Cobalt Oxyhydroxide, and Cobalt Oxide*

Nanodiscs. Journal of Physical Chemistry C, 2010. **114**(1): p. 111-119.

29. Sun, S.H. and C.B. Murray, *Synthesis of monodisperse cobalt nanocrystals and their assembly into magnetic superlattices (invited).* Journal of Applied Physics, 1999. **85**(8): p. 4325-4330.

30. Farhadi, S., J. Safabakhsh, and P. Zaringhadam, *Synthesis, characterization, and investigation of optical and magnetic properties of cobalt oxide (Co3O4) nanoparticles.* Journal of Nanostructure in Chemistry, 2012. **3**(1).

31. Cao, A.M., et al., *Hierarchically structured cobalt oxide (Co3O4): The morphology control and its potential in sensors.* Journal of Physical Chemistry B, 2006. **110**(32): p. 15858-15863.

32. Toh, R.J., et al., *Transition Metal (Mn, Fe, Co, Ni)-Doped Graphene Hybrids for Electrocatalysis.* Chemistry-an Asian Journal, 2013. **8**(6): p. 1295-1300.

33. Eda, G., et al., *Blue Photoluminescence from Chemically Derived Graphene Oxide.* Advanced Materials, 2010. **22**(4): p. 505-+.

34. Li, M., et al., *Fingerprinting photoluminescence of functional groups in graphene oxide.* Journal of Materials Chemistry, 2012. **22**(44): p. 23374-23379.

35. Gan, Z.X., et al., *Mechanism of Photoluminescence from Chemically Derived Graphene Oxide: Role of Chemical Reduction.* Advanced Optical Materials, 2013. **1**(12): p. 926-932.

36. Gan, Z.X., H. Xu, and Y.L. Hao, *Mechanism for excitation-dependent photoluminescence from graphene quantum dots and other graphene oxide derivates: consensus, debates and challenges.* Nanoscale, 2016. **8**(15): p. 7794-7807.

37. Liu, F., et al., *Facile Synthetic Method for Pristine Graphene Quantum Dots and Graphene Oxide Quantum Dots: Origin of Blue and Green Luminescence.* Advanced Materials, 2013. **25**(27): p. 3657-3662.

38. Dong, Y.Q., et al., *Blue luminescent graphene quantum dots and graphene oxide prepared by tuning the carbonization degree of citric acid.* Carbon, 2012. **50**(12): p. 4738-4743.

39. Kundu, A., et al., *Highly Fluorescent Graphene Oxide-Poly(vinyl alcohol) Hybrid: An Effective Material for Specific Au3+ Ion Sensors.* Acs Applied Materials & Interfaces, 2012. **4**(10): p. 5576-5582.

40. Wang, F.X., et al., *Graphene quantum dots as a fluorescent sensing platform for highly efficient detection of copper(II)*

ions. Sensors and Actuators B-Chemical, 2014. **190**: p. 516-522.

41. Wang, D.Y., et al., *Photoluminescence quenching of graphene oxide by metal ions in aqueous media.* Carbon, 2015. **82**: p. 24-30.

42. Wang, D., et al., *Chemically tailoring graphene oxides into fluorescent nanosheets for Fe3+ ion detection.* Carbon, 2012. **50**(6): p. 2147-2154.

43. Ciotta, E., et al., *Discriminating between Different Heavy Metal Ions with Fullerene-Derived Nanoparticles.* Sensors, 2018. **18**(5).

44. Ciotta, E., et al., *Sensitivity to Heavy-Metal Ions of Unfolded Fullerene Quantum Dots.* Sensors, 2017. **17**(11).

45. Bulushev, D.A., et al., *Copper on carbon materials: stabilization by nitrogen doping.* Journal of Materials Chemistry A, 2017. **5**(21): p. 10574-10583.

46. Sun, H.Z., et al., *A noble bimetal oxysulfide CuVOS catalyst for highly efficient catalytic reduction of 4-nitrophenol and organic dyes.* Rsc Advances, 2019. **9**(55): p. 31828-31839.

47. Liu, Y.Y., et al., *A simple route to prepare a Cu2O-CuO-GN nanohybrid for high-performance electrode materials.* Rsc Advances, 2017. **7**(20): p. 12027-12032.

48. Mondal, P., et al., *Enhanced catalytic performance by copper nanoparticle-graphene based composite.* Rsc Advances, 2013. **3**(16): p. 5615-5623.

49. Nie, H.B., et al., *Excellent Tribological Properties of Lower Reduced Graphene Oxide Content Copper Composite by Using a One-Step Reduction Molecular-Level Mixing Process.* Materials, 2018. **11**(4).

50. Babu, S.G., et al., *Influence of electron storing, transferring and shuttling assets of reduced graphene oxide at the interfacial copper doped TiO2 p-n heterojunction for increased hydrogen production.* Nanoscale, 2015. **7**(17): p. 7849-7857.

51. Biesinger, M.C., et al., *Resolving surface chemical states in XPS analysis of first row transition metals, oxides and hydroxides: Cr, Mn, Fe, Co and Ni.* Applied Surface Science, 2011. **257**(7): p. 2717-2730.

52. An, G.M., et al., *Low-temperature synthesis of Mn3O4 nanoparticles loaded on multi-walled carbon nanotubes and their application in electrochemical capacitors.* Nanotechnology, 2008. **19**(27): p. 75709-75709.

53. Suktha, P., et al., *Charge storage mechanisms of electrospun Mn3O4 nanofibres for high-performance supercapacitors.* Rsc Advances, 2017. **7**(16): p. 9958-9963.

54. Wang, L., et al., *Preparation of Mn3O4 nanoparticles at room condition for supercapacitor application.* Powder Technology, 2013. **235**: p. 76-81.

55. Biesinger, M.C., et al., *Resolving surface chemical states in XPS analysis of first row transition metals, oxides and hydroxides: Sc, Ti, V, Cu and Zn.* Applied Surface Science, 2010. **257**(3): p. 887-898.

56. Yang, H.M., J. Ouyang, and A.D. Tang, *Single step synthesis of high-purity CoO nanocrystals.* Journal of Physical Chemistry B, 2007. **111**(28): p. 8006-8013.

57. Huang, J., et al., *Highly selective production of heavy hydrocarbons over cobalt-graphene-silica nanocomposite catalysts.* Rsc Advances, 2017. **7**(53): p. 33441-33449.

58. Han, Y., et al., *Observing the Electrochemical Oxidation of Co Metal at the Solid/Liquid Interface Using Ambient Pressure X-ray Photoelectron Spectroscopy.* Journal of Physical Chemistry B, 2018. **122**(2): p. 666-671.

59. Langell, M.A., et al., *Valence-band electronic structure of Co3O4 epitaxy on CoO(100).* Physical Review B, 1999. **59**(7): p. 4791-4798.

60. Buchanan, R.M. and C.G. Pierpont, *Tautomeric Catecholate-Semiquinone Interconversion Via Metal-Ligand Electron-Transfer - Structural, Spectral, and Magnetic-Properties of*

(3,5-Di-Tert-Butylcatecholato)-(3,5-Di-Tert-Butylsemiquinone)(Bipyridyl)Cobalt(Iii), a Complex Containing Mixed-Valence Organic-Ligands. Journal of the American Chemical Society, 1980. **102**(15): p. 4951-4957.

61. Banerjee, S., J.T. Chen, and C.Z. Lu, *A new trinuclear mixed-valence Co(II)-Co(III) complex stabilized by a bis(salicylidene) based ligand.* Polyhedron, 2007. **26**(3): p. 686-694.

62. Zhang, K.L., et al., *Nitrogen-Doped Sponge Ni Fibers as Highly Efficient Electrocatalysts for Oxygen Evolution Reaction.* Nano-Micro Letters, 2019. **11**(1).

63. Zhao, Y., et al., *A new route for the electrodeposition of platinum-nickel alloy nanoparticles on multi-walled carbon nanotubes.* Electrochimica Acta, 2007. **52**(19): p. 5873-5878.

64. Z. Baig, O.M., M. Mustapha, A. Mumtaz, K. Munir, M. Sarfraz, *Investigation of Tip Sonication Effects on Structural Quality of Graphene Nanoplatelets (GNPs) for Superior Solvent Dispersion.* Ultrasonics Sonochemistry, 2018. **45**: p. 133-149.

65. F. Hennrich, R.K., K. Arnold, J. Stutz, S. Lebedkin, T. Koch, T. Schimmel, and M. Kappes, *The Mechanism of Cavity-Induced Scission of Single-Walled Carbon Nanotubes.* Journal of Chemistry B, 2007: p. 1932-1937.

66. D. O'Carroll, B.S., M. Krol, H. Boparai, C. Kocur, *Nanoscale Zero Valent Iron and Bimetallic Particles for Contaminated Site Remediation.* Advances in Water Resources, 2013. **51**: p. 104-122.

67. Morgan, W.S.a.J.J., *Aquatic Chemistry*. 1981, New York: John Wiley & Sons.

68. T. Bastami, M.E., *Synthesis of Manganese Oxide Nanocrystal by Ultrasonic Bath: Effect of External Magnetic Field.* Ultrasonics Sonochemistry, 2012. **19**: p. 830-840.

Chapter 4: Photoactivity of a Cell Membrane Specific Graphene Oxide Quantum Dot/Polyaniline/Mn_xO_y (GPM) via Formation of Hydroxyl Radical ($HO^{\cdot -}$) Formation as a Function of Mn^{n+} Oxidation State

Gustavo Chata[a], Forrest Nichols[a], Rene Mercado[a], Tufa Assafa[a], Shaowei Chen[a,*], Chad Saltikov[a,*]

Department of Chemistry and Biochemistry, University of California, 1156 High Street, Santa Cruz, California 95064, USA

Department of Microbiology and Environmental Toxicology, University of California, 1156 High Street, Santa Cruz, California 95064, USA

The biomedical relevance of graphene oxide quantum dots (GOQDs) as photoactive nanomaterial leading to reactive oxygen species (ROS) formation ultimately lead to bactericidal activity from functional moieties of the carbon-based nanostructures. The deposition metal oxide upon GOQD have recently exhibited enhanced photoactivity via chemically induced modification leading to nanocomposite design. In the present study Mn_xO_y nanoparticles were

synthesized hydrothermally and anchored with PANI onto GOQD. The various deposited Mn_xO_y nanoparticles exhibited photoactive oxidation states of Mn. The photoactivity of Mn (II) led to a drastic enhancement in hydroxyl radical ($HO^{\cdot-}$) concentration upon photoexcitation at 365 nm excitation. The Graphene Oxide/Polyaniline/Manganese Oxide (GPM) nanocomposites designed proved to have specific photoactivity towards *S. Epidermidis* and *E. coli* which was unrelated to ROS production. Emphasizing the relevance in nanocomposite-to-cell interface interaction for enhanced photodynamic activity.

4.1 Introduction

The continuous widespread application of antibiotics to gram-negative and gram-positive bacteria has led to the evolution of enzymatic resistance [1]. The application of modern antimicrobial drugs (AMD) specific to various extracellular and intracellular targets have been met with cellular modulation of antibiotic targets [2]. Prevalent antibiotic utilization has led to genomic expression of van casettes which lead to vancomycin resistance in gram-positive *Enterococci* and *S.Aureus* [3] specific to peptidoglycan binding sites on bacterial cell membranes. The production β-lactamase in *S.Aureus* and *E.coli* leads to

degradation of β-lactam derived antibiotics [3] [4]. Nanomaterials have readily been implemented as biomedical relevant alternative therapeutics to antibiotics. The enhanced cell membrane interaction of nanomaterial specific bacteria lead to lipid degradation, enzyme inactivation, DNA damage, and reactive oxygen species (ROS) formation evidently leading to cell death [5]. Metal oxide nanomaterials (MON) like ZnO, TiO_2, Cu_2O, Fe_xO_y, Ag_2O demonstrate the bactericidal effectiveness by modification of the size and shape of the designed nanostructures[6]. Although the efficacy of MON's originates from their valence band structures which allows for production of reactive oxygen species (ROS) which can be formed via metal oxide ionization [7]. The increased application of MONs a biotherapeutic agents stem from their available valence states, chemical inertness, and solubility.

While effective valence states of MONs have been readily identified for their inevitable aggregation and precipitation[8]. The ROS formation which lead to preferrable bactericidal activity can lead to inevitable cytotoxicity to mammalian cell lines [9]. Therefore, cellular specificity via ligand modification can lead to MON specificity towards bacterial organisms therein preventing aggregation

and enhancing bactericidal efficacy [10, 11]. Graphene oxide (GO) is a utilized oxidized carbon nanostructure utilized to enhance MONs solubility for antibacterial activity[12, 13]. The negatively charged oxygen moieties of GO provide sites for Van der Waals interactions with surface exposed positively charged metal sites from the metal oxide lattice[14-18]. The effective charge of the metal oxide along with the functionalized ligand on the surface of MONs will overall affect the measured zeta potential leading cell membrane specific activity [19]. The chemical inertness of MON incorporated GO based nanocomposites readily lead to MONs with a stabilized oxidation state leading to bactericidal activity based on ROS production or ROS independent membrane degradation[20].

The band-gap structure of MON based nanocomposite further enhance bactericidal activity at concentration below their minimal inhibitory concentrations (MIC)[21]. The design of a photoactive ZnO/GQD nanostructure by *Jiu et al.* was utilized to induce UV-induced ROS formation from the band structure of ZnO below the nanocomposites' MIC [22]. Similarly, *Cao et al*. demonstrated the enhanced photoactive antibacterial TiO_2/GS nanocomposite with a tunable bandgap as a function of reduced graphene oxide

deposition[23]. The design of RGO-CuO produced by *Kiani et al* demonstrates reconfiguration of the nanocomposites' band structure leading to charge transfer between the CuO and RGO[24]. The various GO based nanocomposites demonstrates the utility in enhancing the photoactivity of MON via chemical functionalization. Although careful examination of the ROS produced based on the oxidation state of the photoactive MON's is limited in literature. Specially since various of the effective photocatalysts exhibit a single oxidation state.

The various oxidation states exhibited by Mn_xO_y provide an effective system to evaluate the relationship between Mn oxidation state and ROS production leading to bactericidal activity. The accounted number of photoactive bactericidal GO/Mn_xO_y nanocomposites is limited in literature. Current work on Mn_xO_y nanomaterials solely focus on the bactericidal activity exhibited in the dark without focusing on the relevant relationship between Mn oxidation state and ROS production leading to bacterial cell death [25-27]. In this work we examine the effect of Mn_xO_y oxidation state on ROS production by utilizing polyaniline (PANI) to anchor Mn_xO_y nanoparticles with differing oxidation states to understand the effect in photocatalytic antibacterial activity. The

cytotoxicity and phototoxicity towards bacterial cells were then examined. The chemical structure of the graphene oxide/polyaniline/manganese oxide (GPM) nanocomposites were examined with TEM, XRD, and XPS to evaluate the oxidation state of the deposited Mn_xO_y on GPM. Electron Paramagnetic Resonance (EPR) was utilized to evaluate the specific ROS formed under light irradiation. The efficacy of photoactive MnO is found to produce a high concentration of $HO^{\cdot -}$ although the extent of its concentration does not relate with photoactivity. Thereby suggesting the relevance in nanocomposite-to-cell interaction from GPM-x nanocomposites.

4.2 Experimental Section

4.2.1 Chemicals

Aniline (99.8 %), Ammonium Persulfate (APS, 99.8%), Potassium Permanganate ($KMnO_4$, 99.0%), Polyvinylpyrrolidone (PVP, MW 3500), Ethylenediaminetetraacetic Acid Disodium Salt Dihydrate (EDTA-2Na, 99.0%), Tert-Butanol (TBA, 99.5%), Ethanol (EtOH, 95.0%), and Glutaraldehyde (25.0%) were all purchased from ACROS or Sigma Aldrich. Water was purified with a Barnstead Nanopure Water System (18 M Ω cm).

4.2.2 GOQD Synthesis

The synthesis of GOQD has been detailed previously. In brief, pitch carbon fiber (1 g) was immersed into a mixture of concentrated HNO_3 (40 mL) and H_2SO_4 (60 mL) in a round-bottom flask. After two hours of sonication, the carbon fibers were refluxed at 120 °C for 24 h. Once the solution was cooled to room temperature, its pH was adjusted to pH 7 with NaOH. The solution was left overnight to allow for salts to precipitate out of solution. The supernatant, which contained water-soluble GOQDs, was collected and transferred to a cellulose dialysis bag and placed in Nanopure water for several days to afford purified GOQD.

4.2.3 MnO Synthesis

90 mg $KMnO_4$ and 27 mg of polyvinylpyrrolidone were dissolved in 30 mL deionized (DI) water under stirring for 10 minutes which formed a homogeneous purple solution. The solution was transferred to a Teflon-lined steel autoclave, sealed, and maintained at 170 °C for 12 hours for a hydrothermal synthesis. After hydrothermal reaction, the precipitates were collected and washed with DI water and ethanol for several times[28].

4.2.4 MnOOH Synthesis

3 mL absolute ethanol was added into 47 mL aqueous solution of $KMnO_4$ (0.1 M) under stirring at room temperature. The mixture was then transferred into a Teflon-lined steel autoclave, sealed, and heated at 140 ^oC for 24 hours. After hydrothermal reaction, the precipitates were collected and washed with DI water[29].

4.2.5 MnO_2 Synthesis

0.608 g of $KMnO_4$ was dissolved in 70 mL distilled water for 30 min. Then, 1.27 mL HCl was added to the solution and stirred for 10 minutes. Solution was transferred to a 100 mL Teflon-lined stainless-steel autoclave and kept for 12 h 140 ^oC. Precipitates were collected and washed with water[30].

4.2.6 GOQD/PANI Synthesis

25 mg of GOQD were dissolved in 100 mL of DI water and ultrasonicated for 1 hour. A volume of 5 mL of aniline was added to the GOQD mixture after sonication. A solution of 5 mM APS was dissolved in a solution of 5.4 mM HCl which was later added to the GOQD solution and reacted for 10 minutes. Afterwards another 12 mL of aniline was added to the solution.

4.2.7 GOQD/PANI/Mn_xO_y Synthesis

25 mg of GOQD were dissolved in 100 mL of DI water and ultrasonicated for 1 hour. A volume of 12 mL of aniline was slowly added to a stirring GOQD suspension. Separately, 12.25 mg of APS was added to 10 mL of 5.4 mM HCl. The APS solution was then transferred to the stirring GOQD suspension which was reacted in an ice bath for 10 minutes. Then 25 mg of Mn_xO_y nanoparticles were dispersed in hydrochloric acid (1M, 50 mL) which was later added to the GOQD, aniline, and APS suspension. The reaction was stirred for 12 hours and dialyzed in Nanopure water for three days.

4.2.8 Characterization

The morphology and size of the samples were characterized by transmission electron microscopy measurements (TEM, Phillips CM 300 at 300 kV). UV-vis absorption spectra were acquired with a Perkin Elmer Lambda 35 UV-vis spectrophotometer, and photoluminescence measurements were conducted with a PTI fluorospectrophotometer. X-ray photoelectron spectra (XPS) were recorded with a PHI 5400/XPS instrument equipped with an Al K_α source operated at 350 W and 10^{-9} Torr. Time-resolved photoluminescence decay spectra was collected on a Horiba

QM-3304 instrument at the pulsed laser excitation of 335 nm in the time-correlated single-photon counting (TCSPC) mode

4.2.9 Antimicrobial Evaluation

E. coli cells were grown in Luria Broth (LB) agar in a 37 °C incubator. A single colony was selected and used to inoculate 3 mL of liquid LB and allowed to shake at 37 °C for 18 h. The resulting liquid was centrifuged at 5000 rpm for 5 min and resuspended in Nanopure water to an optical density of 0.1 at 600 nm. To determine the MIC, a 96-well plate was used to conduct a kinetic cell growth experiment in the dark at 37 °C. Each well was filled with a total volume of 200 µL with 30 µL of sterile LB, 10 µL of bacterial solution, and varied volumes of the GOQD samples prepared above. Sterile Nanopure water was used to bring the total volume in each well to 200 µL. Upon inoculation, the 96-well plate was placed in a Molecular Device VERSA max microplate reader, where the optical density (OD) was measured at 600 nm every minute and 30 seconds with intermittent shaking between each reading over a 24-hour incubation period. In photodynamic antibacterial assessments, 200 µL of *E. coli* (OD 0.1) was transferred to a 1 mL plastic centrifuge tube, into which 600 uL of 1 mg/mL the GOQD/PANI/Mn_xO_y samples and GOQD/PANI was added along with 200 µL of

sterilized Nanopure water. The centrifuge tubes containing the *E. coli* and nanoparticles were irradiated with UV photoirradiation (100 W, 1000-1500 lumen with a peak emission at 365 nm, Dongguan Hongke Lighting Co, China). After irradiating the sample, each centrifuge tube was diluted by 100 folds at each respective time point. From the diluted solution, 10 µL was distributed evenly on an LB agar plate utilizing sterilized glass beads. Upon dispersion of nanoparticle and *E. coli* suspension on the LB agar plate, the agar plates were placed in a 37 °C incubator.

4.2.9.a ROS Measurement

To quantify ROS concentrations, 63 µL of the GPM nanoparticles was mixed with 7 µL of 1 mol L^{-1} DMPO with the mixture of Nanopure H_2O and DMPO as a control. Then the solution was added to a capillary tube which was then inserted into a quartz EPR tube (Wilmad, 4 mm outer diameter). The tube was centered in the cavity resonator for data collection. Spectra were recorded at room temperature with a Bruker EMX EPR spectrometer operating at the X-band frequency (~9.4 GHz) using an ER 4122SHQE resonator (Bruker). The samples were subsequently irradiated of 10 min with 365 nm UV light to collect EPR spectra.

4.2.9.b Ellman's Reagent Assay

The intracellular oxidative capacity of GPM nanocomposites was measured after 365 nm excitation via oxidation of reduced glutathione. GPM-x nanocomposite and GP were solubilized in pH 7.4 0.1 M PBS buffer (300 µL at 1mg/mL) was added into 300 µL (13 mM GSH). The solution was irradiated at 365 nm excitation wavelength for 10 minutes then 300 µL of 5,5-dithio-bis-(2-nitrobenzoic acid) (100 µM DTNB) was added to GP or GPM-x with reduced glutathione solution. The absorbance at 412 nm of 2-nitro-5-thiobenzoic acid (TNB) was measured to assess the oxidation of reduced glutathione.

4.3 Results and Discussion

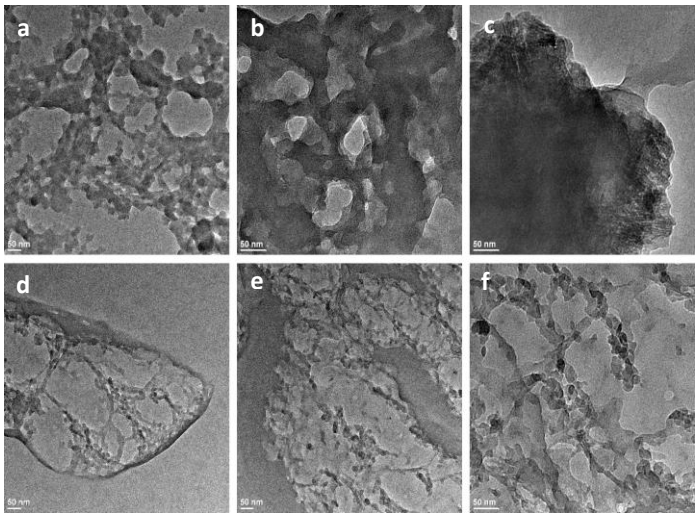

Figure 1: TEM Images of GPM 1 (a,b,c) and GPM-2 (d,e,f)

GPM-1 and GPM-2 (Fig. 1 a, b, d. e).

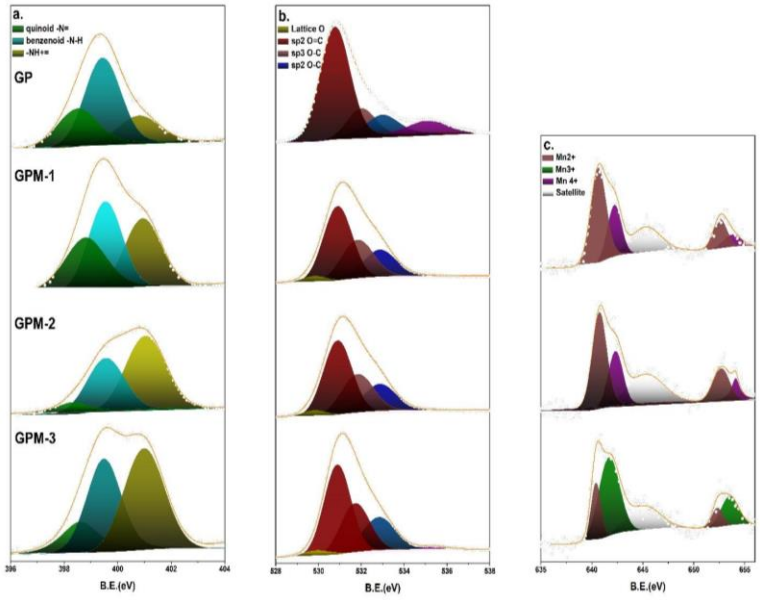

Figure 2: XPS of a) High resolution N1s, b) O1s, and c) Mn2p spectra for GP, GPM-1, GPM-2, and GPM-3

The lattice spacing from manganese oxide nanoparticles (Fig. S1) deposited on the surface of graphene oxide quantum dots (GOQD) via polyaniline (PANI) polymerization

The anchoring capacity of polyaniline (PANI) is exhibited by the metal oxide nanoparticles which are layered between a GOQD and PANI matrix for GPM-1 and GPM-2 samples (Fig. 1c, f). A porous GOQD frame enhances the exposed surface area from Mn_xO_y photocatalyst which lead to improved photoactivity for

for GPM-3. The deposited nanoparticles exhibit a large population of 0.17 nm, 0.20 nm, and 0.260 nm lattice fringes which corresponds with hexagonal wurtzite MnO with corresponding parameters: *$P6_3mc$,* a = b = 3.3718(2) Å, c = 5.3854 (7) Å[31] (Fig. S1). The high concentration of MnO nanoparticles demonstrate the efficiency of the electrostatic interaction of the negatively charged lattice oxygen of MnO and the positively charged quaternary amine from the polyaniline moiety. The high valency of Mn enables its oxidative activity thereby enabling highly oxidized Mn centers as active sites in the polymerization process[32, 33]. The polymerization process leads to a variety of Mn_xO_y whose various

Table 1: Summary of XPS Fitting Results (Atomic Percentage)

Sample	C	N	O	Mn		
				Mn2+	Mn3+	Mn4+
GPM-1	70.38%	5.86%	23.38%	0.246%	0%	0.159%
GPM-2	62.94%	5.79%	30.75%	0.345%	0%	0.175%
GPM-3	68.15%	5.66%	25.81%	0.092%	0.281%	0%
GP	64.01%	4.07%	31.95%	0%	0%	0%

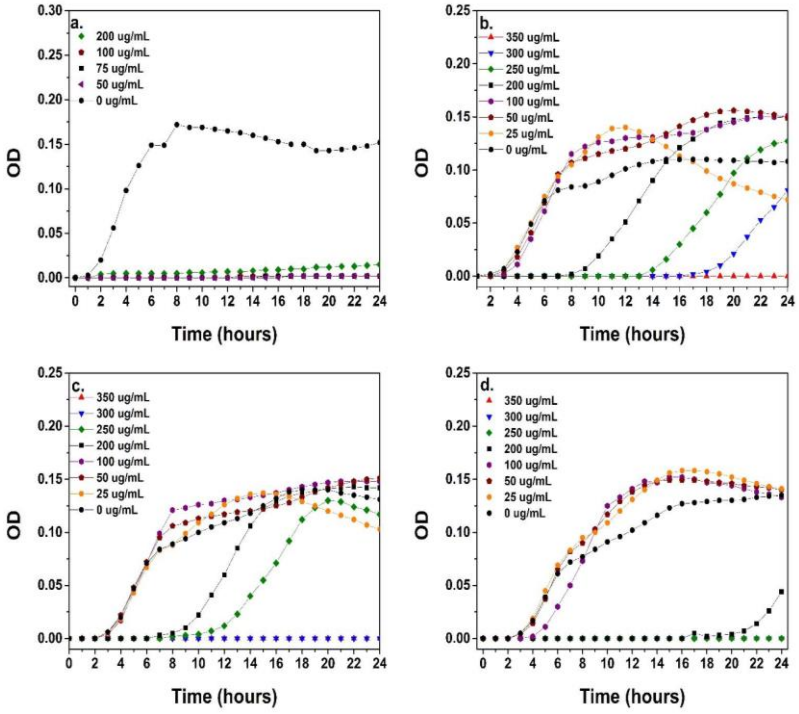

Figure 3: Minimal Inhibitory Concentration (MIC) measurements of *E.coli* in the dark with a) GP, b) GPM-1, c) GPM-2, and d) GPM-MnOOH

oxidation states were driven by the polyaniline polymerization. XRD diffraction patterns of various manganese oxides with varying oxidative states are testament to the polymerization mechanism of PANI (Fig. S2). While various Mn_xO_y diffraction patterns lead to the overall XRD signal measured, a critical contributor from the XRD pattern is originated from hexagonal MnO (mp-999539) and monoclinic MnOOH (mp-29159) for GPM-3 (Table S1). Although the diffraction pattern of hexagonal MnO and monoclinic is weak within the XRD pattern it does not

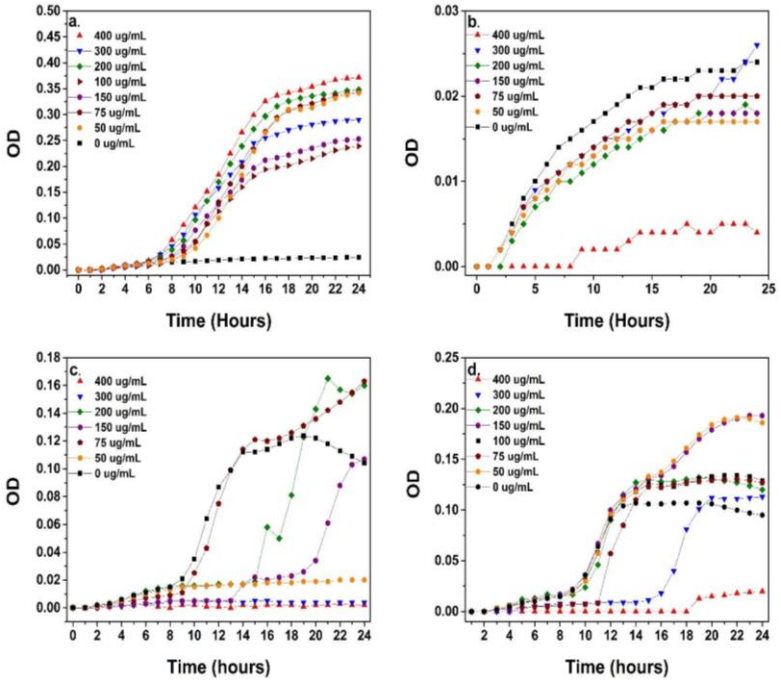

Figure 4: Minimal Inhibitory Concentration (MIC) measurements for *S. Epidermidis* in the dark with a) GP, b) GPM-1, c) GPM-2, and d) GPM-3

disregard its compelling presence on GPM-3. The broadness and intensity of XRD peaks are subject to the size and shape of deposited nanoparticles[34].

The diffraction pattern of wurtzite MnO is also present in GPM-1 and GPM-2 due to the polymerization of aniline with a Mn_xO_y of higher valency which readily leads to Mn^{2+} (Table S1) [35]. The polymerized aniline may further be oxidized by MnO_2 to Mn^{2+} although various MnO_2/polyaniline

composites synthesized independently exhibit high concentration of MnO_2 [36-41]. The presence of

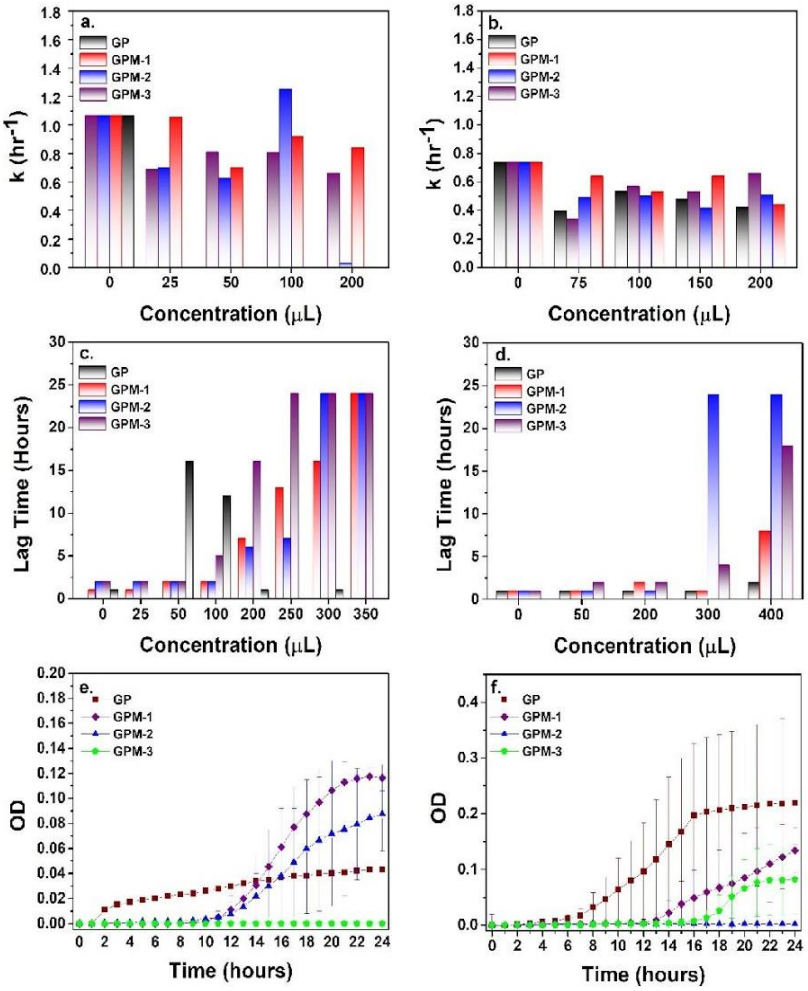

Figure 5: Growth Rate constants at respective concentrations of GP and GPM-x samples against a) *E. coli* and b) *S.Epidermidis*. Lag time measurements for GP and GPM-x samples against c) *E. coli* and d) *S. Epidermidis*.

various oxidation states of Mn_xO_y can be a function of the various intermediates from the oxidation of PANI

or ANI or the incomplete reduction of Mn precursors to the desired valency[42-45]. Since the Mn_xO_y can be reduced in the presence of PANI or ANI, the final oxidation state of the precursor could influence the Mn_xO_y present upon completion of the polymerization reaction. The absence of Mn^{4+} in GPM-3 demonstrates the Mn^{4+} was consumed during the oxidation of PANI and ANI, which occurs readily for Mn_xO_y systems where the oxidation state of Mn is 4+ (Fig. S2) [42] [41]. Although since the ANI polymerization is initialized by ammonium persulfate (APS) the reduction of Mn^{4+} to Mn^{2+} is not prevalent throughout the GPM-3 sample thereby leading to reduction of MnO_2 to other structures such as Mn_3O_4 and Mn_2O_3 (Table S1). The presence of MnO_2 in GPM-1 and GPM-2 demonstrates the incomplete reduction of Mn^{4+} possibly growth profile of *E.coli* at 250 µg/mL and f. *S.Epidermidis* at 300 µg/mL from lower percentage of MnO_2 present on the surface of each composite. Therefore, in GPM-1 and GPM-2 APS became the main oxidizer in the polymerization reaction which increased the Mn^{4+} concentration in both samples. The absorption profile of GPM samples can be attributed to the presence of GOQD and PANI structure (Fig. S3). The GOQD spectra demonstrates three absorption peaks at 232 nm, 260 nm, and 284 nm

which are related to the C=C from the sp^2 system of GOQD[46-48] (Table S2). The prominent 232 nm peak is present among the GP and GPM samples due to the existence of GOQD among all composite structures. In the GPM-2 composite the 232 nm to 218 nm peaks which can be attributed to the oxidation of the sp^2 structure to the acidic environment produced from the production of sulfates from APS reduction (Table S2). The emergence of peaks at 238 nm, 246 nm, and 254 nm correspond to the oxidation process[49, 50]. The GPM samples contain a peak at 270 nm which is due to the absorption of quinone, which is initiated from the oxidation of polyaniline from Mn_xO_y. The fluorescence emission spectra demonstrate the emergence of a sole emission peak which suggests the electron-hole recombination process measure via fluorescence occurs for a similar structure throughout all samples (Fig. S3). Although the emission intensity measured at 482 nm for GOQD, GPM-2, and GPM-3 are due to from the C-OH moiety from GOQD leading to a σ* - n electronic transition and near band edge emission from emeraldine base form of polyaniline (Table S3) [49, 51]. The enhanced photoluminescence at 482 nm for GPM-2 and GPM-3 can be related to the emission at 484 nm arising from GOQD and PANI. The emission spectra of GP and

GPM-1 is red-shifted to ~500 nm which can be attributed to a emeraldine base[52, 53].

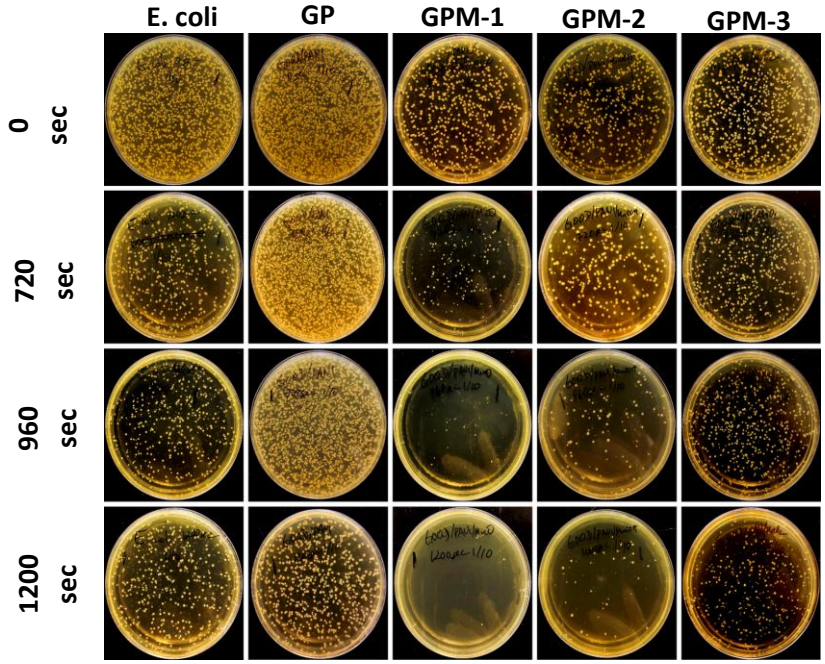

Figure 6: Photodynamic activity at excitation wavelength of 365 nm with *E. coli*, *E. coli* + GP, *E. coli* + GPM-1, *E.coli* + GPM-2, *E.coli* + GPM-3

The N1s spectra of GP and GPM samples demonstrate the presence of PANI throughout all samples due to deconvoluted peaks from N1s (Fig. 2a) related to various moieties in PANI which include quinoid -N=

(398.4 eV), benzenoid -N-H (399.4 eV), and quaternary ammonium -N=+ (400.8 eV) (Table S4) [54-56]. In contrast to GP, the GPM samples contain a higher atomic percentage of quaternary ammonium which could be attributed to the

interaction of PANI with Mn_xO_y during its polymerization (Table S5). The O1s spectra contains oxygen moieties from GOQD which include hydroxyl and carbonyl groups (Fig. 2b). In the O1s spectra the deconvoluted binding energy peaks are attributed to oxygen double bonded to sp^3 carbon (531 eV), oxygen single bonded to sp^3 carbon (532 eV), and oxygen single bonded to sp^2 carbon (533 eV) (Table S6)[49]. GPM samples contain a lattice oxygen peak at 530 eV with similar atomic percentage from dominant the presence of Mn_xO_y on the composite structure (Table S7) [57, 58]. The prevalent oxidation states from Mn on the surface of GPM samples can be measured from the Mn $2p^{3/2}$ position of the high-resolution Mn 2p spectra (Fig. 2c). The deconvoluted Mn 2p spectrum demonstrates the presence of two Mn oxidation states. Among all GPM samples the Mn 2p demonstrates a peak around 640.5 eV which can be attributed to Mn^{2+} (Table S8). The Mn $2p^{3/2}$ peak attributed to Mn^{2+} occurs at 640.61 eV and 640.40 eV for GPM-1 and GPM-3 respectively which can be attributed to MnO [59-62]. The spin orbital splitting for GPM-1 and GPM-3 is 12.06 eV and 11.85 eV respectively which accounts for the binding energy difference in Mn $2p^{3/2}$ and Mn $2p^{1/2}$ for MnO structure (Table S8) [59, 63, 64]. In GPM-2 the Mn$2p^{3/2}$ can also be attributed to Mn^{2+} regardless

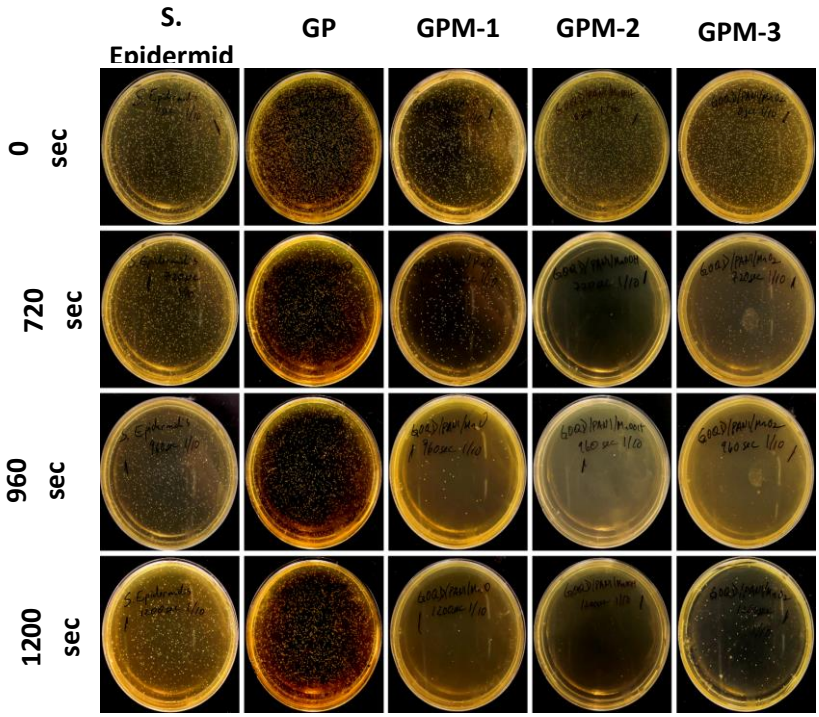

Figure 7: Photodynamic activity at 365 nm excitation of wavelength with *S. Epidermidis*, GP + *S. Epidermidis*, GPM-1 + *S. Epidermidis*, GPM-2 + *S. Epidermidis*, GPM-3 + *S. Epidermidis*

of an increase in the binding energy peak to 640.97 eV in contrast to GPM-1 and GPM-3[59-62, 65-67]. More specifically the Mn^{2+} signal can be attributed to MnO due to its binding energy difference between Mn $2p^{3/2}$ and Mn $2p^{1/2}$ which is 11.87 eV. Although the Mn^{2+} is prevalent among GPM samples, the secondary peak in the high resolved Mn $2p^{3/2}$ differs in GPM-3 in contrast to GPM-1 and GPM-2 (Fig. 2c). Within the GPM-1 and GPM-2 the secondary peak in the high resolved Mn 2p is defined at 642.16 eV and 642.59 eV

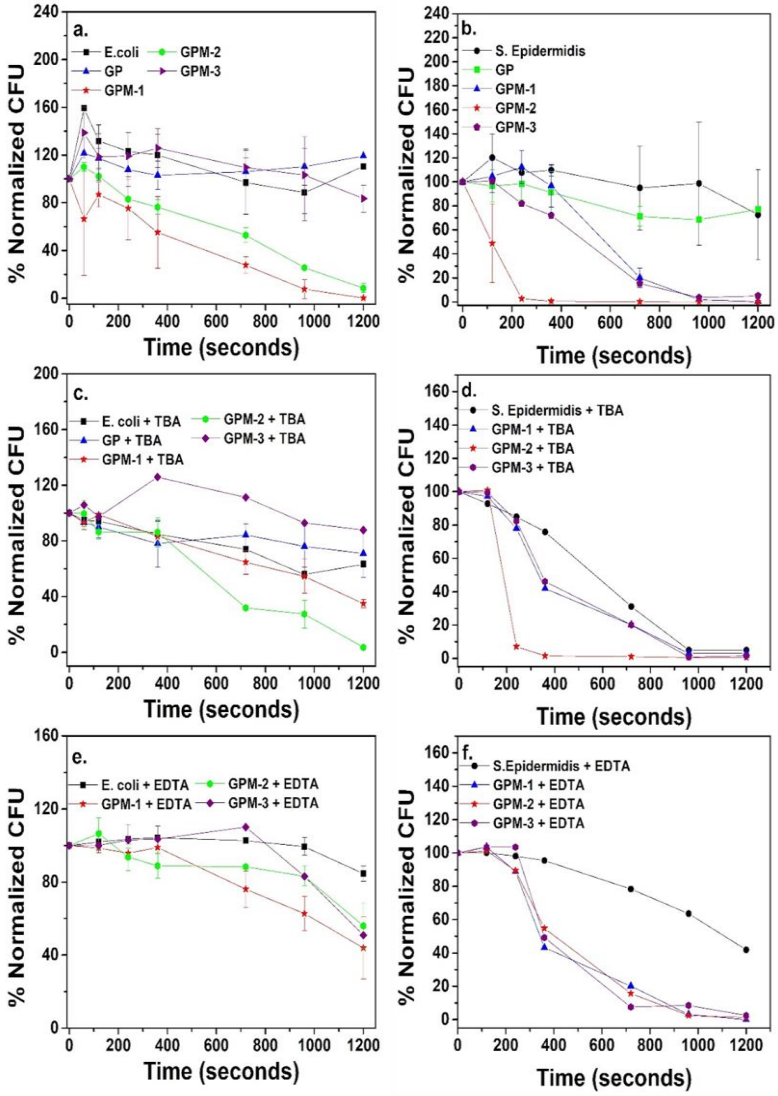

Figure 8: Photodynamic activity of GP and GPM-x under 365 nm exc. against a) *E.coli* , b) *S.Epidermis* , c) *E.coli* and TBA, d) *S.Epidermidis* and TBA, e) *E.coli* and EDTA, and f) *S.Epidermidis* and EDTA

with respective spin orbital splitting at 11.63 eV and 11.50 eV which can be attributed to MnO_2 (Table S8) [57, 60, 68-72].

The Mn $2p^{3/2}$ peak of GPM-3 occurs at 641.6 eV with a spin orbital splitting at 11.8 eV which accounts for the existence of Mn_2O_3 [60-62, 72-77]. Therefore, on the surface of GPM-1 and GPM-2 the Mn_xO_y structures of MnO and MnO_2 contribute extensively to the measured Mn 2p spectra (Fig. 2c). In contrast to GPM-3 where the dominant Mn_xO_y structures are MnO and Mn_2O_3. Analysis of the total atomic percentage of Mn per total C present through GPM samples ranges from 0.5 to 0.8% (Table S9). The oxidation states of Mn calculated from measured atomic percentage differ between GPM samples with a 65% Mn^{2+} and 35% Mn^{4+} present in GPM-1 and GPM-2 in contrast to 25% Mn^{2+} and 75% Mn^{3+} (Table S9). The measured valency of dominant Mn from GPM samples correlates with the XRD Mn_xO_y structures measured since hexagonal MnO is measured in all samples. Also, MnO_2 diffraction patterns are measured solely for GPM-1 and GPM-2 while GPM-3 clearly demonstrates the diffraction pattern for Mn_2O_3.

The minimal inhibitory concentrations of GP and GPM samples were assessed based on 96 well plate experiments. A gram-negative (*Escherichia coli*) and gram-positive (*Staphylococcus Epidermidis*) were utilized as model organisms for varying membrane interactions between the

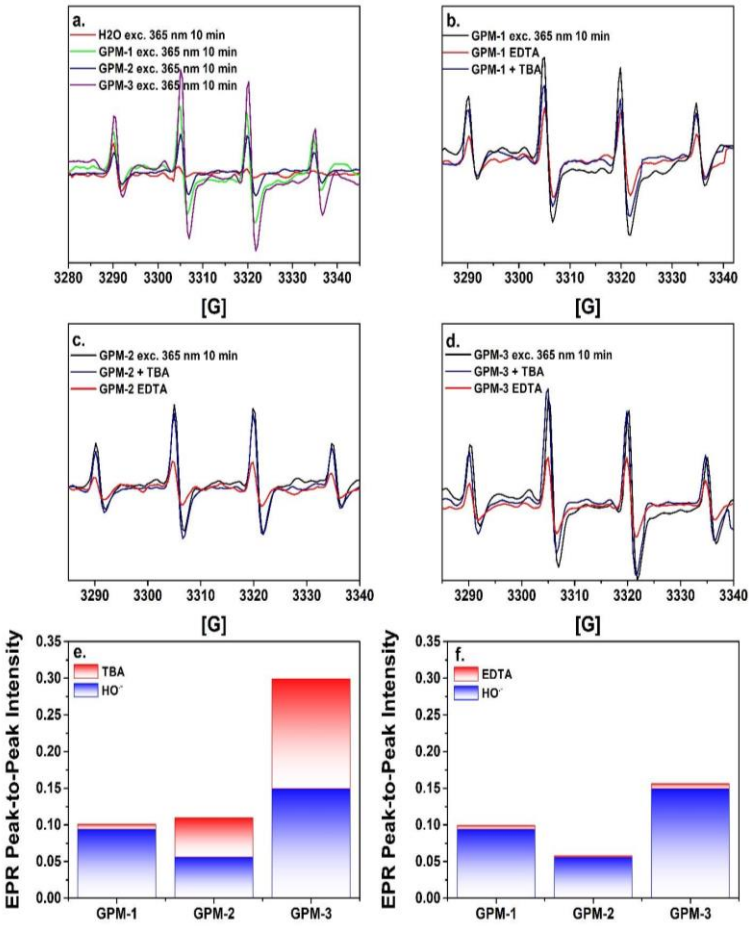

Figure 9: EPR hyperfine splitting pattern in the presence of DMPO after 10 minutes a) Photodynamic activity under 365 nm exc. with H_2O and GPM-x samples; b) GPM-1 with no radical scavenger, TBA, and EDTA c) GPM-2 with no radical scavenger, TBA, and EDTA; d) GPM-3 with no radical scavenger, TBA, and EDTA

nanocomposite and the cell membrane. The resting membrane potential for *E.coli* is measured between -75mV to -125 mV in contrast to the membrane potential of *S. Epidermidis* which is measured at -17.1 mV [78-80]. The MIC

of GP for *E. coli* was measured at 75 µg/mL while *S. Epidermidis* exhibited no bacterial growth (Fig. 3a and Fig. 4a). The variation in antimicrobial activity of GP towards *E.coli* versus *S. Epidermidis* can be ascribed to differences in nanoparticle to cell interface interaction [81, 82]. Since the antibacterial activity of graphene oxide is specific to nanoparticle size and oxidation state, variation in its surface potential can enhance cell membrane to sp^2 or oxygen defect interaction[83, 84]. The incorporation of Mn_xO_y into the GP structure increases the MIC for *E. coli* by varying the inhibitory activity to a higher concentration for the GPM-1, GPM-2, and GPM-3 to a concentration of 350 µg/mL, 300 µg/mL, and 250 µg/mL respectively (Fig.3 b,c,d). In contrast to *E. coli*, the inhibitory activity of GPM is enhanced in contrast to GP for *S. Epidermidis* organism by exhibiting an MIC at 400 µg/mL for GPM-1 and GPM-3 and 300 µg/mL for GPM-2 (Fig. 4 b,c,d). Since Mn^{2+} is soluble in aqueous media, the GPM samples with high concentrations of Mn (II) can lead to Mn (II) diffusion therein affecting the growth rate of *E. coli* and *S. Epidermidis*. In the case of *E. coli* the Mn (II), Mn(III), and Mn(IV) within GP cause an enhancement in the growth rate in contrast to GP alone (Fig. 3). Specifically GPM-1 and GPM-2 demonstrate a decreased antibacterial efficiency in *E.*

coli inhibition, the diminished inhibitory action can be attributed to an increase in Mn(II) (Table S4). A decreased inhibitory activity due to Mn_xO_y within GP for *E.coli* can be attributed to the resistance and accumulation of Mn(II) in *E. coli K-12* strain[85]. The aqueous Mn(II) can react on the surface of *E.coli* therein effecting the bacteria's growth rate[86]. The presence of specific Mn(II)-importers such as Nramp-type transporters and ATP-binding casettes (ABC) importers are utilized to incorporate into metabolically active enzymes such superoxide dismutase, ribonuclotide reductase, and FosB [87]. The GPM-1 and GPM-2 which contain the highest concentration of Mn(II) calculated from high resolution XPS of Mn 2p (Fig. 2c) demonstrate an increased MIC (Table S4) in contrast to GPM-3 which contain an elevated concentration of Mn(III). The enhanced inhibitory activity of GPM-3 can be attributed to the presence of Mn_2O_3 on its surface. The inhibition of *E.coli* has been categorized in zone of inhibition (ZOI) experiments were polyvinylpyrrolidone (PVP) and cetyl trimethyl ammonium bromide (CTAB) displayed similar inhibition against *E. coli* [88]. Uncapped Mn_2O_3 is known to display inhibitory activity towards both gram-negative and gram-positive bacteria [89].

The antibacterial activity of GPM towards *S. Epidermidis* is enhanced in contrast to GP (Figure 4). The inhibitory activity of GPM-1 and GPM-3 is enhanced with an MIC over 400 μg/mL and an MIC of 300 μg/mL for GPM-2 (Table S4). Similar to *Staphylococcus Aureus* the gram-positive bacteria *S. Epidermidis* possesses a Mn^{2+} specific binding protein known as mntABC transporter which allows intercellular uptake[90]. The Mn specific superoxide dismutase (SOD) enzymes of gram-negative bacteria such as *S. Aureus* and *S. Epidermidis* known as sodM and sodA are influential in resistance to reactive oxygen species [91, 92]. Therefore, intercellular uptake of Mn^{2+} leads to a diminished antibacterial activity which is observed for highly concentrated Mn^{2+} GPM-1(Fig. 3 a). The antibacterial activity of GPM-2 towards *S. Epidermidis* is not solely attributed to the intracellular ionic incorporation of Mn(II). The incorporation of Mn_xO_y for GPM-2 is potentially enhancing the cell-to-nanocomposite interaction this can be attributed to the dissimilarities in inhibitory activity measured for GPM-1 and GPM-2. Assessment of the atomic concentration of Mn to carbon of GPM-2 from high resolution XPS (Table S9) demonstrates GPM-2 contains 0.82% Mn/C in contrast to 0.5% Mn/C of GPM-1. The slightly negative membrane

potential of *S. Epidermidis* benefits from an increase in the Mn (II) and Mn (IV) population of GPM-2. The attenuation of GPM's activity as a function of membrane potential is further supported by the inhibitory activity of GPM-3 which contains a population of Mn (II) and Mn (III) on GPM surface (Table S9). Therefore, the decreased valency of Mn or decrease in higher valent Mn concentration diminishes the inhibitory activity of GPM against *S. Epidermidis*.

The efficiency of Mn_xO_y on the inhibitory activity on the cell membrane of bacteria of GPM nanocomposites is exhibited by the decrease in growth rate constant exhibited among all GPM samples for both *E. coli* and *S. Epidermidis* (Fig.5 a,b). An increase lag time (t_l) as a function of GPM further verifies the effect of Mn_xO_y for both *E. coli* and *S. Epidermidis* (Fig. 5 c,d). Growth curves measured at constant concentrations demonstrate the specificity of GPM-x samples to bacterium cell wall at high nanocomposite concentrations (Fig. 5 e,f). The GPM-3 nanocomposite demonstrates complete inhibition of *E. coli* growth at 250 µg/mL (Fig. 5e) while GPM-2 completely inhibits *S. Epidermidis* growth at 300 µg/mL (Fig. 5f). The small deviation in antibacterial activity concentration of *S.epidermidis* and *E.coli* suggests Mn valency does not

strongly contribute to bacterial growth inhibition. Furthermore the bactericidal activity displayed amongst all GPM-x nanocomposites at high concentrations indicate the antagonistic influence of Mn_xO_y on the growth of *E.coli* and *S.Epidermidis*. Although the high MIC's tabulated for GPM-x demonstrates the necessity of a high concentration of Mn_xO_y is required to inhibit bacterial growth in the dark.

To assess the bactericidal activity of GP and GPM-x samples upon photoirradiation a low nanocomposite concentration of 6 μg/mL was utilized against bacteria. The photoexcitation of GPM-x samples at 365 nm excitation demonstrates an enhanced bactericidal activity of *E. coli* for GPM-1 at 1200 sec (Fig. 6). In contrast the photoexcitation of GPM-2 leads to enhanced bactericidal activity of *S. Epidermidis* at 360 sec (Fig. 7). The source of photodynamic activity was assessed by utilizing radical scavengers of tert-butyl alcohol (TBA) and ethylenediaminetetraacetic acid (EDTA) which are specific for hydroxyl radicals (HO^{-}) and holes (h^{+})[93-99]. The TBA leads to loss of photodynamic activity against *E. coli* for GPM-1 only (Fig. 8c). The photodynamic activity for GP, GPM-2, and GPM-3 remains unchanged due to inactivity of photocatalyst in presence of TBA against *S. Epidermidis* (Fig. 8d). The radical scavenger

activity of EDTA influences scavenging activity of GPM-1 and GPM-2 by increasing the measured Colony Forming Units (CFU) of *E. coli* (Fig. 8e). Similarly, the TBA scavenger was utilized in photodynamic activity against *S. Epidermidis* but only slightly diminishes the bactericidal activity of GPM-2 by increasing the CFU measured at 240 seconds from 0.63% population of CFU to 7.03% (Table S12). The application of EDTA to photodynamic activity of GPM-2 against *S. Epidermidis* demonstrates quenching of GPM-2 by increasing the of time of cell death (TOC) of all CFU from 720 seconds to over 1200 seconds (Fig. 7f) Photodynamic activity among other GPM-x nanocomposites is not affected by the presence of EDTA. The effective quenching capacity of EDTA towards GPM-1 and GPM-2 is demonstrated clearly in the photodynamic activity measured for *E. coli*. Furthermore, EDTA is effective in quenching photodynamic activity of GPM-2 against *S. Epidermidis* which distinguishes holes as critical active site in the production of reactive oxygen species (ROS) inducing cell death. Electron paramagnetic resonance (EPR) was utilized to determine the reactive oxygen species (ROS) responsible for bactericidal activity for *S. Epidermidis* and *E. coli* (Fig. 8). The irradiation of 365 nm of GPM-x and H_2O control demonstrate the enhancement of a

1:2:2:1 hyperfine structure $a_N = a_H = 14.9$ G which is attributed to a DMPO-OH adduct specifically related to hydroxyl radical ($HO^{\cdot -}$) production [100-102] (Fig. 8a). The $HO^{\cdot -}$ production is enhanced for all GPM-x samples in comparison to the H_2O control. The EPR peak-to-peak intensity demonstrates the concentration of $HO^{\cdot -}$ is produced more extensively in the GPM-x samples in the corresponding order GPM-3 > GPM-1 > GPM-2. Application of TBA to GPM-x in EPR experiments demonstrates quenching solely for GPM-1 (Fig. 8 b) but does not lead to an appreciable decrease in $HO^{\cdot -}$ production. The EDTA radical scavengers for photo-generated holes from Mn_xO_y enhanced scavenging activity in comparison to TBA (Fig. 8 c,d,e,f). The photodynamic activity of GPM-x samples The EPR peak-to-peak intensity producing the quartet splitting pattern of EPR correlates with reduced glutathione (GSH) oxidation experiments with 5,5′-dithiobis(2-nitrobenzoic acid) (DTNB) which is readily utilized to measure antimicrobial activity with ROS

production [84, 103, 104]. The intracellular concentration of reduced thiols (GSH) influences the intracellular concentration of H_2O_2 via disulfide bond formation (GSSG) from H_2O_2 oxidation (GSH GSSG + $2e^-$ + $2H^+$) (O_2 + $2e^-$ + $2H^+$ H_2O_2) [84, 105]. The intercellular concentration of H_2O_2 is

readily controlled by both gram-negative and gram-positive bacteria since superoxide formation ($O_2^{\cdot -}$) and free Fe^{2+} concentration can lead to highly oxidative $HO^{\cdot -}$ effectively leading to cell death [106, 107]. The GPM-x nanocomposites were photo-irradiated for 10 minutes with a 365 nm excitation wavelength LED to assess the extent of GSH oxidation in presence of photo-active GPM-x nanocomposites. The loss of reduced glutathione is effective in the presence of Mn_xO_y on GP in the following order GPM-3 > GPM-1 > GPM-2 (Fig. S4). The decrease in glutathione from ROS production correlates strongly with the DMPO-OH adduct measured for EPR among all GPM-x samples (Fig. 9 a). Unlike the ROS dependent oxidation of glutathione, the photodynamic activity of GPM-x samples do not correlate with the production of $HO^{\cdot -}$ formation measured from EPR (Fig. 9 a,b). The GPM-1 and GPM-2 demonstrate enhanced photodynamic activity for *E. coli* and *S. Epidermidis* respectively which contains a high concentration of Mn^{4+} as measured from high resolution Mn 2p XPS (Table S9).

The XRD pattern of GPM-1 and GPM-2 exhibits MnO_2 nanostructures which are not exhibited in the GPM-3 sample (Fig. S2). As previously discussed the Mn (II) specificity cell transporter of both *S. Epidermidis* and *E. coli* can produce

enzymatically specific active sites for Mn(II) active nanocomposite attachment. Similarly to Mn(II) specificity, Mn(III) transferrin receptors TfR are utilized to endocytose Mn(III) intracellularly into bacterial organisms utilizing enzymatic Mn to inhibit H_2O_2 formation [108]. The redox cycling of Mn(II) and Mn(III) leads to an enhancement in scavenging activity of $O_2^{\cdot-}$ [109]. In contrast to lower valent Mn, the production or consumption of Mn(IV) is prevalent in redox active reaction of bacteria like *Bacillus* and *Alteromonas putrefaciens* [110-113]. The oxidation of Mn(II) to Mn(IV) is known to lead to biomineralization into MnO_2 [111, 112] which portrays the biomineralization of Mn(IV) in higher valent redox active bacteria. Therefore, upon cell-to-nanocomposite interaction of GPM-1 and GPM-2, the Mn (IV) maintain its MnO_2 structure while Mn (II) ionization can be intercellularly metabolized. The Mn oxidation state of GPM-3 can both be internalized and metabolized by both gram-negative and gram-positive model organisms utilized. Also the Mn (II) and Mn (III) enzymatic sequestration in superoxide dismutase can lead to a decrease in intracellular $O_2^{\cdot-}$ which leads to a diminished bactericidal activity. The Mn-valent specific metabolism of gram-negative and gram-positive bacteria therein lead to a diminished photoactive

activity of GPM-3 regardless of the extent of $HO^{\cdot -}$ measured under photoexcitation (Fig. 9a). Furthermore suggesting the DMPO-OH adduct attributed to $HO^{\cdot -}$ may also be a source of $O_2^{\cdot -}$ which could occur upon protonation of $O_2^{\cdot -}$ into H_2O_2 and UV irradiation to $HO^{\cdot -}$ [114]. Due to the enzymatic reactivity of SOD the $O_2^{\cdot -}$ would lead to H_2O_2 which is less lethal to bacterial organisms. Also the cellular machinery of *S. Epidermidis* and *E. coli* would inevitably lead to the metabolization of Mn^{2+} and Mn^{3+} with (SOD) therein enhancing the cellular scavenging activity.

The protonation of $O_2^{\cdot -}$ to H_2O_2 ultimately affects the $HO^{\cdot -}$ hyperfine splitting pattern due to its radical formation from UV-irradiated H_2O_2 [114]. The high concentration of photoactive Mn(II) and Mn(III) can lead to oxidation to corresponding higher Mn(III) and Mn(IV) valency under UV excitation as proposed by *Yosdhia et al.* from GPM-3 [115]. The extensive production of $HO^{\cdot -}$ on GPM-3 correlates well with plausible $O_2^{\cdot -}$ formation due to its extent of production arising from Mn (III) Mn_xO_y sites [116]. In the photoexcited states superoxide formation would yield from Mn (III) active sites via a one electron O_2 reduction reaction to produce $O_2^{\cdot -}$ leading to Mn (IV) production. The photoactivated Mn(IV) could be reduced to Mn(III) in the formation of $HO^{\cdot -}$ as

measured from EPR spectra and antibacterial experiments [117, 118]. In contrast to GPM-3 were Mn (II) and Mn (III) active sites are dominant, the Mn(II) and Mn(IV) are prevalent amongst the GPM-1 and GPM-2 nanocomposites (Fig. 2c). Similar to GPM-3, Mn(II) active sites, the Mn(II) can indeed lead to an increased valency of Mn(III) upon photoirradiation which could react with O_2 to form $O_2^{\cdot-}$ leading to Mn(IV). The newly formed Mn (IV) could lead to $HO^{\cdot-}$ therein recharging Mn to Mn (III) or could lead to a separate photonic process observed for MnO_2 under UV-excitation. The Mn (IV), specifically MnO_2 structures, are readily reduced to Mn(III) upon UV irradiation as determined by *Marafatto et al.* [119]. The variation in DMPO-OH adduct measured from GPM-1 and GPM-2 can be attributed to the separate reduction mechanisms of Mn (IV) upon photo-excitation [119]. The rate of $HO^{\cdot-}$ production from the photogenerated Mn (IV) is replenished by H_2O to $HO^{\cdot-}$ for GPM-1 while GPM-2 experiences photoreduction of Mn (IV) to Mn (III). The fitted XRD of GPM-1 and GPM-2 support the preferred $HO^{\cdot-}$ dependent formation replenishment of Mn(IV) to Mn(III) based on measured experimental bandgaps (Table S1).

The XRD of GPM-1 is fitted to MnO, Mn_3O_4, and MnO_2 with measured experimental bandgaps at 1.58 eV, 2.5 eV, and 1.25 eV respectively (Table S1). Unlike GPM-1, the fitted XRD pattern of GPM-2 solely contains experimental bandgaps measured for MnO and MnO_2 at 1.58 eV and 0.617 eV respectively (Table S1). Since photoexcitation of GPM-x nanostructures is conducted at an energy of 3.33 eV, all Mn_xO_y nanostructures would induce electron hole separation which could evidently react with H_2O leading to production of $HO^{\cdot-}$ (Fig. 9a). The absence of measured experimental bandgaps of Mn_3O_4 from GPM-2 underpins its predominant photoactive Mn (IV) reduction events to Mn (III). In other words, the Mn (II) and Mn (III) forms of Mn_3O_4 could not be photoexcited to Mn (III) and Mn (IV) respectively which would lead to $O_2^{\cdot-}$ and $HO^{\cdot-}$ based on the reduction potentials asserted from its bandgap. The ROS producing Mn_xO_y photoactive sites may not solely be activated during its photoexcitation process. The fluorescence emission of GPM-2 is most quenched amongst all GPM-x samples which suggests it is most effective in electron-hole separation originating from GP photoemission. Such quenching mechanism can be attributed to the assisted photoreduction of Mn (IV) to Mn (III) originating from the excited electron

from GP's conduction band. A quenched emission agrees with Mn (IV) to Mn (III) photoreduction since the excited electron originating from the valence band of GP cannot recombine leading to its diminished photoluminescence. The sole specificity of GPM-1 and GPM-2 to *E. coli* and *S. Epidermidis* suggests an enhancement in the nanocomposite-to-cell interaction since the high production of ROS measured from the DMPO-OH adduct of GPM-3 does not correlate with photogenerated cell death. The close cellular interaction with the nanocomposites is further supported by the measured oxidation of reduced glutathione from the Ellman's Reagent Assay (Fig. S4) where its oxidation relates strongly with EPR measured ROS production (GPM-3 > GPM-1 > GPM -2).

Furthermore, extensive oxidation based on carbon single molecules is supported by the leading photocatalytic degradation of methylene blue dye (MBD) Mn_xO_y. The high extent of MBD oxidation attributed to MnO_2 is not solely dependent on ROS formation arising from its band structure but also its spontaneous reduction coupled to MBD oxidation[120, 121]. The spontaneity of reaction is defined by proton concentration therein yielding a higher concentration of Mn^{2+} from MnO_2 [122]. Therefore, attributing

enhanced photodynamic activity of GPM-1 and GPM-3 to intercellular ROS formation via oxidation of relevant redox active enzymes responsible for spontaneous ATP burrowed within its plasma membrane. Ubiquinone (Coenzyme Q) contains redox active quinones relevant to the oxidation succinate to fumarate leading ultimately to electron transport in cytochrome b which eventually leads to ATP production from mitochondrial proton influx[123]. Therefore, intercellular concentration of MnO_2 would facilitate cell death via mitochondrial inactivation due to the metabolic relevance of ubiquinone and the high proton mitochondrial membrane concentration.

The present study demonstrates the antibacterial efficacy of a Mn_xO_y nanostructures with enhanced water solubility due to PANI anchoring onto GOQD. The photodynamic activity of GPM-1 and GPM-2 is specific to *E. coli* and *S. Epidermidis,* respectively. While the low antibacterial activity (MIC > 200 µg/mL) of GPM-x nanocomposites for both model organisms further supports the relevance of photoactive Mn_xO_y nanostructure utilized at low concentrations (6 µg/mL). The inhibition of bacterial growth at high nanocomposite concentration portrays the bactericidal activity of Mn_xO_y nanostructure. Structural

information of GPM-x structure demonstrates the presence of lower Mn valency in GPM-3 in contrast to the higher Mn valency of GPM-1 and GPM-2. Fluorescence emission demonstrates enhanced quenching of GPM-2 which correlates with a decrease in ROS production as measured from EPR. Interestingly ROS production does not correlate with the observed bactericidal activity which determines the role of solution free ROS of nanocomposite materials. The bactericidal specificity of GPM-1 and GPM-2 suggests cell membrane-to-nanocomposite interaction as a leading role to enhanced photodynamic activity.

4.4 Conclusion

In this study the enhanced ROS production relates with a lower Mn valent GPM-x nanostructure. While Mn (II), Mn (III), and Mn (IV) all prove to be photoactive sites for ROS production while a lower valent Mn leads to more ROS dependent redox pathways. The interaction of GP and Mn_xO_y leads to the UV driven photoreduction from GP to Mn (IV) leading to Mn (III). Therein decreasing the amount of ROS produced from GPM-2 due to electron transfer from the photo-excited electrons from the conduction band of GP to the photoactive Mn_xO_y. Therefore, the efficiency of an ROS-dependent photoreduction pathway from Mn (IV) to Mn (III)

determines the efficacy of photoactive GPM-x nanocomposites. While the lower valent Mn is critical in ROS production, a higher concentration of Mn (II) and Mn (IV) leads to enhanced photodynamic activity with *S. Epidermidis* and *E. coli* due to enhanced nano-composite-to-cell membrane interaction. The production of bacterial membrane specific GPM nanocomposites showcases the relevance in utilizing the favorable physical characteristics of relevant nanomaterials in producing an optimal photocatalyst. The application of PANI as a Mn_xO_y nano-anchor to GOQD can lead to further refinement of more effective photocatalyst for antibacterial activity.

4.5 Supporting Information

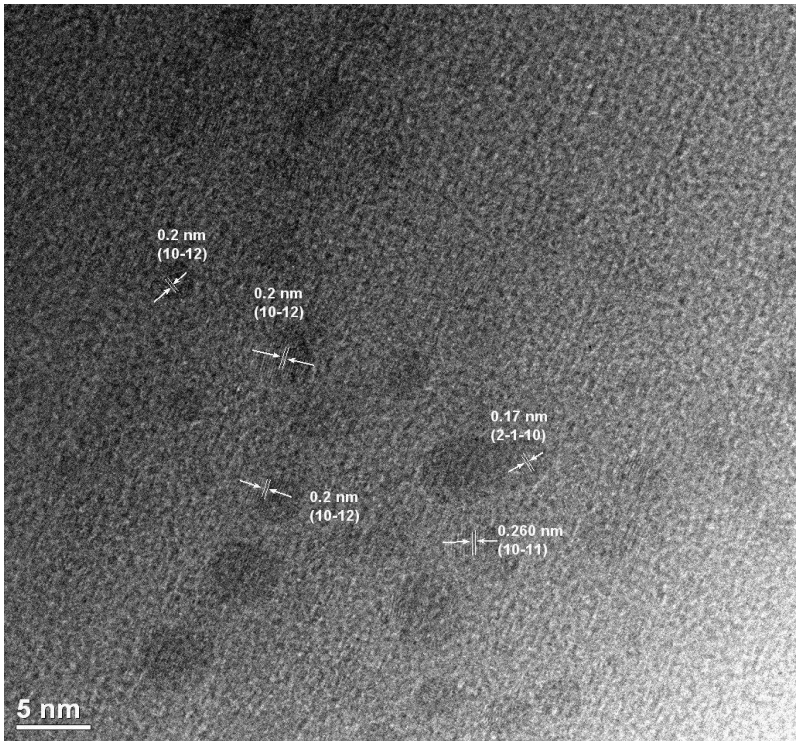

Figure S1: TEM of GPM-3

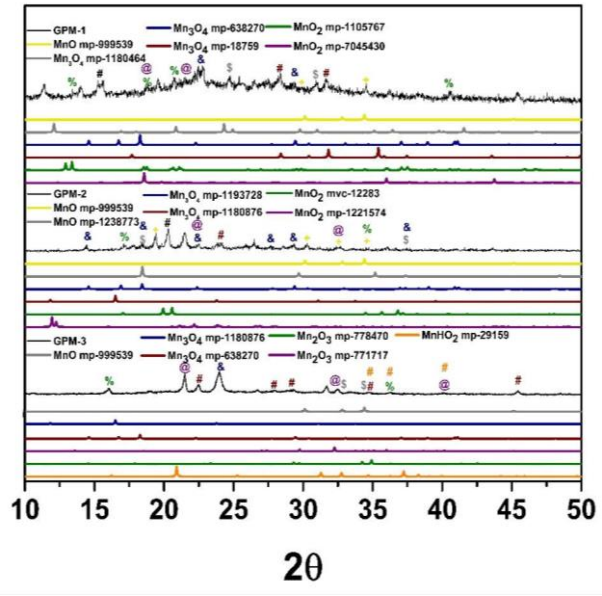

Figure S2: XRD of GPM-1, GPM-2, and GPM-3

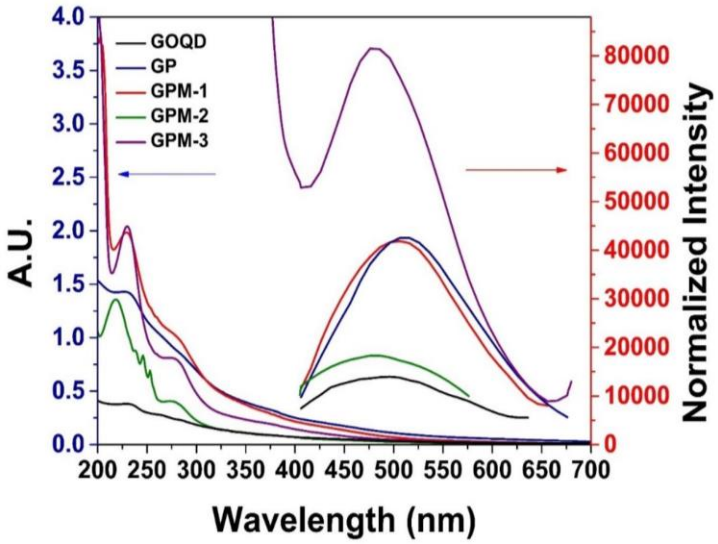

Figure S3: UV-VIS and Normalized Photoluminescence Spectra of GOQD, GP, GPM-1, GPM-2, and GPM-3

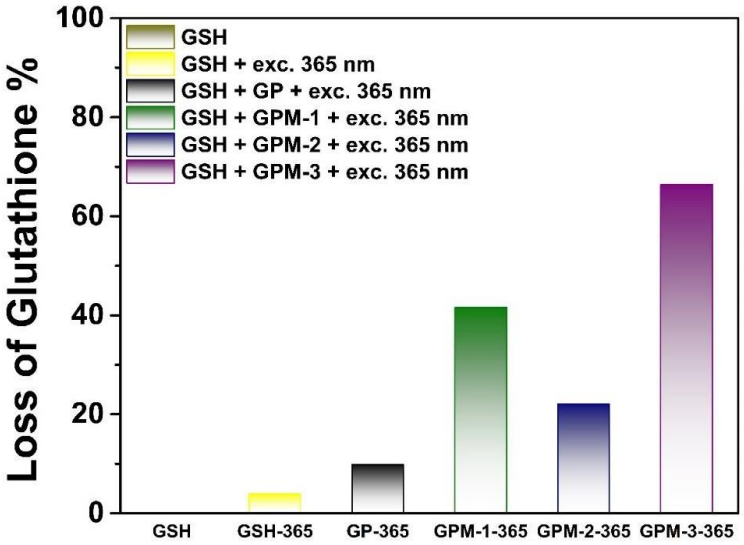

Figure S4: Loss of reduced glutathione measured from absorption of 462 nm of the 2-nitro-5-thiobenzoic acid (TNB) reaction with reduced glutathione (GSH) after UV-irradiation in the absence of catalysis, with GP, and with GPM-x samples.

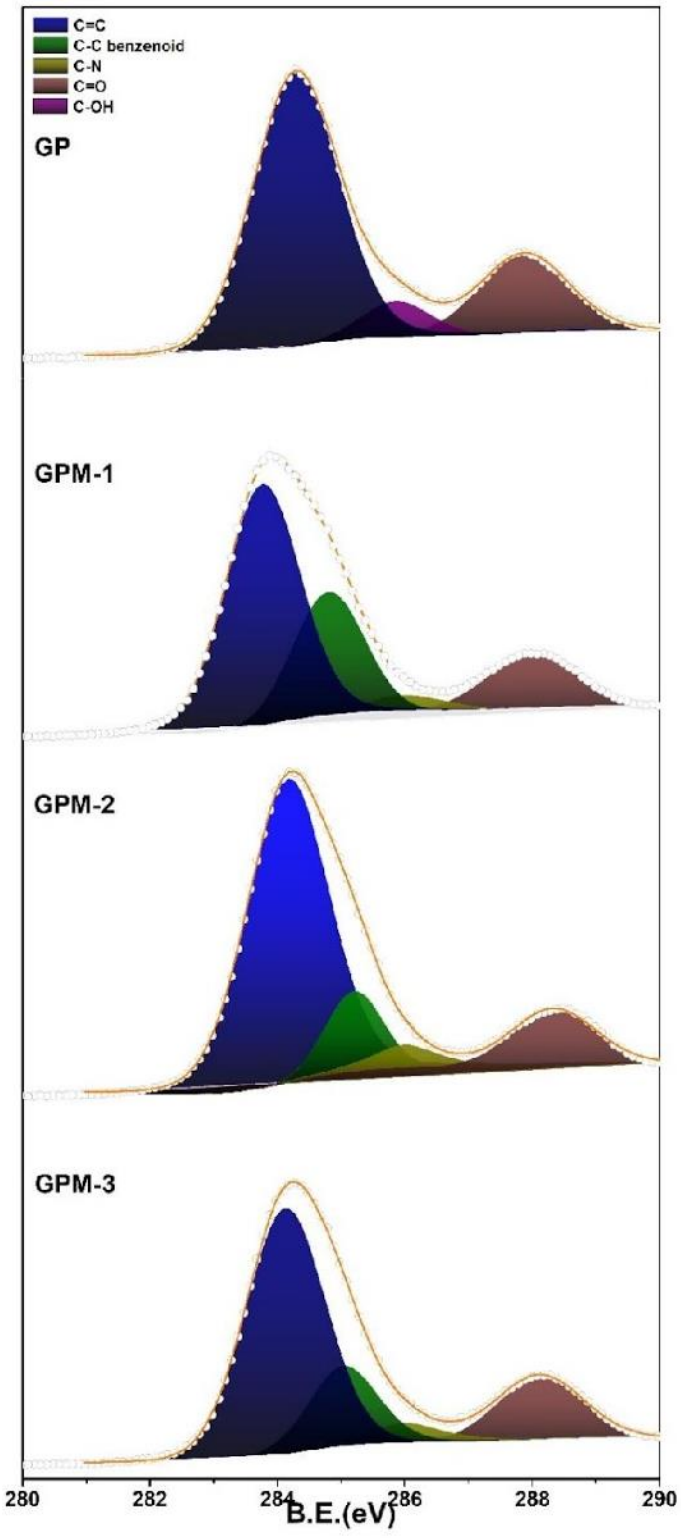

Figure S5: Deconvoluted high resolved C1s XPS of GP, GPM-1, GPM-2, and GPM-3

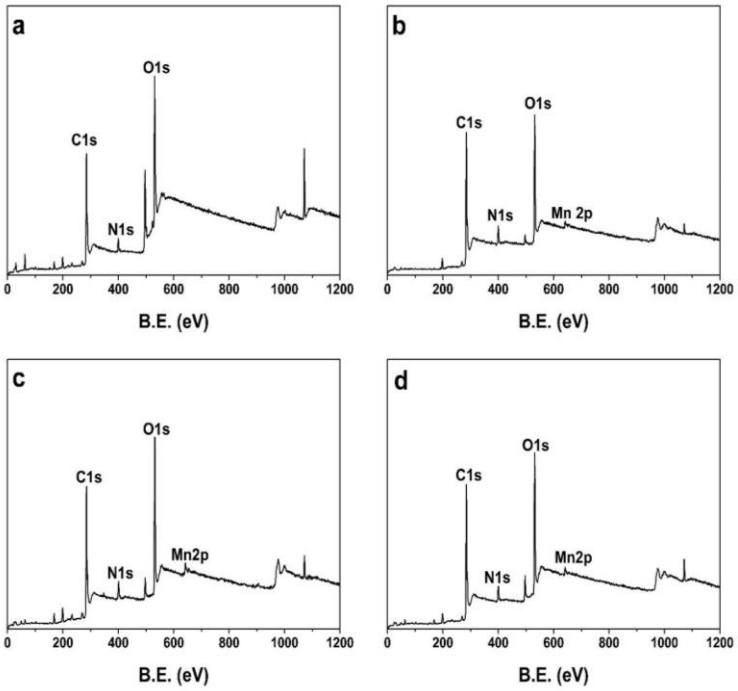

Figure S6: XPS survey scan of a) GP, b) GPM-1, c) GPM-2, and d) GPM-3

Table S1: Manganese Oxide structures identified from raw XPS data of GPM-x nanocomposites with their respective crystal system and calculated or measured bangap.

GPM-1 standards	Metal Oxide Structure	GPM-2 standards	Metal Oxide Structure	GPM-3 standards	Metal Oxide Structure
mp-999539	MnO	mp-999539	MnO	mp-1238899	MnO
mp-1180464	Mn_3O_4	mp-1238773	MnO	mp-999539	MnO
mp-638270	Mn_3O_4	mp-1193728	Mn_3O_4	mp-1180876	Mn_3O_4
mp-18759	Mn_3O_4	mp-1180876	Mn_3O_4	mp-638270	Mn_3O_4
mp-1105767	MnO_2	mvc-12283	MnO_2	mp-778470	Mn_2O_3
mp-7045430	MnO_2	-	-	mp-771717	Mn_2O_3
-	-	-	-	mp-29159	$MnHO_2$

Table S2: Absorption peaks measured from UV-VIS with corresponding functional groups attributed to their electronic transitions.

Samples	Abs. λ_1 (nm)	Abs. Origin	Abs. λ_2 (nm)	Abs. Origin	Abs. λ_3 (nm)	Abs. Origin
GOQD	232	π - π^* of C=C from GOQD	260	π - π^* of C=C from GOQD	284	π - π^* of C=C from GOQD
GP	230	π - π^* of C=C from GOQD	379	Phenanzine absorption		
GPM-1	230	π - π^* of C=C from GOQD	279	π - π^* of substituted quinones		
GPM-2	218	π - π^* of C=C from GOQD	238	π - π^* of C=C from GOQD	246	π - π^* of C=C from GOQD
GPM-3	230	π - π^* of C=C from GOQD	279	π - π^* of substituted quinones		

Table S3: Emission wavelength measured from excitation of GPM-x and GP at 350 nm.

Samples	Em λ_1 (nm)	Em. Origin
GOQD	482	C-OH σ^* - n from GOQD
GP	508	Doped -N=
GPM-1	503	M^{n+}-N-phen
GPM-2	482	C-OH σ^* - n from GOQD and $\pi - \pi^*$ from PANI
GPM-3	482	C-OH σ^* - n from GOQD

Table S4: Average binding energies measured from deconvoluted high resolved N1s spectra with their corresponding standard deviations.

Sample	N1s quinoid amine (avg.)	N1s benzenoid amine (avg.)	N1s quarternary amine (avg.)
GP	398.36	399.36	400.82
GPM-1	398.8	399.55	400.90
GPM-2	398.33	399.56	400.97
GPM-3	398.66	399.81	400.98
Sample	**N1s quinoid amine (avg.) Intensity**	**N1s benzenoid amine (avg.) Intensity**	**N1s quarternary amine (avg.)**
GP	5480.11	15164.34	4423.51
GPM-1	10468.90	12731.97	14866.87
GPM-2	2986.01	13042.52	23713.96
GPM-3	7797.59	12291.98	16990.14

Table S5: Percentage composition of quinoid, benzenoid, and quaternary amine measured from high resolved N1s spectra.

Sample	%Lattice Quinoid Amine/Total Nitrogen	% Benzenoid Amine/Total Nitrogen	% Quaternary Amine/ Total Nitrogen
GP	21.86	60.49	17.65
GPM-1	27.50	33.45	39.05
GPM-2	7.51	32.82	56.67
GPM-3	21.03	33.15	45.82

Table S6: Average binding energies measured from deconvoluted high resolved O1s spectra with their corresponding standard deviations.

Sample	O1s Lattice Oxygen (avg.)	O1s O=C (avg.)	O1s O-C(avg.)	O1s O-C sp^2 (avg.)	O1s H_2O (avg.)
GP	-	530.81	531.63	532.76	535.19
GPM-1	529.8	530.93	531.92	533.02	-
GPM-2	529.8	530.89	531.88	533.05	-
GPM-3	529.85	530.81	531.63	532.76	535.19
Sample	O1s Lattice Oxygen (avg.) Intensity	O1s O=C (avg.) Intensity	O1s O-C(avg.) Intensity	O1s O-C sp^2 (avg.) Intensity	O1s H_2O (avg.) Intensity
GP	-	226364.8	51009.3	43023.1	38851.69
GPM-1	8474.99	122275.2	81103.31	49314.32	-
GPM-2	13614.43	163349.6	108316.9	77796.15	-
GPM-3	10864.75	127145	86778.4	63502.9	4993.94

Table S7: Percentage composition of oxygen from metal oxide lattice, double bonded oxygen to sp^2 carbon, single bonded oxygen to sp^3 carbon, single bonded oxygen to sp^2 carbon, and oxygen measured from water adsorbed from high resolved O1s spectra.

Sample	**%Lattice O/Total Oxygen**	**% O=C/Total Oxygen**	**% O-C/ Total Oxygen**	**%O-C sp^2 / Total Oxygen**	**%H_2O /Total Carbon**
GP	-	70.65	15.92	13.43	-
GPM-1	3.25	46.82	31.05	18.88	-
GPM-2	3.75	44.99	29.83	21.43	-
GPM-3	3.70	43.35	29.59	21.65	1.70

Table S8: Average binding energies measured from deconvoluted high resolved Mn 2p spectra with their corresponding standard deviations. Intensity of deconvoluted Mn 2 p spectra measured from GPM nanocomposites.

Sample	**Mn $2p^{3/2}$ (avg.) (pos. 1)**	**Mn $2p^{1/2}$ (avg.) (pos. 1)**	**ΔB.E.**	**Mn $2p^{3/2}$ (avg.) (pos. 2)**	**Mn $2p^{1/2}$ (avg.) (pos. 2)**	**ΔB.E.**
GPM-1	640.61	652.67	12.06	642.16	653.80	11.64
GPM-2	640.97	652.84	11.87	642.59	654.13	11.55
GPM-3	640.40	652.21	11.82	641.62	653.41	11.80
Sample	**Mn $2p^{3/2}$ Int. (avg.) (pos. 1)**	**Mn $2p^{1/2}$ Int. (avg.) (pos. 1)**	-	**Mn $2p^{3/2}$ Int. (avg.) (pos. 2)**	**Mn $2p^{1/2}$ Int. (avg.) (pos. 2)**	-
GPM-1	8985.17	2810.43	-	5370.34	1100	-
GPM-2	13250	500	-	6750	2250	-
GPM-3	3461.10	1064.36	-	10355.67	1064.36	-

Table S9: Percentage of total manganese per carbon, ratio of lattice oxygen to total manganese atomic composition, percentage of manganese oxidation states to total manganese measured from XPS.

Sample	%Mn/C (Total C)	Lattice O/Mn	% Mn^{2+}/Mn (Total Mn)	% Mn^{3+}/Mn (Total Mn)	% Mn^{4+}/Mn (Total Mn)
GPM-1	0.54	2.04	64.58	-	35.42
GPM-2	0.82	2.34	66.36	-	33.64
GPM-3	0.55	2.59	24.76	75.24	-

4.6 References

1. Arias, C.A. and B.E. Murray, *Antibiotic-resistant bugs in the 21st century--a clinical super-challenge.* N Engl J Med, 2009. **360**(5): p. 439-43.
2. Egorov, A.M., M.M. Ulyashova, and M.Y. Rubtsova, *Bacterial Enzymes and Antibiotic Resistance.* Acta Naturae, 2018. **10**(4): p. 33-48.
3. Schaenzer, A.J. and G.D. Wright, *Antibiotic Resistance by Enzymatic Modification of Antibiotic Targets.* Trends Mol Med, 2020. **26**(8): p. 768-782.
4. Kennedy, K. and P. Collignon, *Colonisation with Escherichia coli resistant to "critically important" antibiotics: a high risk*

for international travellers. European Journal of Clinical Microbiology & Infectious Diseases, 2010. **29**(12): p. 1501-1506.

5. Gupta, A., et al., *Combatting antibiotic-resistant bacteria using nanomaterials.* Chemical Society Reviews, 2019. **48**(2): p. 415-427.
6. McNamara, K.T.S.A.M., *Nanoparticles in Biomedical Applications.* Advances in Physics, 2017. **2**: p. 54-88.
7. Zhang, H.Y., et al., *Use of Metal Oxide Nanoparticle Band Gap To Develop a Predictive Paradigm for Oxidative Stress and Acute Pulmonary Inflammation.* Acs Nano, 2012. **6**(5): p. 4349-4368.
8. Hotze, E.M., T. Phenrat, and G.V. Lowry, *Nanoparticle Aggregation: Challenges to Understanding Transport and Reactivity in the Environment.* Journal of Environmental Quality, 2010. **39**(6): p. 1909-1924.
9. Sengul, A.B. and E. Asmatulu, *Toxicity of metal and metal oxide nanoparticles: a review.* Environmental Chemistry Letters, 2020. **18**(5): p. 1659-1683.
10. Khan, M., et al., *Enhanced Antimicrobial Activity of Biofunctionalized Zirconia Nanoparticles.* Acs Omega, 2020. **5**(4): p. 1987-1996.

11. Wang, L.L., C. Hu, and L.Q. Shao, *The antimicrobial activity of nanoparticles: present situation and prospects for the future.* International Journal of Nanomedicine, 2017. **12**: p. 1227-1249.

12. Rojas-Andrade M., N.T., Mistler W., Armas J., Lu J., Roseman G., Hollingsworth W., Nichols F., Millhauser G., Ayzner A., Saltikov C., Chen S., *Antimicrobial Activity of Graphene Oxide Quantum Dots: Impacts of Chemical Reduction* Nanoscale Adv., 2020. **2**: p. 1074-1083.

13. He, P.C., S., *Vertically Oriented Graphene Nanosheets for Electrochemical Energy Storage.* 8, 2021: p. 783-797.

14. El-Shafai, N.M., et al., *Graphene oxide-metal oxide nanocomposites: fabrication, characterization and removal of cationic rhodamine B dye.* Rsc Advances, 2018. **8**(24): p. 13323-13332.

15. Liu, J.L., et al., *Antimicrobial Activity of Zinc Oxide-Graphene Quantum Dot Nanocomposites: Enhanced Adsorption on Bacterial Cells by Cationic Capping Polymers.* Acs Sustainable Chemistry & Engineering, 2019. **7**(19): p. 16264-16273.

16. El-Shafai, N., et al., *Graphene oxide decorated with zinc oxide nanoflower, silver and titanium dioxide nanoparticles: fabrication, characterization, DNA interaction, and*

antibacterial activity. Rsc Advances, 2019. **9**(7): p. 3704-3714.

17. Wang, Y.W., et al., *Superior antibacterial activity of zinc oxide/graphene oxide composites originating from high zinc concentration localized around bacteria.* ACS Appl Mater Interfaces, 2014. **6**(4): p. 2791-8.

18. Nichols, F.L., J.; Mercado, R.; Rojas-Andrade, M.; Ning, S.; Azhar, Z.; Sandhu, J.; Cazares, R.; Saltikov, C.; Chen, S., *Antibacterial Activity of Nitrogen-Doped Carbon Dots Enhanced by Atomic Dispersion of Copper.* Langmuir 2020. **36**: p. 11629-111636.

19. Liu, J.S., J.; Wang, Y.; Li, J.; Liu, H.; Wang, A.; Hui, A.; Chen, S. , *Antimicrobial Activity of Zinc Oxide -Graphene Quantum Dot Nanocomposites: Enhanced Adsorption on Bacterial Cells by Cationic Capping Polymers.* ACS Sustain Chem Eng, 2019. **7**: p. 16264-16273.

20. Rojas-Andrade, M.D., et al., *Antibacterial mechanisms of graphene-based composite nanomaterials.* Nanoscale, 2017. **9**(3): p. 994-1006.

21. Liu, J.C., W.; Wang, Y.; Fan, X.; Shen, J.; Liu, H.; Wang, A.; Hui, A.; Nichols, F.; Chen, S., *Cobalt-Doped Zinc Oxide Nanoparticles-MoS2 Nanosheet Composites as Broad-*

Spectrum Bactericidal Agents. ACS Appl Nanomaterials, 2021.

22. Liu, J., et al., *Photo-enhanced antibacterial activity of ZnO/graphene quantum dot nanocomposites.* Nanoscale, 2017. **10**(1): p. 158-166.
23. Cao, B.C., et al., *High antibacterial activity of ultrafine TiO2/graphene sheets nanocomposites under visible light irradiation.* Materials Letters, 2013. **93**: p. 349-352.
24. Kiani, F., et al., *Effect of graphene oxide nanosheets on visible light-assisted antibacterial activity of vertically-aligned copper oxide nanowire arrays.* Journal of Colloid and Interface Science, 2018. **521**: p. 119-131.
25. Kamran, U., et al., *Biogenic synthesis, characterization and investigation of photocatalytic and antimicrobial activity of manganese nanoparticles synthesized from Cinnamomum verum bark extract.* Journal of Molecular Structure, 2019. **1179**: p. 532-539.
26. Alimohammadi, F., et al., *Antimicrobial Properties of 2D MnO2 and MoS2 Nanomaterials Vertically Aligned on Graphene Materials and Ti3C2 MXene.* Langmuir, 2018. **34**(24): p. 7192-7200.
27. Haneefa, M.M., M. Jayandran, and V. Balasubramanian, *Green Synthesis Characterization and Antimicrobial Activity*

Evaluation of Manganese Oxide Nanoparticles and Comparative Studies with Salicylalchitosan Functionalized Nanoform. Asian Journal of Pharmaceutics, 2017. **11**(1): p. 65-74.

28. Wang, S.T., et al., *Conversion-Type MnO Nanorods as a Surprisingly Stable Anode Framework for Sodium-Ion Batteries.* Advanced Functional Materials, 2020. **30**(19).

29. Gao, T., et al., *Microstructures, Surface Properties, and Topotactic Transitions of Manganite Nanorods.* Inorganic Chemistry, 2009. **48**(13): p. 6242-6250.

30. Zeraati, A.S., M. Arjmand, and U. Sundararaj, *Silver Nanowire/MnO2 Nanowire Hybrid Polymer Nanocomposites: Materials with High Dielectric Permittivity and Low Dielectric Loss (vol 9, pg 14328, 2017).* Acs Applied Materials & Interfaces, 2017. **9**(37): p. 32412-32412.

31. Nam, K.M., et al., *New Crystal Structure: Synthesis and Characterization of Hexagonal Wurtzite MnO.* Journal of the American Chemical Society, 2012. **134**(20): p. 8392-8395.

32. Hekmat, F., S. Shahrokhian, and N. Taghavinia, *Ultralight Flexible Asymmetric Supercapacitors Based On Manganese Dioxide-Polyaniline Nanocomposite and Reduced Graphene Oxide Electrodes Directly Deposited on Foldable Cellulose*

Papers. Journal of Physical Chemistry C, 2018. **122**(48): p. 27156-27168.

33. Jaidev, et al., *Polyaniline-MnO2 nanotube hybrid nanocomposite as supercapacitor electrode material in acidic electrolyte.* Journal of Materials Chemistry, 2011. **21**(44): p. 17601-17605.

34. Holder, C.F. and R.E. Schaak, *Tutorial on Powder X-ray Diffraction for Characterizing Nanoscale Materials.* Acs Nano, 2019. **13**(7): p. 7359-7365.

35. Liu, Z.S., et al., *Use of manganese dioxide as oxidant in polymerization of aniline on carbon black for supercapacitor performance.* High Performance Polymers, 2016. **28**(10): p. 1105-1113.

36. He, Y., et al., *MnO2/polyaniline hybrid nanostructures on carbon cloth for supercapacitor electrodes.* Journal of Solid State Electrochemistry, 2016. **20**(5): p. 1459-1467.

37. Han, G.Q., et al., *MnO2 Nanorods Intercalating Graphene Oxide/Polyaniline Ternary Composites for Robust High-Performance Supercapacitors.* Scientific Reports, 2014. **4**.

38. Mu, B., et al., *Glycol assisted synthesis of graphene- MnO2-polyaniline ternary composites for high performance supercapacitor electrodes.* Physical Chemistry Chemical Physics, 2014. **16**(17): p. 7872-7880.

39. Misnon, I.I. and R. Jose, *Synthesis and electrochemical evaluation of the PANI/delta-MnO2 electrode for high performing asymmetric supercapacitors.* New Journal of Chemistry, 2017. **41**(14): p. 6574-6584.

40. Li, H.L., et al., *MnO2 nanoflake/polyaniline nanorod hybrid nanostructures on graphene paper for high-performance flexible supercapacitor electrodes.* Journal of Materials Chemistry A, 2015. **3**(33): p. 17165-17171.

41. Han, J., et al., *Reactive template strategy for fabrication of MnO2/polyaniline coaxial nanocables and their catalytic application in the oxidative decolorization of rhodamine B.* Journal of Materials Chemistry A, 2013. **1**(42): p. 13197-13202.

42. Wang, J.Z., C; Jin, D; Xie, K.; Wei, B., *Synthesis of Ultralong MnO/C Coaxial Nanowires as Freestanding Anodes for High-Performance Lithium Ion Batteries.* Journal of Materials Chemistry A, 2015. **3**: p. 13699-13705.

43. Ortaboy, S.A., J.; Rossi, F.; Bertoni G.; Salviati G.; Carraro C.; Maboudian R., *MnOx-decorated carbonized porous silicon nanowire electrodes for high performance supercapacitors.* Energy & Environmental Science, 2017. **10**: p. 1505-1516.

44. Kang, L., et al., *A new strategy for synthesis of hierarchical MnO2-Mn3O4 nanocomposite via reduction-induced*

exfoliation of MnO2 nanowires and its application in high-performance asymmetric supercapacitor. Composites Part B-Engineering, 2019. **178**.

45. Duay, J.S., S.; Gui Z.; Gillette E.; Lee S., *Self-Limiting Electrodeposition of Hierarchical MnO2 and M(OH)2/MnO2 Nanofibril/Nanowires: Mechanism and Supercapacitor Properties.* ACS Nano, 2013. **2**: p. 1200-1214.
46. Luo, D.C., et al., *Evaluation Criteria for Reduced Graphene Oxide.* Journal of Physical Chemistry C, 2011. **115**(23): p. 11327-11335.
47. Saxena, S., et al., *Investigation of structural and electronic properties of graphene oxide.* Applied Physics Letters, 2011. **99**(1).
48. Zhang, J.L., et al., *Reduction of graphene oxide via L-ascorbic acid.* Chemical Communications, 2010. **46**(7): p. 1112-1114.
49. Li, M., et al., *Fingerprinting photoluminescence of functional groups in graphene oxide.* Journal of Materials Chemistry, 2012. **22**(44): p. 23374-23379.
50. Sapurina, I. and J. Stejskal, *The mechanism of the oxidative polymerization of aniline and the formation of supramolecular polyaniline structures.* Polymer International, 2008. **57**(12): p. 1295-1325.

51. Bubb, D.M., et al., *Observation of persistent photoconductivity in conducting polyaniline thin films.* Applied Physics a-Materials Science & Processing, 2005. **81**(1): p. 119-125.

52. Liu, Y.F., et al., *Room temperature synthesis of pH-switchable polyaniline quantum dots as a turn-on fluorescent probe for acidic biotarget labeling.* Nanoscale, 2018. **10**(14): p. 6660-6670.

53. Zhang, J.L., et al., *Enhanced conductivity and fluorescence of polyaniline doped with Eu3+, Tb3+, and Y3+ ions.* Journal of Applied Polymer Science, 2012. **125**(4): p. 2494-2501.

54. Patil, S.H., et al., *To form layer by layer composite film in view of its application as supercapacitor electrode by exploiting the techniques of thin films formation just around the corner.* Electrochimica Acta, 2018. **265**: p. 556-568.

55. Ahuja, P., et al., *Hierarchically Grown NiO-Decorated Polyaniline-Reduced Graphene Oxide Composite for Ultrafast Sunlight-Driven Photocatalysis.* Acs Omega, 2018. **3**(7): p. 7846-7855.

56. Li, Y.Q., et al., *Green Synthesis of Free Standing Cellulose/Graphene Oxide/Polyaniline Aerogel Electrode for High-Performance Flexible All-Solid-State Supercapacitors.* Nanomaterials, 2020. **10**(8).

57. Chen, S., et al., *Thermally driven phase transition of manganese oxide on carbon cloth for enhancing the performance of flexible all-solid-state zinc-air batteries.* Journal of Materials Chemistry A, 2019. **7**(34): p. 19719-19727.

58. Li, X.T., et al., *Oxygen Vacancies Induced by Transition Metal Doping in gamma-MnO2 for Highly Efficient Ozone Decomposition.* Environmental Science & Technology, 2018. **52**(21): p. 12685-12696.

59. Biesinger, M.C., et al., *Resolving surface chemical states in XPS analysis of first row transition metals, oxides and hydroxides: Cr, Mn, Fe, Co and Ni.* Applied Surface Science, 2011. **257**(7): p. 2717-2730.

60. Ianhez-Pereira, C., et al., *The interplay between Mn valence and the optical response of ZnMnO thin films.* Applied Physics a-Materials Science & Processing, 2020. **126**(5).

61. Xie, Y.J., et al., *A highly effective Ni-modified MnOx catalyst for total oxidation of propane: the promotional role of nickel oxide.* Rsc Advances, 2016. **6**(55): p. 50228-50237.

62. Liu, L.Z., et al., *Self-molten-polymerization synthesis of highly defected Mn/Sm binary oxides with mesoporous structures for efficient removal of toluene and*

chlorobenzene. Inorganic Chemistry Frontiers, 2019. **6**(5): p. 1158-1169.

63. Li, M., et al., *High-performance asymmetric supercapacitors based on monodisperse MnO nanocrystals with high energy densities.* Nanoscale, 2018. **10**(34): p. 15926-15931.

64. Ramadan, M., et al., *3D Interconnected Binder-Free Electrospun MnO@C Nanofibers for Supercapacitor Devices.* Scientific Reports, 2018. **8**.

65. Pang, Y.M., Z.; Wang, H.; Wang, X.; Linkov, V.; Wang, R., *Manganese-Assisted Annealing Produces Abundant Macropores in a Carbon Aerogel to Enhance Its Oxygen Reduction Catalytic Activity in Zinc−Air Batteries.* ACS Sustain Chem Eng, 2021.

66. Yu, N., et al., *Flexible high-energy asymmetric supercapacitors based on MnO@C composite nanosheet electrodes.* Journal of Materials Chemistry A, 2017. **5**(2): p. 804-813.

67. Li, X.N., et al., *MnO@1-D carbon composites from the precursor C4H4MnO6 and their high-performance in lithium batteries.* Rsc Advances, 2013. **3**(25): p. 10001-10006.

68. Li, J.G., et al., *Birnessite-Type Manganese Oxide on Granular Activated Carbon for Formaldehyde Removal at Room*

Temperature. Journal of Physical Chemistry C, 2016. **120**(42): p. 24121-24129.

69. Zhao, Y., et al., *In situ anchoring uniform MnO2 nanosheets on three-dimensional macroporous graphene thin-films for supercapacitor electrodes.* Rsc Advances, 2015. **5**(110): p. 90307-90312.

70. Sun, S.Q., et al., *Electrochemical Deposition of -MnO2 on Ag/rGO Hybrid Films as Flexible Electrode Materials for Asymmetric Supercapacitor.* Electronic Materials Letters, 2019. **15**(3): p. 331-341.

71. Wang, Y., et al., *A facile hydrothermal synthesis of MnO2 nanorod-reduced graphene oxide nanocomposites possessing excellent microwave absorption properties.* Rsc Advances, 2015. **5**(108): p. 88979-88988.

72. Wu, S.P., et al., *Efficient imine synthesis via oxidative coupling of alcohols with amines in an air atmosphere using a mesoporous manganese-zirconium solid solution catalyst.* Catalysis Science & Technology, 2021. **11**(3): p. 810-822.

73. Salavati-Niasari, M.M., F.; Davar, F.; Saberyan K., *Fabrication of chain-like Mn2O3nanostructures via thermal decomposition ofmanganese phthalate coordination polymers.* Applied Surface Science, 2009. **256**: p. 1476-1480.

74. Zhang, X.D., et al., *Synthesis of highly efficient Mn2O3 catalysts for CO oxidation derived from Mn-MIL-100.* Applied Surface Science, 2017. **411**: p. 27-33.

75. Parveen, N., et al., *Feasibility of using hollow double walled Mn2O3 nanocubes for hybrid Na-air battery.* Chemical Engineering Journal, 2019. **360**: p. 415-422.

76. Feng, D.Y., et al., *Boosting High-Rate Zinc-Storage Performance by the Rational Design of Mn2O3 Nanoporous Architecture Cathode.* Nano-Micro Letters, 2020. **12**(1).

77. Kim, S.H., et al., *MnO2 Nanowire-CeO2 Nanoparticle Composite Catalysts for the Selective Catalytic Reduction of NOx with NH3.* Acs Applied Materials & Interfaces, 2018. **10**(38): p. 32112-32119.

78. Stratford, J.P., et al., *Electrically induced bacterial membrane-potential dynamics correspond to cellular proliferation capacity.* Proc Natl Acad Sci U S A, 2019. **116**(19): p. 9552-9557.

79. Felle, H., et al., *Quantitative measurements of membrane potential in Escherichia coli.* Biochemistry, 1980. **19**(15): p. 3585-90.

80. Ong, T.H., et al., *Cationic chitosan-propolis nanoparticles alter the zeta potential of S. epidermidis, inhibit biofilm formation by modulating gene expression and exhibit*

synergism with antibiotics. PLoS One, 2019. **14**(2): p. e0213079.

81. An, X.M.H.L., Bin; Wang, J., *Graphene Oxide Reinforced Polylactic Acid/Polyurethane Antibacterial Composites.* Journal of Nanomaterials, 2013: p. 1-6.

82. Rahman, S.R., M; Shajahan; Al-Mamun A., *Antibacterial Activity Study of Graphene OxidePolyaniline (GO-PANI) and GO-PANI-Mupirocin Composite against Escherichia coli and Staphylococcus aureus.* International Journal of Scientific & Engineering Research, 2019. **10**: p. 1475-1479.

83. Liu, S., et al., *Lateral dimension-dependent antibacterial activity of graphene oxide sheets.* Langmuir, 2012. **28**(33): p. 12364-72.

84. Liu, S., et al., *Antibacterial activity of graphite, graphite oxide, graphene oxide, and reduced graphene oxide: membrane and oxidative stress.* ACS Nano, 2011. **5**(9): p. 6971-80.

85. Abelson, P.H. and E. Aldous, *Ion antagonisms in microorganisms; interference of normal magnesium metabolism by nickel, cobalt, cadmium, zinc, and manganese.* J Bacteriol, 1950. **60**(4): p. 401-13.

86. Silver, S., et al., *Manganese-resistant mutants of Escherichia coli: physiological and genetic studies.* J Bacteriol, 1972. **110**(1): p. 186-95.

87. Brophy, M.B. and E.M. Nolan, *Manganese and microbial pathogenesis: sequestration by the Mammalian immune system and utilization by microorganisms.* ACS Chem Biol, 2015. **10**(3): p. 641-51.

88. Z., S., *Structural and Optical Study of Mn2O3 Nanoparticles in Antibacterial Activity.* Sylwan. **163**: p. 76-84.

89. Gnanam, S.A.R.S.K., *Antimicrobial Activity of the Novel Metal Oxide Nanoparticles Against Selected Human Pathogenic Bacteria.* Material Science and Engineering, 2019. **561**: p. 1-6.

90. Gribenko A.; Mosyak L.; Ghosh S.; Parris K.; Svenson K.; Moran J.; Chu L.; Li S.; Liu T.; Woods Jr, V., *Three-Dimensional Structure and Biophysical Characterization of Staphylococcus Aureus Cell Surface Antigen–ManganeseTransporter MntC.* Journal of Molecular Biology, 2013: p. 3430-3443.

91. Valderas, M.G.J.W., N.; and Hart M., *The Superoxide Dismutase Gene sodM Is Unique to Staphylococcus aureus: Absence of sodM in Coagulase-Negative Staphylococci.*

American Society for Microbiology, 2002. **184**: p. 2465-2472.

92. Juttukonda, L.J., et al., *Dietary Manganese Promotes Staphylococcal Infection of the Heart.* Cell Host Microbe, 2017. **22**(4): p. 531-542 e8.

93. Li, X.J., et al., *The Inhibition Effect of Tert-Butyl Alcohol on the TiO2 Nano Assays Photoelectrocatalytic Degradation of Different Organics and Its Mechanism.* Nano-Micro Letters, 2016. **8**(3): p. 221-231.

94. Tauber, A., et al., *Sonolysis of tert-butyl alcohol in aqueous solution.* Journal of the Chemical Society-Perkin Transactions 2, 1999(6): p. 1129-1135.

95. Liu, W., et al., *Synergistic adsorption-photocatalytic degradation effect and norfloxacin mechanism of ZnO/ZnS@BC under UV-light irradiation.* Scientific Reports, 2020. **10**(1).

96. Yang, X.F., et al., *Bifunctional TiO2/Ag3PO4/graphene composites with superior visible light photocatalytic performance and synergistic inactivation of bacteria.* Rsc Advances, 2014. **4**(36): p. 18627-18636.

97. Ahmad, N., et al., *Zinc oxide-decorated polypyrrole/chitosan bionanocomposites with enhanced photocatalytic,*

antibacterial and anticancer performance. Rsc Advances, 2019. **9**(70): p. 41135-41150.

98. Adhikari, S., et al., *Photocatalytic inactivation of E-Coli by ZnO-Ag nanoparticles under solar radiation.* Rsc Advances, 2015. **5**(63): p. 51067-51077.

99. Ganeshbabu, M., et al., *Synthesis and characterization of BiVO4 nanoparticles for environmental applications.* Rsc Advances, 2020. **10**(31): p. 18315-18322.

100. Grela, M.A., M.E.J. Coronel, and A.J. Colussi, *Quantitative spin-trapping studies of weakly illuminated titanium dioxide sols. Implications for the mechanism of photocatalysts.* Journal of Physical Chemistry, 1996. **100**(42): p. 16940-16946.

101. Dvoranova, D., et al., *EPR Investigations of G-C3N4/TiO2 Nanocomposites.* Catalysts, 2018. **8**(2).

102. Chauvin, J., et al., *Analysis of reactive oxygen and nitrogen species generated in three liquid media by low temperature helium plasma jet.* Scientific Reports, 2017. **7**.

103. Faria, A.F., F. Perreault, and M. Elimelech, *Elucidating the Role of Oxidative Debris in the Antimicrobial Properties of Graphene Oxide.* Acs Applied Nano Materials, 2018. **1**(3): p. 1164-1174.

104. Liu, S.B., et al., *Lateral Dimension-Dependent Antibacterial Activity of Graphene Oxide Sheets.* Langmuir, 2012. **28**(33): p. 12364-12372.

105. Mailloux, R.J., S.L. McBride, and M.E. Harper, *Unearthing the secrets of mitochondrial ROS and glutathione in bioenergetics.* Trends in Biochemical Sciences, 2013. **38**(12): p. 592-602.

106. Uhl, L. and S. Dukan, *Hydrogen Peroxide Induced Cell Death: The Major Defences Relative Roles and Consequences in E-coli.* Plos One, 2016. **11**(8).

107. Linley, E., et al., *Use of hydrogen peroxide as a biocide: new consideration of its mechanisms of biocidal action.* Journal of Antimicrobial Chemotherapy, 2012. **67**(7): p. 1589-1596.

108. Valderas, M.W., et al., *The superoxide dismutase gene sodM is unique to Staphylococcus aureus: Absence of sodM in coagulase-negative staphylococci.* Journal of Bacteriology, 2002. **184**(9): p. 2465-2472.

109. Smith, M.R., et al., *Redox dynamics of manganese as a mitochondrial life-death switch.* Biochemical and Biophysical Research Communications, 2017. **482**(3): p. 388-398.

110. Myers, C.R. and K.H. Nealson, *Bacterial Manganese Reduction and Growth with Manganese Oxide as the Sole Electron-Acceptor.* Science, 1988. **240**(4857): p. 1319-1321.

111. Ghiorse, W.C. and H.L. Ehrlich, *Electron transport components of the MnO2 reductase system and the location of the terminal reductase in a marine Bacillus.* Appl Environ Microbiol, 1976. **31**(6): p. 977-85.

112. Butterfield, C.N., et al., *Mn(II,III) oxidation and MnO2 mineralization by an expressed bacterial multicopper oxidase.* Proc Natl Acad Sci U S A, 2013. **110**(29): p. 11731-5.

113. Dick, G.J., et al., *Direct identification of a bacterial manganese(II) oxidase, the multicopper oxidase MnxG, from spores of several different marine Bacillus species.* Appl Environ Microbiol, 2008. **74**(5): p. 1527-34.

114. Collin, F., *Chemical Basis of Reactive Oxygen Species Reactivity and Involvement in Neurodegenerative Diseases.* Int J Mol Sci, 2019. **20**(10).

115. Yoshida, M., et al., *Photoexcited Hole Transfer to a MnOx Cocatalyst on a SrTiO3 Photoelectrode during Oxygen Evolution Studied by In Situ X-ray Absorption Spectroscopy.* Journal of Physical Chemistry C, 2014. **118**(42): p. 24302-24309.

116. Zhang, S., et al., *Sustained production of superoxide radicals by manganese oxides under ambient dark conditions.* Water Res, 2021. **196**: p. 117034.

117. Du, T., et al., *Antibacterial Activity of Manganese Dioxide Nanosheets by ROS-Mediated Pathways and Destroying Membrane Integrity.* Nanomaterials (Basel), 2020. **10**(8).

118. Alimohammadi, F., et al., *Antimicrobial Properties of 2D MnO2 and MoS2 Nanomaterials Vertically Aligned on Graphene Materials and Ti3C2 MXene.* Langmuir, 2018. **34**(24): p. 7192-7200.

119. Marafatto, F.F., et al., *Rate and mechanism of the photoreduction of birnessite (MnO2) nanosheets.* Proc Natl Acad Sci U S A, 2015. **112**(15): p. 4600-5.

120. Ahmed, S.A.Z.K.A.R.M.V.V.A.M.K.A., *Effective removal of methylene blue dye using nanoscale manganese oxide rods and spheres derived from different precursors of manganese.* Journal of Physics and Chemistry of Solids, 2021. **155**: p. 1-9.

121. Siddiqui, S.M., O; Mohsin, M.; Chaudhry S., *Nigella sativa seed based nanocomposite-MnO2/BC :Anantibacterial materialfor photocatalytic degradation, and adsorptive removal of Methylene blue from water* Environmental Research, 2018. **171**: p. 328-340.

122. Zhou, S.X., et al., *Degradation of methylene blue by natural manganese oxides: kinetics and transformation products.* Royal Society Open Science, 2019. **6**(7).

123. Aussel, L., et al., *Biosynthesis and physiology of coenzyme Q in bacteria.* Biochimica Et Biophysica Acta-Bioenergetics, 2014. **1837**(7): p. 1004-1011.

124. Reddy, I.N., et al., *A study of coral reef-like tetragonal Mn3O4 nanostructure photoelectrode for photoelectrochemical water splitting under visible irradiation.* Journal of Electroanalytical Chemistry, 2020. **874**.

125. Dubal, D.P., et al., *A novel chemical synthesis and characterization of Mn3O4 thin films for supercapacitor application.* Applied Surface Science, 2010. **256**(14): p. 4411-4416.

126. Bui, P.T.M., et al., *Low temperature solution processed Mn3O4 nanoparticles: Enhanced performance of electrochemical supercapacitors.* Journal of Alloys and Compounds, 2017. **694**: p. 560-567.

127. Cockayne, E. and L. Li, *First-principles DFT+U studies of the atomic, electronic, and magnetic structure of alpha-MnO2 (cryptomelane).* Chemical Physics Letters, 2012. **544**: p. 53-58.

128. Zhao, Q.H., et al., *Preintercalation Strategy in Manganese Oxides for Electrochemical Energy Storage: Review and Prospects.* Advanced Materials, 2020. **32**(50).

Chapter 5: Summary of Research Results

The low-temperature growth of MnO_2 from the oxidation of sp^2 domains from GOQD with $KMnO_4$ lead to a chemically stable and water soluble GOQD/MnO_2 nanocomposite structure. Photoluminescence and time resolved fluorescence lifetime (TRFL) suggest an enhanced photodynamic activity from the electronic configuration of the GOQD with MnO_2. The sp^2 C binding energy at 284.0 eV experienced the highest chemical shift for all the GOQD/MnO_2 samples which indicates electron transfer from the GOQD to MnO_2 under steady state conditions. The measured fluorescence lifetime constant further demonstrates the possible electron transfer process from GOQD to MnO_2 under 365 nm excitation for the GOQD/MnO_2-c sample which maintained a rate constant of $\tau_{365\ nm}$= 2.564 ns. The increased fluorescence lifetime for GOQD/MnO_2-c correlated with the enhanced photodynamic activity measured for GOQD/MnO_2-c with the lowest documented time of cell death (TCD) amongst all

GOQD/MnO_2 samples. The radical scavenger experiments conducted with EDTA and TBA suggested a radical species as the source of bactericidal activity. Analysis via electron paramagnetic resonance (EPR) determined hydrogen radical formation as the leading species responsible for bactericidal activity.

A series of metal chelated GOQD nanostructures were developed to further understand the photoactivity of metal oxides for graphene oxide-based nanocomposite structures. An aqueous sonication technique was utilized to dope the metal ions on the exposed oxygen moieties of GOQD. TEM analysis of GOQD-Co^{2+} which contained the highest photoactivity at 365 nm exc. demonstrated a lack of metal oxide deposition. A highly quenched GOQD-Co^{2+} photoluminescence spectra measured from an excitation at 365 nm with an increased fluorescence lifetime constant of $\tau_{365\ nm}$ = 2.09 ns was a measure of effective electron-hole separation from metal doping of GOQD. The oxidation of Co^{2+} to Co^{3+} was measured via XPS with a decrease in chemical shift from the O1s spectra of GOQD. The shift in binding energy of O1s and the lack of oxygen lattice at 530.0 eV which is readily measured for metal oxide structures

further supported the electronic interaction between GOQD and Co^{2+}. The enhanced photoactivity at an excitation wavelength of 365 nm excitation for GOQD-Co^{2+} correlated with the fluorescence emission and fluorescence lifetime constant. Although the source of bactericidal activity upon irradiation was not attributed to the production of reactive oxygen species (ROS).

Previous experiments determined a high valency of Mn^{4+} with electronic interaction to GOQD was required to induce photodynamic activity at 365 nm excitation. To assess the role of oxidation state and the role of electronic distribution between GOQD and Mn_xO_y, a GOQD based composite with Mn_xO_y anchored via polyaniline (PANI) was synthesized. The TEM of GOQD/PANI/Mn_xO_y (GPM) measured layered GOQD with stacked Mn_xO_y nanoparticles. XRD measured Mn^{2+} amongst all GPM samples which was attributed to the oxidation of PANI in the presence of Mn^{4+}. The measured XPS supported the presence of Mn^{2+} amongst all GPM samples but discerned GPM-1 and GPM-2 from GPM-3 by the presence of Mn^{4+} from the former and Mn^{3+} from the latter. Fluorescence measurements of GPM measured quenching for GPM-1 and GPM-2 in comparison to

GPM-3 which correlated with electronic interaction of GOQD and PANI with the deposited Mn_xO_y of GPM-1 and GPM-2. The photoactivity of GPM samples was tested for gram-negative *E. coli* and gram- positive *S. Epidermidis* with enhanced photodynamic activity measured for GPM-1 for *E. coli* and GPM-2 for *S. Epidermidis*. The radical scavenger experiments conducted with TBA and EDTA attributed the source of bactericidal activity related to the photoproduction of holes from deposited metal oxide nanoparticles. The specific radical species produced amongst all GPM samples was $HO^{\cdot -}$ which was quenched extensively in the presence of EDTA. Surprisingly, the highest production of ROS was measured for GPM-3. Therefore, an intimate interaction of GPM-1 and GPM-2 with the cell membrane of *E. coli* and *S. Epidermidis* is proposed as the leading cause for the efficacy of the photocatalysts.

The work presented emphasizes the application of GOQD and Mn_xO_y based composits nanostructures for photodynamic activity with UV irradiation. Electronic distribution between the GOQD and Mn_xO_y and oxidation state of Mn was found to provide an active role in enhanced photo-induced bactericidal activity. Ultimately the Mn_xO_y is

the active site leading to ROS production. Although ROS is a leading cause for photoinduced bactericidal activity a close interaction between the composite nanoparticle and cell membrane can lead to enhancement of the photoactive nanoparticle.

Chapter 6: Future Work

Functionalization of GOQD with positively charged amines could enhance intimate cellular interaction via ester formation. The extent of functionalization would lead to varying surface charges from the GOQD structures which could b examined with a series of bacteria. Metal doping of Mn_xO_y would be desirable since it could decrease the band-gap energy as well as produce trapped states increasing the production of ROS. The photoactivity of GOQD-Co^{2+} structure could be enhanced by producing a core shell structure which could provide a close cellular interaction but prevent hydrolysis and nanoparticle aggregation. The biocompatibility of GOQD based nanocomposites should be

examined with mammalian cell lines like human's epithelial cells to assess their cytotoxicity to treat bacterial infection.